UNIVERSITY OF CALIFORNIA, SAN DIEGO

The role of computer simulations in the preclinical development of semiflexible polymeric anticancer therapeutics

A dissertation submitted in partial satisfaction of the requirements for the degree of

Doctor of Philosophy

in

Bioengineering

by

Lili Xiaoping Peng

Committee in charge:

David A. Gough, Chair
Karen L. Christman
Michael J. Heller
Stephen B. Howell
J. Andrew McCammon
Lei Yu

2010

The dissertation of Lili Xiaoping Peng is approved, and is acceptable in quality and form for publication on microfilm and electronically:

_____

_____

_____

_____

_____

_____
Chair

University of California, San Diego

2010

DEDICATION

Dedicated with love to my late grandparents, Liu Ming and Tang Yizhi, for their eternal support.

EPIGRAPH

"Whoso would be a man must be a nonconformist."

Ralph Waldo Emerson, Self-Reliance

TABLE OF CONTENTS

LIST OF ABBREVIATIONS

AA, all-atom

ADME, adsorption, distribution, metabolism, excretion

CD, circular dichroism

CG, coarse-grained

DPBS, Dulbecco's Phosphate Buffered Saline

f_{PTX}, PTX loading fraction

GAFF, Generalized AMBER force field

GG_{NH3+}, γ-glutamyl-glutamate (amino terminus)

GG, γ-glutamyl-glutamate

GG_{COO-}, γ-glutamyl-glutamate (carboxyl terminus)

GROMACS, GROningen Machine for Chemical Simulations

IND, Investigational New Drug

MARTINI, MARrink's Toolkit INItiative

MD, molecular dynamics

MW, molecular weight

npRGD, nonpeptide RGD (Arginine-Glycine-Aspartate)

PDB, Protein Data Bank

PEG, poly(ethylene) glycol

PGG, poly(γ-glutamyl-glutamate)

PGG-PTX, poly(γ-glutamyl-glutamate) paclitaxel

PGG-PTX-PEG-npRGD, nonpeptide RGD-targeted poly(γ-glutamyl-glutamate) paclitaxel poly(ethlylene) glycol

PTX, Paclitaxel

RESP, restrained electrostatic potential

R_{gyr}, radius of gyration

RMSD, root mean square deviation

RMSF, root mean square fluctuation

VMD, Visual Molecular Dynamics

LIST OF FIGURES

LIST OF TABLES

LIST OF SCHEMES

ACKNOWLEDGEMENTS

I would like to thank Professor David Gough for his patience and encouragement through thick and thin, allowing me to make and learn from my own mistakes. No words can describe my appreciation for his support. I would like to thank J. Andrew McCammon for his tremendous generosity in providing me the resources and guidance on this thesis project that would otherwise would have not been accomplished. Professors Karen Christman and Michael Heller are thanked for their guidance and willingness to serve on my doctoral committee. I gained much from scientific discussions with scientists from Nitto Denko Technical Corporation, in particular Lei Yu, Sang Van, and Sanjib Das. Last, but not least, I would like to acknowledge the very important role played by Dr. Stephen Howell in my research.

I would like to thank all the people in the UCSD Biosensors Laboratory for their continued encourage and support.

I would like to extend my gratitude to all the people in the UCSD McCammon Group for the help given during the various stages of my thesis. A special thanks to Gary Huber for formally introducing me to the group, and Anthony Ivetac and Mikolai Fajer for editing our manuscripts. I would also like to thank Robert Swift, Barrett Abel, and many others for their assistance.

I would like to thank my parents for instilling in me a determination to succeed and love of knowledge that were necessary foundations in my pursuit of this degree.

I would like to thank Keith Chan for his emotional and intellectual support, always standing by me and loving me. He has been and will always be very close to my heart.

Funding for the research described in this thesis was provided in part by Nitto Denko Technical Corporation and by the University of California Discovery Program's Research Award bio06-10568.

Chapter 2, in full, is a reprint of the material as it appears in *Biopolymers*, 2010, Peng LX**,** Ivetac A, Van S, Zhao G, Chaudhari AS, Yu L, Howell SB, McCammon JA, Gough DA. The dissertation author was the primary investigator and first author of this paper.

Chapter 3, in full, has been submitted for publication of the material as it may appear in *Biomacromolecules*, Peng LX, Fajer M, Das SK, Yu L, Howell SB, Gough DA. The dissertation author was the primary investigator and first author of this paper.

Chapter 4, in part, is currently being prepared for submission for publication of the material. Peng LX, Ivetac A, Das SK, Yu L, Howell SB, Gough DA. The dissertation author was the primary investigator and first author of this paper.

Chapter 5, in part, is currently being prepared for submission for publication of the material. Peng LX, Chaudhari AS, Das SK, Yu L, Howell SB, Gough DA. The dissertation author was the primary investigator and first author of this paper.

VITA

Studies:

- B.S., Chemical Engineering, Massachusetts Institute of Technology (2005)
- M.S., Bioengineering, University of California, San Diego (2008)
- Ph.D., Bioengineering, University of California, San Diego (2010)

Teaching and Research:

- Teaching Assistant, Bioengineering, 2005-2007
- Graduate Student Researcher, 2006-2010

Publications:

Peng LX, Ivetac A, Van S, Zhao G, Chaudhari AS, Yu L, Howell SB, McCammon JA, Gough DA. "Characterization of a clinical polymer-drug conjugate using multiscale modeling." *Biopolymers* Apr 26 2010.

Peng LX, Fajer M, Das SK, Yu L, Howell SB, Gough DA. "The molecular conformation of a polymeric anticancer therapeutic: a coarse-grained modeling study." *Biomacromolecules* (under review).

Peng LX, Ivetac A, Das SK, Yu L, Howell SB, Gough DA. "Computer simulations for accelerated selection of candidate compounds of a preclinical polymer-drug conjugate." (in preparation).

Peng LX, Chaudhari AS, Das SK, Yu L, Howell SB, Gough DA. "Effect of PEG molecular weight and nonpeptide RGD density on the conformation of poly(glutamyl-glutamate) paclitaxel: a coarse-grained modeling study." (in preparation).

ABSTRACT OF THE DISSERTATION

The role of computer simulations in the preclinical development of semiflexible anticancer polymeric therapeutics

by

Lili Xiaoping Peng

Doctor of Philosophy in Bioengineering

University of California, San Diego, 2010

Professor David A. Gough, Chair

Poly(γ-glutamyl-glutamate) paclitaxel (PGG-PTX) is a potential anticancer therapeutic in preclinical development. There has been increasing attention on how structural and functional properties of therapeutic nanoparticles, such as size, shape, flexibility, surface hydrophilicity, and aggregation, influence efficacy. This thesis demonstrates the application of computer simulations to elucidate these properties of PGG-PTX candidates, which would otherwise be tedious or inaccessible to achieve experimentally.

Computer simulations were carried out by running molecular dynamics (MD) simulations on eighteen coarse-grained (CG) PGG-PTX models, varying in the PTX loading fraction (f_{PTX} = 0.18, 0.24, and 0.37) and spatial PTX arrangement (uniform:

'even' and 'random', clustered: 'clusters' and 'ends', concentrated: 'middle' and 'side') on the PGG backbone. The results show that PGG-PTX molecules with concentrated spatial PTX arrangements produce filamentous shapes and are more flexible, while PGG-PTX molecules with uniform PTX arrangements generate globular morphologies and are less flexible. The PTX loading fraction and spatial PTX arrangement have a minimal effect on the size of a PGG-PTX molecule. Intermolecular aggregation increases with increasing PTX loading fraction, while surface hydrophilicity decreases with increasing PTX loading fraction. The PGG-PTX molecules at $f_{PTX} = 0.24$ with concentrated spatial PTX distributions exhibit nonspherical shape, high flexibility, low aggregation, and high surface hydrophilicity. Since these properties have been shown to be clinically advantageous, we recommend the PGG-PTX molecules at $f_{PTX} = 0.24$ with concentrated spatial PTX distributions for experimental testing.

The shape, flexibility, and surface hydrophilicity of nonpeptide RGD-targeted PGG-PTX systems varying in poly(ethylene glycol) (PEG) spacer length (500 Da, 1000 Da, and 2000 Da) and npRGD ligand density (4, 8, 12, and 16 per PGG-PTX-PEG-npRGD molecule) were also examined. Results from CG MD simulations show that the PGG-PTX-PEG1000-npRGD$_8$ and PGG-PTX-PEG1000-npRGD$_{12}$ molecules were the most promising candidates, given their filamentous shape, high flexibility, and high surface hydrophilicity.

Overall, we introduce computer simulations as a tool for facilitating the preclinical development of polymeric drug delivery systems.

Chapter 1

Introduction

1.1 Motivation and approach

Cancer is currently the leading cause of morbidity and mortality in the United States. While a wide range of therapies and treatments are available to patients, chemotherapy has consistently been shown to be the most effective. A well-known chemotherapeutic agent used to treat patients with breast, ovarian, and lung cancers is paclitaxel (Taxol®). Paclitaxel stabilized microtubule polymerization during cell division, thus inhibiting mitosis of tumor cells. While paclitaxel has been proven to be effective in prevent tumor growth, it is highly hydrophobic and thus not sufficiently water-soluble. Efforts to improve paclitaxel's solubility have included its chemical conjugation to a hydrophilic delivery agent, such as albumin-bound paclitaxel (ABRAXANE®) and poly(glutamate) paclitaxel (CT-2103 or OPAXIO^{TM}). This study focuses on poly(γ-glutamyl-glutamate) paclitaxel (PGG-PTX) and nonpeptide RGD-targeted poly(γ-glutamyl-glutamate) paclitaxel poly(ethylene glycol) (PGG-PTX-PEG-npRGD), which were anticancer therapeutics in preclinical development at Nitto Denko Technical Corporation during the duration of this thesis work. The formulations included PGG-PTX varying in PTX loading fraction by mass (f_{PTX} of 0.18, 0.24, and 0.37), and nonpeptide RGD-targeted PGG-PTX (f_{PTX} = 0.37) conjugated with poly(ethylene glycol)

(PEG) varying in PEG molecular weight (500 Da, 1000 Da, and 2000 Da) and nonpeptide RGD ligand density (4, 8, 12, and 16 ligands per PGG-PTX-PEG-npRGD molecule).

1.2 Biological transport barriers in drug delivery

In chemotherapy, a therapeutic agent is first intravenously administered into the bloodstream of a cancer patient. From then on, the drug delivery system encounters multiple "resistances" that impeded its journey to the target tumor. Such resistances include:

- Clearance by the reticoendothelial system (RES) via macrophage opsonization
- Adhesion of walls to tumor endothelia
- Extravasation through fenestrations of tumor vasculature
- Binding to surfaces of tumor cells
- *In vivo* stability

For a drug to reach its maximum therapeutic potential, it must reach the tumor in sufficient amounts while simultaneously minimize toxicity and other adverse effects to normal, healthy tissue. Therefore, the drug must overcome the aforementioned barriers in their journey to the target tumor. In the past 5-10 years, the structural and functional properties of nanoparticles have been receiving increasing attention for influencing the drug's ability to overcome these resistances. For instance, particles with higher surface hydrophilicity and higher molecular weight have been shown to avoid macrophage opsonization and ultimately RES clearance, thus resulting in a longer circulation half-life. Moreover, nonspherical, wormlike, and filamentous particles have demonstrated firmer

adhesion to walls of tumor endothelia. There has also been speculation that particles with higher flexibility can bind more effectively to surfaces of tumor cells. Finally, higher degrees of particle aggregation have been associated with lower *in vivo* stability.

1.3 Facilitating preclinical development using computer simulations

In preclinical development, candidate therapeutic agents are rigorously assessed for their safety, efficacy, and biodistribution using *in vitro* and *in vivo* testing in pharmacodynamics, pharmacokinetics, adsorption, distribution, metabolism, excretion (ADME), and toxicity profiles to order to estimate a safe starting dose of the drug in clinical trials in humans. While preclinical testing is crucial for filing an Investigational New Drug (IND) application to initiate a Phase I clinical trial, the highly experimental nature of the preclinical phase results an exhaustive and resource-intensive process that can take up to a decade to accomplish. Given the urgent clinical needs of cancer patients, there is a need for new methods to accelerate the preclinical development of therapeutic agents.

To our knowledge, computer simulations have yet to be used in assisting the preclinical development of a therapeutic agent. Computational modeling can provide insight into the behavior of biomolecules that is inaccessible experimentally. Therefore, the modeling results can be used to help design meaningful experiments in preclinical development. This thesis work focuses on using molecular modeling of PGG-PTX and PGG-PTX-PEG-npRGD candidates to identify the most promising compounds based on their size, shape, flexibility, surface hydrophilicity, and aggregation.

1.4 Challenges in the molecular modeling of PGG-PTX and PGG-PTX-PEG-npRGD

Prior to running MD simulations of PGG-PTX and PGG-PTX-PEG-npRGD systems, there were challenges and difficulties in our approach that needed to be addressed. The first challenge concerned the starting structure of PGG-PTX and PGG-PTX-PEG-npRGD. The initial structures for the MD simulations are usually obtained from the Protein Data Bank (PDB), a repository of three-dimensional structural data of biomolecules, such as proteins and nucleic acids, obtained from X-ray crystallography and NMR spectroscopy. However, since the PDB structures for PGG-PTX and PGG-PTX-PEG-npRGD compounds are not available, circular dichroism (CD) spectroscopy was used to gain insight on the secondary structural information of PGG-PTX and PGG-PTX-PEG-npRGD. Since the CD spectroscopy results show that PGG-PTX and PGG-PTX-PEG-npRGD exist as random coils, further NMR spectroscopy was not necessary. This evidence suggests that the PGG-PTX and PGG-PTX-PEG-npRGD molecules can be simulated starting from any initial (random) position.

The second challenge was related to the size of each PGG-PTX and PGG-PTX-PEG-npRGD molecule. The molecular weight of each PGG-PTX molecule at f_{PTX} = 0.18, 0.24, and 0.37 were roughly 70 kDa, 80 kDa, and 90 kDa, respectively, and the molecular weight of the PGG-PTX-PEG-npRGD molecules range from ~58 kDa to 170 kDa. Given the relatively large size of each system, it would be impractical to run all-atom (AA) MD simulations in explicit solvent to the desired time scale, as such a feat would required an extraordinary amount of computational expenses. Therefore, efforts

were made to access longer timescales in the μs range by reducing the amount of information in each system. AA models were constructed in AMBER 9.0 and then converted to coarse-grained (CG) models using the MARTINI mapping scheme. Parameterization of the CG models was accomplished by running AA MD simulations and then extracting the bonded distances and angles from the results using the Boltzmann inversion. CG MD simulations of the PGG-PTX and PGG-PTX-PEG-npRGD systems were run in GROMACS 4.0.3.

Another difficulty was the deciding when to stop the CG MD simulations. Given the combination of flexible PGG and rigid PTX, PGG-PTX is by nature semiflexible. Likewise, the flexible PEG polymer and rigid nonpeptide RGD also results in a semiflexible PGG-PTX-PEG-npRGD molecule. Traditional methods of determining the structural conformations of biomolecules involve running MD simulations to a point where the potential energy of a system has converged to equilibrium. At this point, the molecule is rigid. Because PGG-PTX and PGG-PTX-PEG-npRGD are semiflexible and exist as a random coil, it is not expected that the systems will ever reach a static equilibrium. Alternatively, we ran MD simulations on PGG-PTX models until statistical equilibrium was attained, a point at which there is minor fluctuations on the molecular level, yet the overall system exhibit minimal movement. To our knowledge, this study is the first time such an analysis has been applied to examine the structural conformations of semiflexible compounds.

1.5 Overview of thesis

This document provides a comprehensive theoretical study of the possible structural and functional properties of PGG-PTX and PGG-PTX-PEG-npRGD. Results are broken down by chapter: Chapter 2 explores the influence hydrophobic mass fraction (f_{PTX}) and spatial PTX dispersion patterns on the size and shape of a single PGG-PTX molecule resulting from the final trajectory snapshot at 800 ns of CG MD simulations; Chapter 3 introduces root-mean-squared deviation (RMSD) clustering as an improved method to analyze the size, shape, and flexibility of a PGG-PTX resulting from 2 μs of CG MD simulations; Chapter 4 examines the impact of f_{PTX} and spatial PTX dispersion on the morphology, flexibility, aggregation, and surface hydrophilicity of systems of multiple PGG-PTX molecules resulting from 4 μs of CG MD simulations; and Chapter 5 begins discussion on how the npRGD ligand density and PEG spacer length concomitantly affect the size, shape, and flexibility of each PGG-PTX-PEG-npRGD molecule.

Chapter 2

Characterization of a clinical polymer-drug conjugate using multiscale modeling

Abstract

The molecular conformation of certain therapeutic agents has been shown to affect the ability to gain access to target cells, suggesting potential value in defining conformation of candidate molecules. This study explores how the shape and size of poly(γ-glutamyl-glutamate) paclitaxel (PGG-PTX), an amphiphilic polymer-drug with potential chemotherapeutic applications, can be systematically controlled by varying hydrophobic and hydrophilic entities. Eighteen different formulations of PGG-PTX varying in three PTX loading fractions of 0.18, 0.24, and 0.37 and six spatial arrangements of PTX ('clusters', 'ends,' even', 'middle', 'random', and 'side) were explored. Molecular dynamics (MD) simulations of all-atom (AA) models of PGG-PTX were run until a statistical equilibrium was reached at 100 ns and then continued as coarse-grained (CG) models until a statistical equilibrium was reached at an effective time of 800 ns. Circular dichroism spectroscopy was used to suggest initial modeling configurations**.** Results show that a PGG-PTX molecule has a strong tendency to form coil shapes, regardless of the PTX loading fraction and spatial PTX arrangement, although globular shapes exist at $f_{PTX} = 0.24$. Also, less uniform PTX arrangements such

as ‘ends’, ‘middle’, and ‘side’ produce coil geometries with more curvature. The prominence of coil shapes over globules demonstrates that PGG-PTX may confer a long circulation half-life and high propensity for accumulation to tumor endothelia. This multiscale modeling approach may be advantageous for the design of cancer therapeutic delivery systems.

2.1. Introduction

There is a continuing interest in the development of new chemotherapeutic agents for cancer therapy.[1] Although many existing cancer therapeutics are known to be highly effective in destroying cancer cells *in vitro*, physiological barriers may prevent optimal access of the therapeutic to its target. Various investigators have argued that the ability of a therapeutic to successfully cross these barriers may depend on its physicochemical properties such as shape and size.[1, 2] For instance, wormlike, filamentous polymeric micelles remain in the blood ten times longer than their spherical counterparts.[3, 4] Ellipsoidal particles have shown to have a higher propensity to accumulate to the walls of tumor endothelia, than spherical particles.[5] Also, size affects ability of nanoparticle therapeutics to extravasate through fenestrated endothelia[6, 7] as well as influence particle uptake rate by tumor cells,[2, 8] particularly during phagocytosis.[9, 10] These intriguing observations suggest the shape and size of a therapeutic as a basis for design.

Since most therapeutic drugs are rigid, polar molecules, a flexible and hydrophilic entity is often attached to the drug to alter its physicochemical properties. As drug delivery agents, polymers are known to confer benefits such as targeting drugs to the tumor while simultaneously minimizing toxicity by limiting drug exposure to normal

tissue, increasing blood circulation half-life of drugs, and increasing adsorption of drugs to tumor tissue.[6, 11] The polymer-drug hybrid comprised of a rigid, hydrophobic therapeutic component and a flexible, biodegradable, and hydrophilic component may enhance the overall effectiveness of the drug.

This study focuses on developing a polymer-drug construct with potential applications for cancer chemotherapy: poly(γ-glutamyl-glutamate) paclitaxel (PGG-PTX). A flexible, biocompatible, water-soluble polymer, poly-γ-glutamyl-glutamate (PGG) is covalently attached to paclitaxel (Taxol®, $C_{47}H_{51}NO_{14}$), a widely used anticancer therapeutic known for its high efficacy in treating breast, ovarian, and lung cancers.[12-14] Due to paclitaxel's high hydrophobicity and poor solubility, PGG, a hydrophilic, biodegradable carrier, is used to effectively deliver paclitaxel to tumors while minimizing adverse toxicity effects.[15] For comparison, a recent formulation of paclitaxel currently available on the market is paclitaxel bovine serum albumin, known as Abraxane®.[16] The traditional method of designing cancer therapeutics usually invokes an empirical approach of trial-and-error testing of chemical substances on animals and subsequently matching of apparent effects to treatments. While effective, this procedure can be time-consuming and expensive.[17] We used multiscale modeling to elucidate the shape and size of various forms of a PGG-PTX molecule. Such information would aid in the ultimate effort to identify potentially useful conformational variants, which would be otherwise expensive and time-consuming to achieve by systematic synthesis. Our goal was to create a library of molecular conformations that can be biologically tested for potential advantages in chemotherapy.

In the field of molecular modeling, docking methods have been used to predict the activity and affinity of rigid small molecule drug candidates to their protein targets.[18-20] Although molecular modeling methods have been applied to flexible systems such as polymers in effort to predict their behavior,[4, 21-23] modeling both rigid and flexible components poses new challenges and has yet to be attempted. Given the composite of the rigid paclitaxel molecule and the flexible PGG polymer, full equilibrium of the system will never be attained from running molecular dynamic (MD) simulations. Therefore, a PGG-PTX molecule is not expected to have a unique, singular equilibrated structure, but rather tend to a dynamic ensemble of molecular conformations, defined by a statistical equilibrium, a state representing ongoing structural movement with statistical similarity. At this point, there is little further change in the overall structure, although there may be minor movement on the molecular level. Our goal was to gain a *general* understanding of the range of candidate morphologies that can be generated from PGG-PTX, as well as demonstrate a novel and unique application of multiscale modeling for characterizing cancer therapeutics.

Given the practicalities of running MD simulations, there is a need for specifying the initial molecular structure. To construct the initial all-atom (AA) model of PGG-PTX, circular dichroism (CD) spectroscopy was used to gain information about the secondary structure of PGG-PTX in solution.[24] However, a concern arises: since MD simulations can not be infinitely long, an acceptable approximation of the molecular structure is needed.[25]

Computational modeling tools can be advantageous for understanding the dynamical and structural phenomena of molecular systems. Currently there exist a wide

variety of methods suitable for molecular systems ranging from proteins, polymers, and nucleic acids.[26] However, AA MD simulations of relatively large systems (thousands to ten-thousands of atoms) can require a lot of CPU power and be very expensive. Therefore, to minimize computational costs, coarse-grained (CG) models are implemented by reducing the amount of structural information yet maintaining the integrity of the structural information conferred by AA models. Examples of such CG MD approaches have been applied to a wide range of molecular events, such as investigating protein folding and elucidating protein-protein interactions. Such CG simulation methods for polymer systems include Monte Carlo methods, dissipative particle dynamics, and Brownian dynamics.[27, 28] In this study, multiscale MD simulations of PGG-PTX were carried out by first developing AA models and then CG models in order to access the hundreds of nanoseconds regime while minimizing CPU usage.

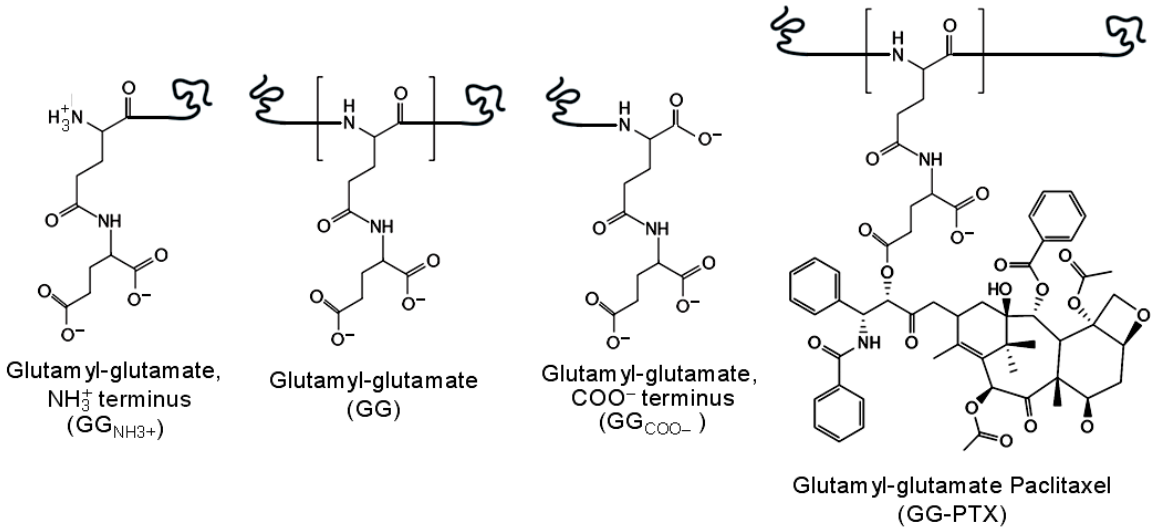

Figure 2.1. Chemical structures of GG and GG-PTX. The GG residue differs slightly based on its position on the polymer, such as its position at the amino or carboxyl termini. For the GG-PTX residue, paclitaxel is covalently conjugated to a carboxylate group of glutamyl-glutamate via an ester linkage. GG_{NH3+} and GG-PTX each has a charge of -1, GG a charge of -2, and GG_{COO-} a charge of -3. (Note: each twisted line represents the position to which a preceding or subsequent residue is covalently attached.)

A PGG-PTX molecule is comprised of a 130-mer PGG backbone with PTX molecules covalently attached to a glutamate-glutamyl molecule via an ester linkage (see Fig. 2.1). There currently exist three different formulations of PGG-PTX varying in the number of PTX molecules attached to the PGG polymer, or PTX loading fraction (f_{PTX}):

$$f_{PTX} = \frac{MW_{PTX}}{MW_{PGG-PTX}} \quad (1)$$

where MW_{PTX} is the molecular weight of all paclitaxel molecules on a PGG-PTX molecule, and $MW_{PGG\text{-}PTX}$ is the molecular weight of then entire PGG-PTX molecule.

The three PGG-PTX formulations are f_{PTX} = 0.18, 0.24, or 0.37, which correspond to 12, 19, and 26 paclitaxel molecules on the 130-mer PGG polymer, respectively. To explore the possible morphologies that each PGG-PTX formulation offers, it is of interest to test how the spatial positioning of hydrophobic PTX groups on the hydrophilic PGG backbone impacts the shape and size of a molecule. Therefore, for each f_{PTX}, the respective paclitaxel molecules were systematically positioned in a controlled manner on a 130-mer PGG polymer in six manners: ‘clusters’, ‘ends’, ‘even’, ‘middle’, ‘random’, and ‘side’ arrangements. Fig. 2.2 shows the six ways PTX can be spatially arranged on the PGG polymer for the f_{PTX} = 0.18 formulation. Applying this patterning scheme to the f_{PTX} = 0.24 and 0.37 formulations results in an array of 18 different PGG-PTX molecules for structural evaluation.

Multiscale modeling was then carried out as follows: AA MD simulations were run on the eighteen PGG-PTX molecules in the AMBER version 9.0 suite of programs[29] using the Cornell et al. parm99[30] and Generalized AMBER force fields[31] (GAFF) until each system reach a statistical equilibrium, which was usually attained by 100 ns, as

indicated by root-mean-square deviation (RMSD) time evolutions. CG parameterization of the AA PGG-PTX models was done using the MARrink's Toolkit INItiative (MARTINI) force field.[32] Subsequent CG MD simulations were run using GROningen Machine for Chemical Simulations (GROMACS) version 4.0.3 software package[33] for effective times of 800 ns.

2.2. Experimental Methods

2.2.1 Sample preparation

Lyophilized samples of PGG-PTX varying in f_{PTX} = 0.18, 0.24, and 0.37 were provided by Nitto Denko Technical Corporation (Oceanside, CA). Each sample was weighed and then diluted to 1mg/ml in 1X HyClone modified DPBS buffer (ThermoScientific, Cat. No. SH30028.03). The samples were then sonicated in a 37ºC water bath for 15 min and vortexed at room temperature for 1 min. The samples were then allowed to settle at room temperature for an additional 10 min. Finally, the samples were then filtered using a 0.2 μm filter paper (Corning, Part No. 431215) and a 20G 1½ Precision Glide needle (Becton Dickinson).

2.2.2 Circular dichroism spectroscopy

CD spectroscopy measurements for PGG-PTX were carried out using an AVIV Model 202 spectrophotometer. CD spectra of pure 1X DPBS buffer and FD protein in 50% TFE/50% double distilled H_2O/0.1% TFA were also taken as the negative and positive controls, respectively. All measurements were done at 37ºC. The far-UV CD spectra were recorded from 190 to 260 nm using a 1 cm rectangular quartz cuvette, and

the CD spectra were collected at every 0.5 nm with 5 sec at each point. For each sample except pure 1X DPBS, the concentration was adjusted and diluted so that the dynode

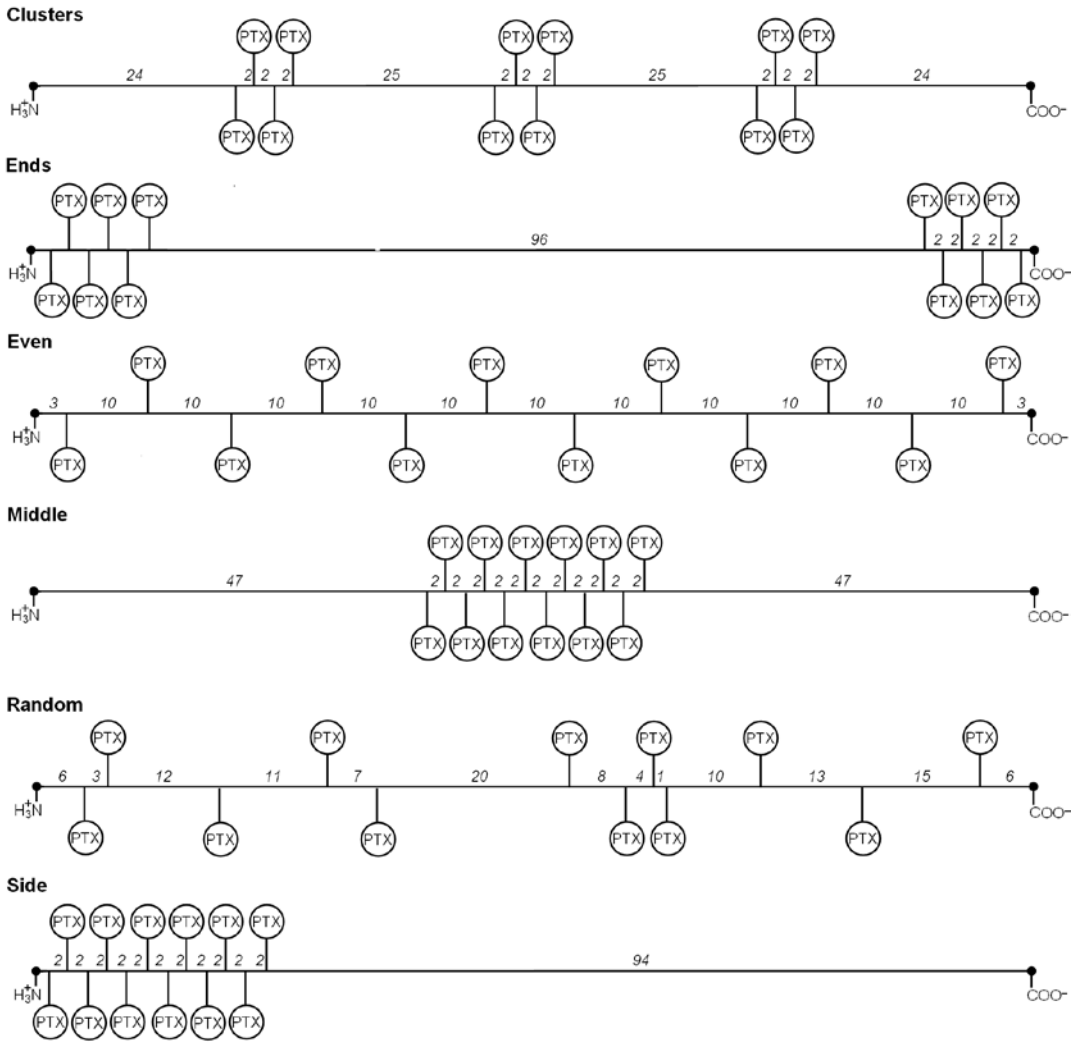

Figure 2.2. Abstract representation of the spatial PTX positioning patterns on the PGG backbone for f_{PTX} = 0.18. Each PGG-PTX molecule is composed of 130 glutamyl-glutamate monomers and 12 paclitaxel molecules. Shows how 12 PTX are covalently attached to the PGG backbone in six arrangements: 'clusters' (3 PTX groups with 4 PTX per group, spaced an equal number of residues apart), 'ends' (2 PTX groups with 6 PTX each, located at both ends), 'even' (each PTX is spaced an equal number of residues apart along PGG), 'middle' (all PTX molecules positioned in the middle), 'random' (all PTX molecules located in random positions), and 'side' (all PTX molecules located at the amino terminus end). Numbers between residues denote number of repeating GG residues that are not amino- or carboxyl-termini GG residues. The amino- and carboxyl-termini GG residues are represented by black dots at the ends of each line. The abstract representations for the f_{PTX} = 0.24 and 0.37 molecules are shown in Figs. 2.14 and 2.15, respectively.

voltage corresponding to the ellipticity signal remained below 500 V throughout the entire spectra collection period. (It has been suggested by Greenfield et al. that the signal-to-noise ratio will greatly diminish once the dynode voltage exceeds 500 V.[24]) The optimum concentrations of each sample leading to optimum ellipticity signal and lowest signal-to-noise ratio were determined to be: 1 mg/ml of PGG-PTX at f_{PTX} = 0.18 in 1X DPBS, 1 mg/ml of f_{PTX} = 0.24 in 1X DPBS, 1 mg/ml of f_{PTX} = 0.37 in 1X DPBS, and 0.25 mg/ml of FD protein in 50% TFE/50% ddH_2O/0.1% TFA.

2.3 Computational Methods

2.3.1 All-atom modeling

Given the large size of each PGG-PTX molecule, AA MD simulations were carried out in implicit solvent. To run AA MD simulations of a PGG-PTX molecule in explicit solvent of the same system size would require an extraordinary amount of CPU power and computational time that are unfeasible for the scope of this study. Given the relatively flexible nature of PGG-PTX, we believe there would be minimal difference in the resulting structures from running AA MD simulations in implicit solvent vs. explicit solvent. In addition, GROMACS is only capable of running CG MD simulations with explicit solvent, not implicit solvent.

2.3.1.1 Model construction

The initial structures and input files were generated using the *xleap* module of AMBER 9.0. Paclitaxel was taken from the Protein Data Bank (PDB ID: IJFF).[34] For the amino-terminus glutamyl-glutamate (GG_{NH3+}), glutamyl-glutamate (GG), carboxyl-

terminus glutamyl-glutamate (GG_{COO-}), and glutamyl-glutamate paclitaxel (GG-PTX) residues, the atom-centered point charges were generated using the Gaussian (g03)[35] program's geometry optimization and restrained electrostatic potential fitting (RESP) calculations.[36] Specifically, hydrogen atoms were added to the carboxyl groups to achieve the ionization state of the protonated molecules. The molecules were then optimized using the AM1 geometry scheme followed by the HF/6-31G* and HF/6-31G** pop=mk iop(6/33=2) *ab initio* level calculations to obtain the electrostatic potential using Gaussian. Finally, RESP fitting was applied on the electrostatic potentials to derive the equivalent partial atomic charges for the molecules.

2.3.1.2 Energy minimization and MD simulation

These steps were carried out using the *sander* module. The starting structures were minimized in implicit solvent using the modified Generalized-Born model of IGB=2[37] and the LPCO model[38] using 250 steps of steepest descent followed by 1750 steps of conjugate gradient. To mimic the salt concentration of blood plasma and PBS buffer, the ionic strength of the implicit solvent was set to 140 mM. No periodic boundary conditions were applied. A non-bonded electrostatic cutoff of 16.0Å was used. Trajectory snapshots were saved every 100 steps for later reprocessing.

MD simulations were carried out using AMBER 9.0 with the modified version (ff99SB)[39] of the Cornell et al. parm99[30] and GAFF force fields.[31] MD simulations were carried out in the NVT ensemble (in which the number of atoms N, volume V, and temperature T were fixed) at 310K in an implicit solvent using the modified Generalized-Born model of IGB=2 and the LPCO model. No periodic boundary conditions were applied. Newton's equations of motions were integrated with a time step of 2 fs. All

bonds involving hydrogen atoms were constrained using the SHAKE algorithm[40]. Constant temperature scaling was also applied with a time constant of 0.5 ps. Langevin dynamics was used with a collision frequency of 2.0 ps^{-1}. The rotational and translational degree of freedom about the center of mass was eliminated. Trajectory snapshots were saved every 100 steps for later reprocessing. Each cycle of the MD simulation was run for 0.1 ns, and this step was repeated until a statistical equilibrium was reached at 100 ns.

2.3.2 Coarse-grained modeling

For the sake of minimizing computational costs as well as accessing longer length and time scales, the level of information in each AA PGG-PTX molecule was reduced while striving to maintain the accuracy of the physicochemical information of each molecule. Given the amino acid-based nature of the glutamyl-glutamate backbone, the MARTINI force field was selected for the CG parameterization for its successful application to proteins by experimental validation of their structural properties as well as the reproduction of thermodynamics.[32, 41-43] The MARTINI force field dictates that a group of roughly 4-5 atoms are represented as an interaction center, or bead. These beads interact through a set of short-ranged Lennard-Jones potentials to reproduce characteristic properties resulting from AA simulations. Charged groups interact via a Coulombic energy function, and bonded potentials are used to describe the chemical connectivity of the beads. Detailed parameterization of the GG_{NH3+}, GG, GG_{COO-}, and GG-PTX residues as well as water (W) and sodium (Na+) ions are described below.

2.3.2.1 Theory

The CG beads are considered as point masses, and their dynamics are described by Newton's equations of motion. The effective bonded and nonbonded interactions among the beads are described by a potential of the form, adapted from Marrink et al.[43]:

$$V = \sum_m \left[V^m_{bond} + V^m_{angle} + V^m_{dihedral} \right] + V^m_{nonbonded} \quad (2)$$

where the index *m* denotes one of the six components in the system: GG_{NH3+}, GG, GG_{COO-}, GG-PTX, W, and Na+. The sum in Eqn. (2) describes the force potentials for the bonded CG beads: V^m_{bond} describes the forces between two bonded CG beads; V^m_{angle} accounts for the forces used to sustain angles between sets of three bonded CG beads; and V^m_{angle} corresponds to the dihedral angle potential for quadruples of bonded CG beads. The $V^m_{nonbonded}$ term accounts for the nonbonded interactions between all of the CG beads in the system.

Bonded interactions are characterized as one of the following:

$$V^m_{bond} = \sum_{ij} \tfrac{1}{2} K^m_{ij} \left(R^m_{ij} - L^m_{ij} \right)^2 \quad (3)$$

$$V^m_{angle} = \sum_{ijk} \tfrac{1}{2} K^m_{ijk} \left[\cos\left(\theta^m_{ijk}\right) - \cos\left(\Theta^m_{ijk}\right) \right]^2 \quad (4)$$

$$V^m_{dihedral} = \sum_{ijkl} K^m_{ijkl} \left[1 + \cos\left(n\chi^m_{ijkl} - \delta^m_{ijkl} \right) \right] \quad (5)$$

where the indices *i, j, k,* and *l* represent four consecutive beads, R^m_{ij} is the distance between two consecutive beads *i* and *j*, L^m_{ij} is the equilibrium CG bond length (or the average of all the sampled conformations from the atomistic MD trajectory), θ^m_{ijk} is the

angle between beads *i*, *j*, and *k*, and $\Theta_{ijk,0}^{m}$ is the equilibrium angle (the average of all the sampled conformations from the atomistic MD trajectory). The CG bead distance force constants (K_{ij}^{GG} and K_{ij}^{GG-PTX}) and the CG bead angle force constants (K_{ijk}^{GG} and K_{ijk}^{GG-PTX}) depend on the bead type and bead interaction.

The nonbonded interactions between two CG beads *m* and *n* at a distance r_{mn} interact via a van der Waals (vdW) characterized by a Lennard-Jones 12-6 potential energy function as well as a Coulombic potential for charged beads (bead type Q):

$$V_{nonbonded} = \sum_{m,n} 4\varepsilon_{mn}\left[\left(\frac{\sigma_{mn}}{r_{mn}}\right)^{12} - \left(\frac{\sigma_{mn}}{r_{mn}}\right)^{6}\right] + \sum_{m,n}\frac{q_m q_n}{4\pi\varepsilon_0 \varepsilon r_{mn}} \qquad (6)$$

where σ_{mn} refers to a typical closest distance of approach between two beads *m* and *n*, ε_{mn} denotes the strength of the interactions between beads *m* and *n* (one of five levels, I to V, for each bead type, and the full interaction matrix is provided in Marrink et al.[32] q_m and q_n are the charges of the *m*th and *n*th beads, ε_0 is the vacuum dielectric permittivity, and a relative dielectric constant of $\varepsilon = 15$ is assumed for all electrostatic interactions.

2.3.2.2 CG mapping

As aforementioned, the MARTINI force field dictates that approximately 4-5 heavy atoms are mapped to one interaction center (bead). An exception to this rule applies to aromatic groups, such as the benzene molecules in paclitaxel: in order to preserve the geometric symmetry of these groups, a 2 heavy atoms-to-1 bead mapping scheme is applied. The CG mapping of the GG_{NH3+}, GG, GG_{COO-}, and GG-PTX residues

Table 2.1. Coarse-grained topologies for GG_{NH3}, GG, GG_{COO-}, and GG-PTX residues

GG Backbone topology

i j	Bond length L_{ij}^{m} [nm]	Force constant K_{ijk}^{GG} [kJ nm^{-2} mol^{-1}]	*i j k*	Bond angle Θ_{ijk}^{m} [º]	Force constant K_{ijk}^{GG} [kJ nm^{-2} mol^{-1}]
G1 G1	0.350*	200*	G1 G1 G1	127*	25*

GG Sidechain Topology (includes GG_{NH3+} and GG_{COO-} residues)

i j	Bond length L_{ij}^{m} [nm]	Force constant K_{ijk}^{GG} [kJ nm^{-2} mol^{-1}]	*i j k*	Bond angle Θ_{ijk}^{m} [º]	Force constant K_{ijk}^{GG} [kJ nm^{-2} mol^{-1}]
G1 G2	0.393	7500*	G1 G2 G3	143	100*
G2 G3	0.381	7500*	G2 G3 G4	85	100*
G3 G4	0.366	7500*			

GG-PTX Sidechain Topology

i j	Bond length L_{ij}^{m} [nm]	Force constant [kJ nm^{-2} mol^{-1}]	*i j k*	Bond angle Θ_{ijk}^{m} [º]	Force constant K_{ijk}^{GG} [kJ nm^{-2} mol^{-1}]
D1 D2	0.374	7500*	D1 D2 D3	153	100*
D2 D3	0.387	7500*	D2 D3 D4	94	100*
D3 D4	0.406	7500*	D3 D4 D5	130	100*
D4 D5	0.357	7500*	D4 D5 D6	84	100*
D5 D6	0.258	7500*	D4 D5 D13	146	100*
D6 D7	0.353	7500*	D5 D6 D7	107	100*
D6 D10	0.318	7500*	D5 D6 D10	75	100*
D5 D13	0.198	7500*	D5 D13 D14	80	100*
D13 D14	0.227	7500*	D5 D13 D23	158	100*
D7 D8	0.270*	1000*	D6 D7 D8	173	100*
D7 D9	0.270*	1000*	D6 D7 D9	109	100*
D8 D9	0.270*	1000*	D6 D10 D11	143	100*
D10 D11	0.270*	1000*	D6 D10 D12	105	100*
D10 D12	0.270*	1000*	D13 D14 D22	95	100*
D11 D12	0.270*	1000*	D13 D14 D15	127	100*
D13 D23	0.223	7500*	D13 D22 D24	85	100*
D14 D23	0.342	7500*	D14 D23 D22	60	100*
D14 D15	0.382	7500*	D14 D15 D16	52	100*
D15 D16	0.519	7500*	D14 D15 D17	36	100*
D15 D17	0.609	7500*	D15 D17 D22	53	100*
D17 D18	0.578	7500*	D15 D17 D18	85	100*
D18 D19	0.289	7500*	D15 D17 D19	48	100*
D17 D19	0.469	7500*	D16 D17 D24	31	100*
D17 D22	0.138	7500*	D17 D19 D21	120	100*
D19 D20	0.349	7500*	D18 D19 D20	115	100*
D19 D21	0.249	7500*	D18 D19 D21	121	100*
D22 D24	0.368	7500*	D18 D17 D19	30	100*
D22 D23	0.369	7500*	D22 D18 D19	54	100*
D24 D25	0.238	7500*	D22 D19 D20	105	100*
D25 D26	0.270*	1000*	D22 D24 D25	125	100*
D25 D27	0.270*	1000*	D23 D22 D13	75	100*
D26 D27	0.270*	1000*	D23 D22 D24	96	100*
			D24 D25 D26	128	100*
			D24 D25 D27	165	100*

*Taken from the predetermined values for backbone or sidechain bonded parameters from the MARTINI force field.

are depicted in Fig. 2.3. Given that the circular dichroism spectroscopy results show that PGG-PTX forms a random coil at 37ºC (310 K), the bonded parameters of the GG backbone were assigned based on the values for a random coil, as dictated by the MARTINI force field. For the negative and positive controls, description of the CG mapping for glutamate (G) and glutamate-benzene (G-B) residues is provided in Fig. 2.11. In addition, four water molecules are represented as a single P_4 type bead, and each Na+ ion is represented by a single Q type bead with a +1 charge.

2.3.2.3 Parameterization of bonded interactions for a PGG-PTX molecule

The equilibrium bond distances and angles were obtained from of the three 'random' PGG-PTX molecules (f_{PTX} = 0.18, 0.24, and 0.37) since they were the models that best mimic the experimental formulations of PGG-PTX. The parameterization was carried out by first extracting the time-dependent bond distances and angles from the 100 ns AA MD simulations using *ptraj* module of AMBER 9.0. Then, the bonded parameters were processed using the Boltzmann inversion procedure[44] in MATLAB 7.0[45] to determine the equilibrium bond distances and angles (see Table 2.1).

2.3.2.4 Energy minimization and MD simulation

CG PGG-PTX models were constructed in GROMACS 4.0.3. Each PGG-PTX molecule was solvated in the center of the box with explicit W beads surrounding the molecule in 2 nm of thickness. Due to the negative charges imparted by the GG and GG-PTX residues in each system, Na+ ions (usually 234) were added in place of W beads to neutralize the system. The simulations were carried out under NPT (the number of

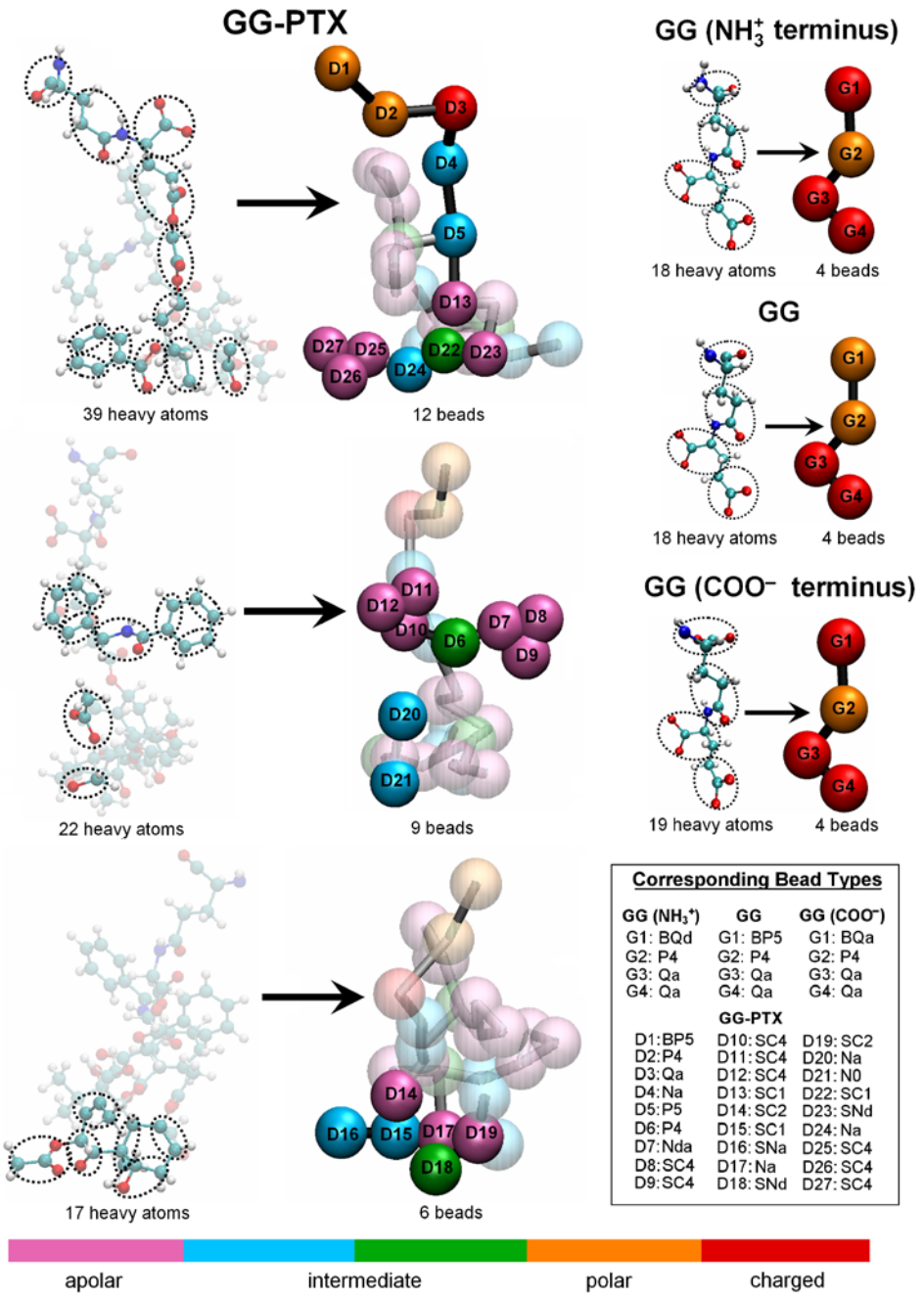

Figure 2.3. Coarse-grained representations of GG and GG-PTX residues. Mapping of the AA models to CG models was done according to the MARTINI force field. Roughly 4-5 heavy atoms were assigned to one interaction center, or "bead". (For the aromatic groups in Paclitaxel, the assignment was 2 heavy atoms to 1 bead.) GG was reduced from 18 or 19 heavy atoms to 4 beads, and GG-PTX was reduced from 148 heavy atoms to 27 CG beads. Differently colored beads represent different bead types, based on polarity and hydrogen-bonding capabilities. For each bead, four main types are considered: polar (P), nonpolar (N), apolar (C), and charged (Q). Each main type can subsequently be distinguished by its degree of polarity (from 1 = lowest polarity to 5 = highest polarity) and its hydrogen-bonding abilities (denoted by a letter: donor (d), acceptor (a), both (da), or none (0)). Beads with nomenclature beginning 'B' and 'S' letters denote a backbone bead and an aromatic bead, respectively.

particles N, pressure P, and temperature T were fixed) conditions. For each simulation, the temperature was kept constant at 310 K with a coupling constant of τ_T = 0.1 ps, and the pressure was weakly coupled to 1 bar with a relaxation time of τ_P = 0.5 ps. The cutoff length for the nonbonded interactions is r_{cut} = 1.2 nm. Lennard-Jones forces were considered for r_{cut} < 0.9 nm and Coulombic forces for r_{cut} < 1.2 nm. The latter was computed every time step for 1.0 nm and once every 10 time steps for 0.9 nm < r_{cut} < 1.2 nm. The time step in the leap-frog integration scheme was 5 fs. The energies, coordinates and velocities were written every 0.5 ps. For each of the eighteen systems, MD simulations were run until a statistical equilibrium was obtained at 200 ns. It is worth noting that, due to the smoothness of the CG potentials, CG dynamics are actually faster than AA interactions. To account for this difference, researchers have approximated CG results by scaling the time axis by a conversion factor of four, the effective speed up factor in the diffusional dynamics of CG water compared to that of real water.[32, 43, 46] Therefore, the effective time sampled for each CG MD simulation was roughly 800 ns. Unless otherwise stated, the CG MD simulation times reported in this paper are effective times.

2.4 Results and Discussion

2.4.1 Circular dichroism spectroscopy

To construct a theoretical model of PGG-PTX practical for clinical applications, its initial molecular configuration needs to be first defined. Circular dichroism spectroscopy was used to determine the general structure of a PGG-PTX molecule, and

the resulting structure was regarded as the initial configuration for the AA PGG-PTX models.

Fig. 2.4 shows the CD spectra of 1mg/ml PGG-PTX at f_{PTX} = 0.18, 0.24, and 0.37, all dissolved in 1X DPBS. All three curves are most representative of a random coil at physiological temperature of 37ºC. The negative control of 1X DPBS at 37ºC indicates that that there is no signal interference that may have influenced the conditions while CD spectra of PGG-PTX were being taken. For the positive control, the shape of the alpha-helical FD protein, a bZIP transcription factor in a floral pathway[47], in 50% TFE/50% ddH_2O/0.1% TFA buffer does indeed correspond to an alpha-helix, as compared with the CD spectrum of the alpha-helical poly-γ-tyrosine.[48] The lowest part of the curve is ~215nm and the highest point of the curve is ~200nm collectively indicate that the FD protein is indeed alpha-helical. This data shows that PGG-PTX exists as a random coil.

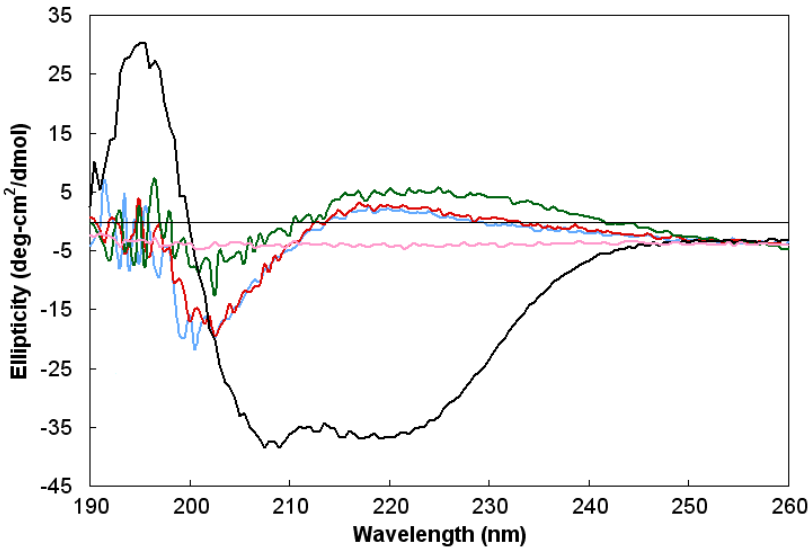

Figure 2.4. CD spectra of samples. Shows the spectra for PGG-PTX at f_{PTX} = 0.18 *(blue line)*, PGG-PTX at f_{PTX} = 0.24 *(red line)*, PGG-PTX at f_{PTX} = 0.37 *(green line)*, FD protein *(black line)*, and pure 1X DPBS *(pink line)*.

For these three samples, it is most likely that the spatial PTX arrangement resembles the PTX arrangement in the 'random' configurations. Therefore, regardless of the PTX loading fraction, PGG-PTX lacks secondary structure and exists primarily as a random coil. Finally, the molecular configuration of PGG-PTX as a random coil does not impose any stipulations on construction of an AA model.

2.4.2 Comparison of all-atom and coarse-grained models

Fig. 2.5 shows the initial structures of the AA and CG models at of PGG-PTX molecule at f_{PTX} = 0.37 with an 'even' PTX distribution. Neglecting the explicit solvent beads of the CG models, the size of the AA models (6189 heavy atoms) is roughly five times larger than its CG counterpart (1222 beads), which is apparent in that the AA model appears to have a higher image resolution than the CG model. Despite this difference, the structural integrity of the PGG-PTX molecule is still preserved in the CG model. From the perspectives of the *xy* and *xz* planes, the length and height of the AA and CG models are comparable, and the cross-sectional area is similar in AA and CG models from the *yz* plane. The paclitaxel molecules are arranged in a spiral fashion around the PGG backbone, similar to the spiral pattern in the AA model.

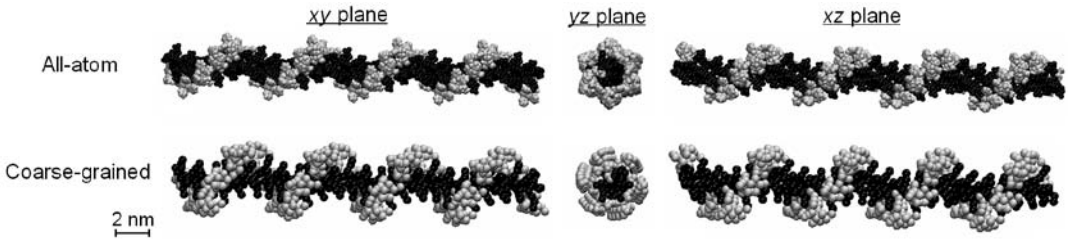

Figure 2.5. AA and CG models of a PGG-PTX molecule. Shows the models for a f_{PTX} = 0.37 molecule with an 'even' PTX distribution. The GG *(black)* and PTX *(grey)* residues are portrayed.

2.4.2.1 AA and CG equilibrium bonded parameters

To assess the validity of the CG model of PGG-PTX, a few equilibrium bond angles (G1-G2-G3, D3-D4-D5, D13-D14-D23, and D24-D25-D37) of the AA and CG PGG-PTX models were selected and compared. As shown in Fig. 2.6, it is apparent that there is relatively good agreement between the AA and CG values. While there is not always a perfect overlap between the AA and CG curves, this behavior is to be expected for a system that has both flexible and rigid components. The AA and CG probability distributions for D13-D14-D23 and D24-D25-D27 are narrower than those for G1-G2-G3 and D3-D4-D5. An explanation for this difference is that the D13, D14, D23, D24, D25, and D27 beads are located in an area of the paclitaxel molecule with high sterical energy (D13, D14, D23, D25, and D26 are part of aromatic groups) thus limiting the range of orientations that the beads can sample. Contrariwise, G1, G2, G3, D3, D4, and D5 are not bound to any aromatic structures, not to mention that they are within close vicinity of the glutamyl-glutamate backbone. The positions of these beads allow for a larger range of accessible orientations. In all, the probability distribution curves show that more flexible components of a PGG-PTX molecule have a wider range of accessible conformations, while more rigid components of a PGG-PTX molecule have a limited range of accessible conformations.

2.4.2.2 RMSD and RMSF values

Figs. 2.16, 2.17, and 2.18 show the RMSD time evolutions from 100-ns AA MD and 100-ns (or 25 ns non-effective time) CG MD simulations of PGG-PTX molecules. It is apparent that there is relatively good agreement between the AA and CG RMSD values. Overall, the AA RMSD values rise to 3-5 nm by 100 ns, and CG RMSD values

increase to 2-4 nm by 100 ns. Although these values are high, they are reasonable given the size of the PGG-PTX molecules. By 100 ns, most AA MD simulations have attained a steady-state level. (While certain systems such as the f_{PTX} = 0.18 'clusters', f_{PTX} = 0.18 'even', and f_{PTX} = 0.24 'even' molecules have not yet attained a full steady-state level, they are adequately stabilized for this study.) On the other hand, the CG MD simulations did not attain a steady-state by 100 ns and were subsequently extended to 800 ns. To assess whether steady-state was reached by 800 ns, CG MD simulations were extended further to an effective time of 2 μs. Fig. 2.7 shows the CG RMSD values for all eighteen systems; most plots show that there is minimal variation in RMSD between 800 ns and 2 μs, indicating that 800 ns was long enough for a statistical equilibrium to be reached.

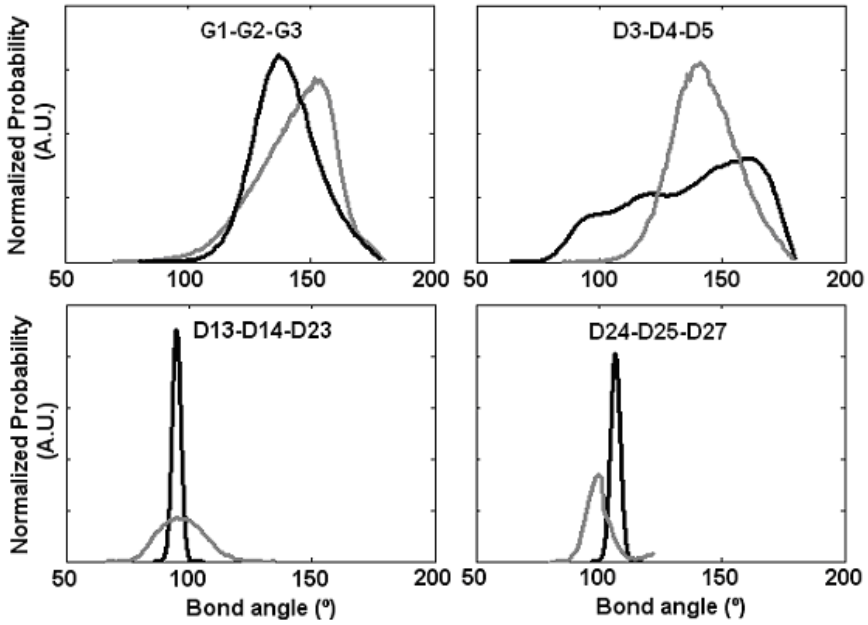

Figure 2.6. Selected probability distributions of AA and CG bond angles between PGG-PTX atom groups. Information was extracted from 100 ns AA MD and 100 ns CG MD simulations. Shows data for AA *(black line)* and CG models *(grey line)*.

Figs. 2.19, 2.20, and 2.21 show the RMSF (by residue) values from 100 ns AA MD and 100 ns (or 25 ns non-effective time) CG MD simulations of PGG-PTX

molecules. There is relatively good agreement between the AA and CG RMSF values. The AA RMSF values typically fluctuated between 2-4 nm, with a few molecules having RMSF values near 8 nm. The CG RMSF values are a bit lower by ~1-3 nm. This discrepancy is expected, given that some structural information was probably lost in the coarse-graining procedure and that the system is comprised of the flexible PGG polymer. Fig. 2.8 shows the CG RMSF values for all eighteen PGG-PTX molecules. Nearly all molecules fluctuate between 2-4 nm, regardless of the spatial PTX arrangement or PTX loading fraction. RMSF is also an indication of molecular flexibility; since higher RMSF values typically correspond to segments of PGG-PTX with unconjugated PGG (no paclitaxel molecules attached), those regions are the most flexible. The distribution of hydrophobic PTX on the PGG backbone influences the degree of residue fluctuation, which is further discussed below.

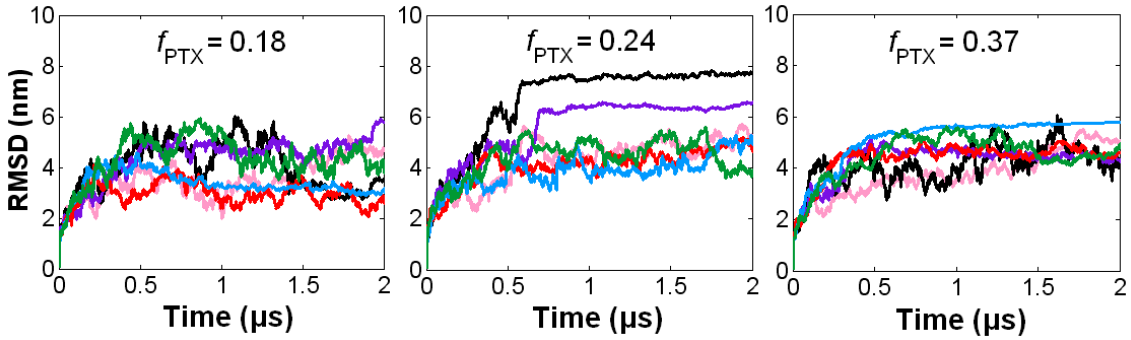

Figure 2.7. CG RMSD time evolutions of PGG-PTX molecules. PTX distributions include 'clusters' *(pink line)*, 'ends' *(black line)*, 'even' *(purple line)*, 'middle' *(red line)*, 'random' *(blue line)*, and 'side' *(green line)*.

2.4.3 Molecular conformation of a PGG-PTX molecule

2.4.3.1 Shape

It was of interest to investigate whether the shape of PGG-PTX can be predicted using multiscale modeling. Fig. 2.9 shows the 800 ns CG MD simulations for the PGG-PTX

molecules. All molecules start out as linear at 0 ns and eventually adopt a coil (filamentous) or globular (round) shape by 800 ns. Since steady-state was attained by all systems by 800 ns, the shape at this time was regarded as the official shape of each PGG-

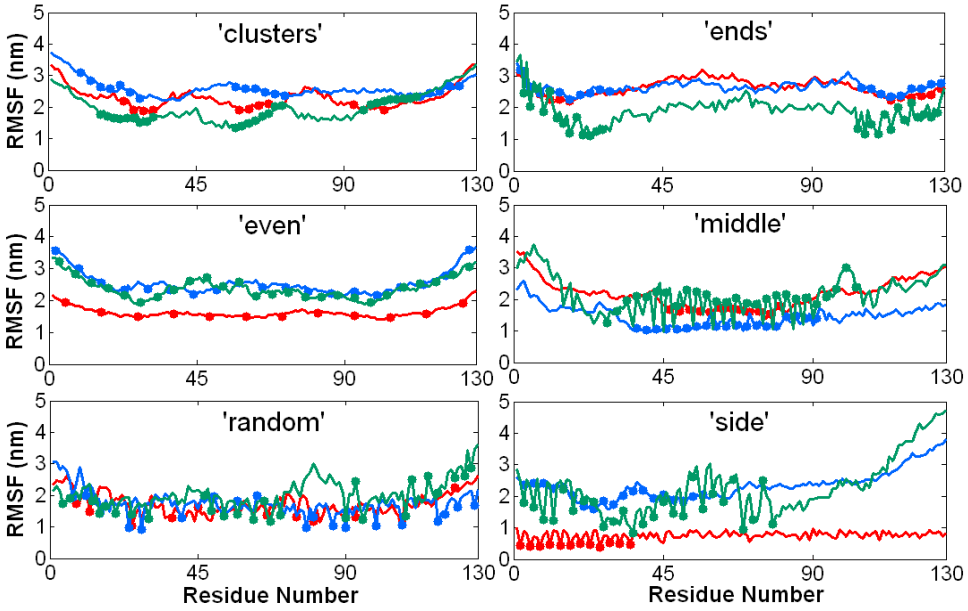

Figure 2.8. CG RMSF trajectories of PGG-PTX molecules. Shows data for f_{PTX} = 0.18 *(red line)*, f_{PTX} = 0.24 *(blue line)*, and f_{PTX} = 0.37 *(green line)* molecules. All trajectories were extracted from the 800 ns effective time CG MD simulations.

PTX molecule. There exists a wide variety of geometries among the molecules. The molecular shape of each molecule can be categorized into two main types: coil (filamentous, wormlike) and globular (round). For each type, the conformation can be further characterized as one or more subtypes (coil: angular, dense, extended, horseshoe, or dumbbell, globule: spherical and toroidal). Descriptions of the geometries are summarized in Table 2.2.

Table 2.2. Descriptions of geometries of a PGG-PTX molecule	
Coil (linear, filamentous)	
Dense	Short, distance between NH_3^+ and COO^- termini is < 10 nm
Extended	Long, distance between NH_3^+ and COO^- termini is > 10 nm
Angular	Characterized by one sharp turn
Horseshoe	Characterized by one major curved turn
Dumbbell	Characterized by two linked spherical globules
Globule (round)	
Spherical	Shaped like a ball
Toroidal	Shaped like a ring or donut

The coil was the most popular type of geometry among all PGG-PTX molecules. All molecules with PTX loading fractions of 0.18 and 0.37 are coils, and at f_{PTX} = 0.24, four of the six molecules are coils, whereas the other two are globules. The f_{PTX} = 0.24 set also has the most diverse set of subtype geometries. All six subtypes are prevalent in the f_{PTX} = 0.24 molecules, including the spherical globule and toroidal globule that are not apparent in the f_{PTX} = 0.18 and f_{PTX} = 0.37 molecules. This evidence suggests that, out of the three PTX loading fractions, PGG-PTX at f_{PTX} = 0.24 has the optimal balance of hydrophobic and hydrophilic forces to have the greatest concomitant effect on the geometry of the molecule. That is, at f_{PTX} = 0.24, the geometry of PGG-PTX is influenced more by the spatial positioning of PTX on the PGG backbone, rather than the PTX loading fraction. On the other hand, at f_{PTX} = 0.18 and 0.37, the geometries of PGG-PTX is more influenced by the mass fraction of hydrophobic PTX and hydrophilic PGG, rather than the spatial positioning of PTX on the PGG. In addition, there are certain spatial PTX arrangements for whose geometries are the least affected by the PTX loading fraction.

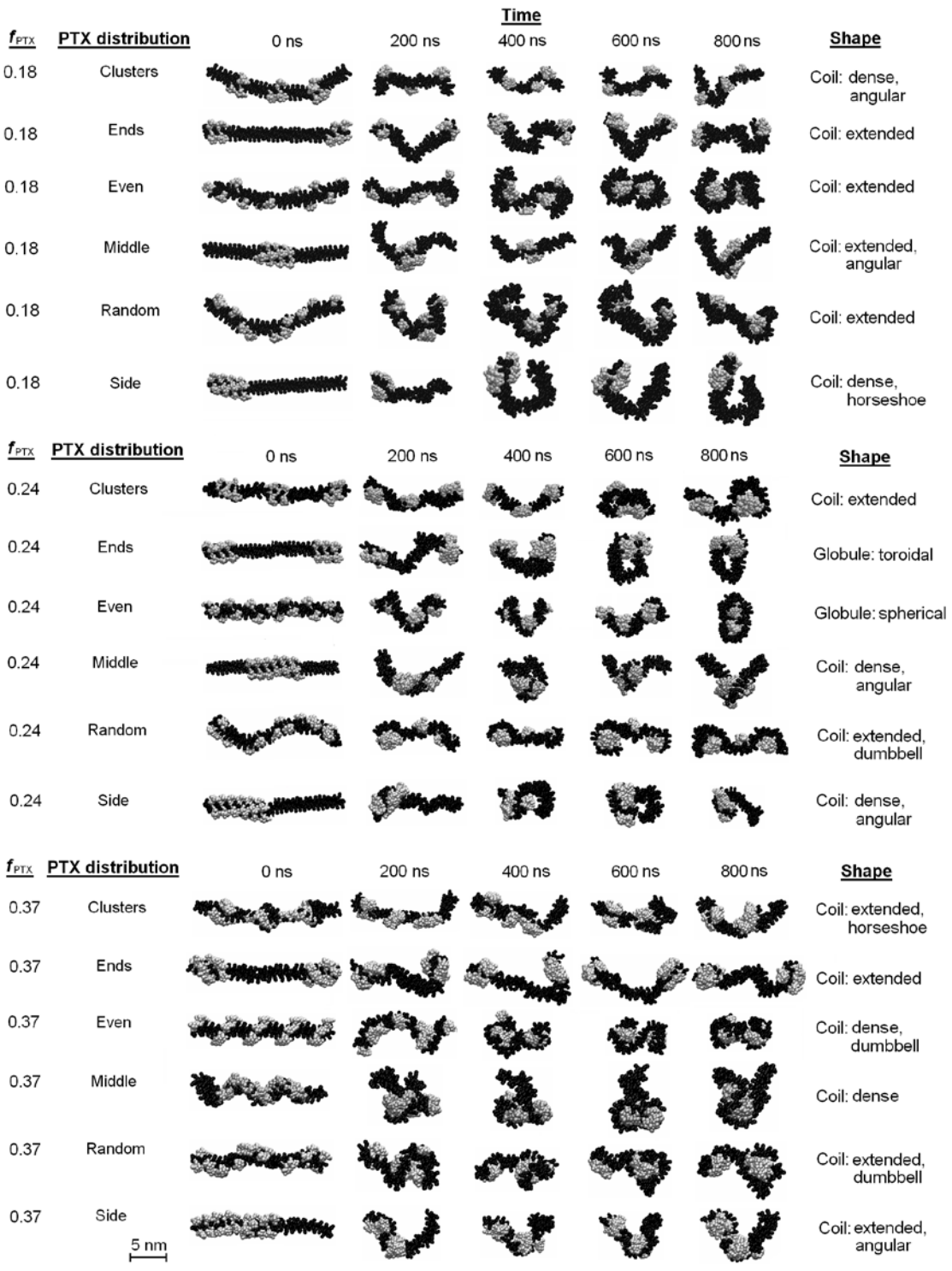

Figure 2.9. CG MD simulations of PGG-PTX molecules. Portrays the glutamyl-glutamate *(black)* and paclitaxel *(grey)* molecules. Explicit water molecules and Na+ ions are not shown.

Such is the ‘middle’ configuration, which maintains a dense coil for all three PTX loading fractions, and the ‘random’ configuration, which maintains an extended coil regardless of the PTX loading fraction. (This shape for the ‘random’ configuration is in good agreement with the previous circular dichroism spectroscopy data on PGG-PTX that indicate that the shape of PGG-PTX is a random coil.) It is also interesting that the ‘side’ and ‘middle’ configurations are unique in that they are characterized by sharp curvature: possessing an angled or curved turn. This behavior is most likely attributed to the spatial PTX arrangement on the PGG backbone, which has a major influence on the flexibility of a PGG-PTX molecule. What sets the ‘middle’ and ‘side’ configurations apart from the rest is that all of the PTX molecules are concentrated into one group such that it leaves long, uninterrupted portions of the PGG backbone unconjugated. These unconjugated portions are floppy and more flexible than the segments of the PGG backbone with PTX molecules attached. A similar pattern is also emergent in the f_{PTX} = 0.24 ‘ends’ molecule, a toroidal globule: two groups of paclitaxel molecules located at each end, thus leaving the middle portion of the PGG backbone unconjugated. As for other configurations like ‘clusters’, ‘random,’ and ‘even’, the paclitaxel molecules are arranged more uniformly along the PGG backbone such that the portions of unconjugated PGG are much shorter (see Fig. 2.2). This relatively equal dispersion of hydrophobic forces minimizes the movement or fluctuation of the PGG-PTX molecule as a whole. For the ‘middle’ and ‘side’ configurations, this absence of hydrophobic drug molecules removes the sterical hindrance imposed by the rigid PTX molecules and thus allows the unconjugated PGG portion to move about more freely. Generally speaking, configurations that have longer unconjugated PGG segments (‘middle’, ‘side’, and

'ends') tend to be more flexible and form more definitive, structured shapes as compared to configurations with a more even PTX distributions along the PGG backbone ('clusters', 'random', and 'even').

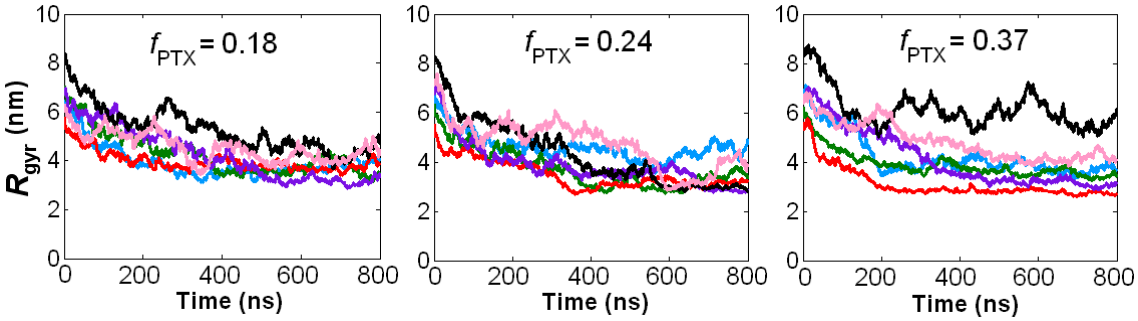

Figure 2.10. Radius of gyration time evolutions of PGG-PTX molecules. PTX distributions include 'clusters' *(pink line)*, 'ends' *(black line)*, 'even' *(purple line)*, 'middle' *(red line)*, 'random' *(blue line)*, and 'side' *(green line)*.

2.4.3.2 Size

It was also of interest to examine the effects of PTX loading fraction and the spatial PTX arrangement on the size of a PGG-PTX molecule. Fig. 2.10 shows the 800 ns CG MD time evolutions of the radius of gyration (R_{gyr}) for all 18 PGG-PTX molecules. There are several interesting trends apparent. It is evident that, at t = 0 ns, the R_{gyr} of most molecules is ~6-8 nm, and over the 800 ns trajectory, each of the 18 PGG-PTX molecules decreased nearly 50% from its initial R_{gyr}. Fig. 9 confirms that, at t = 0 ns, all structures were stretched out and extended, but by t = 200 ns, all of them had shrunken in size. Also, it is interesting to see that, as the PTX loading fraction increases, the greater the variability in R_g among each set of six PGG-PTX configurations. As shown in Fig. 10, at f_{PTX} = 0.18, there is quite some overlap between the plots, especially at 800 ns, indicating that all six f_{PTX} = 0.18 configurations have more or less the same size. At f_{PTX} = 0.24, there is slightly less overlap in the plots, and at f_{PTX} = 0.37, there is

nearly no overlap at all. Suffice to say, higher PTX loading fractions most likely results in a larger range of candidate sizes of PGG-PTX. In addition, the degree of influence the spatial PTX arrangement on PGG exerts over the size of a PGG-PTX molecule is quite minimal. Regardless of the hierarchy of initial R_{gyr} at t = 0 ns (from smallest to largest R_{gyr}: 'middle', 'side', 'random', 'clusters', 'even', and 'ends'), once the molecules have stabilized, nearly all have a final R_{gyr} of ~4 nm.

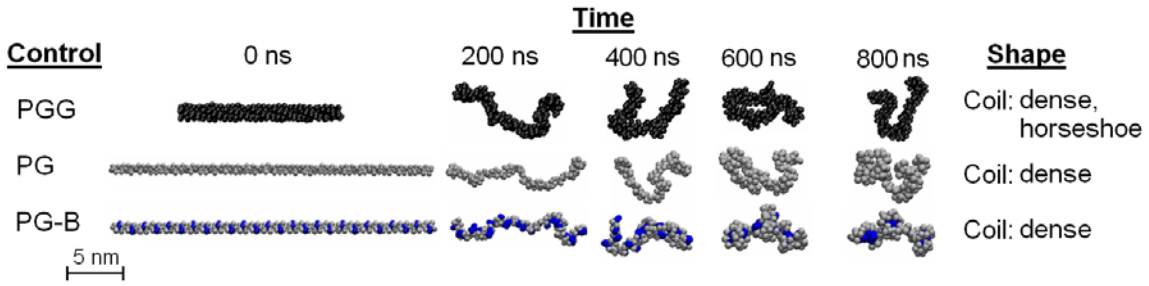

Figure 2.11. CG MD simulations of negative and positive controls. Shows the trajectories for PGG *(black)*, PG *(grey)*, and PG-B *(blue)*. Explicit water molecules and Na+ ions are not shown.

2.4.3.3 Influence of PTX on molecular conformation

The effect of the presence of paclitaxel molecules on the conformation of a PGG molecule was also of interest. To examine the extent of this effect, two negative controls (CG models of hydrophilic polymers free of any hydrophobic entities) and a positive control (CG model of a hydrophilic polymer conjugated with hydrophobic entities) were constructed. The negative controls are: a 130-mer poly-γ-glutamate molecule (PG), and a 130-mer poly-γ-glutamyl-glutamate (PGG) molecule. The positive control is a 130-mer poly-γ-glutamate molecule with covalently conjugated benzene molecules (PG-B) with a benzene loading fraction of 0.37 ($f_{benzene}$ = 0.37) and an 'even' benzene distribution. Fig. 2.11 shows the 800 ns CG MD simulations of the controls. During the 800 ns trajectory, both PG and PGG molecules wiggle around a lot, exhibiting flexible behavior. At 800

ns, they exhibit dense, horseshoe coil shapes. A similar behavior is observed in the PG-B molecule, as it also flexible and contorts before it finally adopts a dense coil at 800 ns. It is also worth noting that the benzene molecules self-assemble together to form three hydrophobic 'cores' located in the inner parts of the molecule.

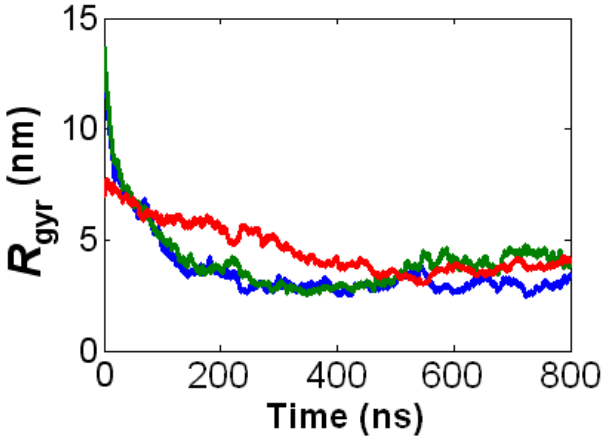

Figure 2.12. Radius of gyration time evolutions for the negative and positive controls. Includes the negative controls, PG *(red line)* and PGG *(green line)*, and the positive control, PG-B *(blue line)*. All trajectories were extracted from the 800 ns CG MD simulations.

Fig. 2.12 shows the 800 ns CG MD time evolutions of R_{gyr} for the controls. The PG and PG-B molecules both have an initial R_{gyr} ~ 13 nm and final R_{gyr} ~ 4 nm. Given that they both have coil shapes, the benzene molecules have an insignificant effect on the coil geometry of a PG molecule. Similarly, the PGG molecule and PGG-PTX molecule (f_{PTX} = 0.37, 'even' PTX distribution) each has an initial R_{gyr} ~ 7 nm and final R_{gyr} ~ 4 nm. Since both molecules are dense coils, this data suggests that, for the PGG-PTX (f_{PTX} = 0.37 'even') molecule, the presence of PTX on PGG only also has a minor influence on the conformation of PGG. It was also interesting to see how the PTX molecules in the PGG-PTX (f_{PTX} = 0.37 'even') molecule also self-assemble to form multiple inner hydrophobic 'cores', similar to the PG-B molecule.

2.4.3.4 Ability to cross physiological barriers in drug delivery

Wormlike, filamentous micelles have been shown to result a longer circulation half-life than their spherical counterparts in drug delivery,[3, 4] and discoidal particles have been shown to have a higher tendency to adhere and accumulate to the wall of tumor endothelia.[5] By analogy, the shapes of the wormlike, filamentous micelles, and discoidal particles are structurally similar to the coil-shaped PGG-PTX molecules. Since all 18 molecules adopt a general coil shape (with a variety of coil subtypes), with exception to the f_{PTX} = 0.24 'ends' and f_{PTX} = 0.24 'even' molecules, it appears that the PTX loading fraction and spatial PTX arrangement have a minor concomitant influence on the molecular conformation of a PGG-PTX molecule. By analogy to the larger micelles and nanoparticles, we speculate that PGG-PTX formulations may confer a relatively long circulation half-life and propensity for accumulation, regardless of the PTX loading fraction and spatial PTX arrangement.

2.5 Conclusions

There have been suggestions that the molecular conformation of a cancer therapeutic influences its ability to reach its intended site in the body. In this study, the conformation of PGG-PTX, a polymer-drug conjugate with potential applications in cancer therapy, was explored by systematically controlling the PTX loading fraction (f_{PTX} = 0.18, 0.24, and 0.37) and spatial patterning of PTX on PGG ('clusters', 'ends', 'even', 'middle', 'random', and 'side'). Given that the CG models accurately reproduce the bonded parameters of the AA models and the good agreement between the AA and CG RMSD and RMSF trajectories, the CG models are suitable for accessing the nanosecond-

microsecond regime. The 800 ns CG MD simulations have shown that, regardless of PTX loading fraction and PTX arrangement on PGG, a PGG-PTX molecule will most likely adopt a coil shape, suggesting that it has a long circulation half-life and high inclination to accumulate towards walls of tumor endothelia. Also, PGG-PTX molecules with less homogeneous PTX arrangements (characterized by long, unconjugated PGG sections) tend to result in geometries with higher curvature. In terms of producing the widest variety of geometries, $f_{PTX} = 0.24$ is the PTX loading fraction at which the PTX arrangements are the most sensitive to morphological change.

2.6 Supporting Information

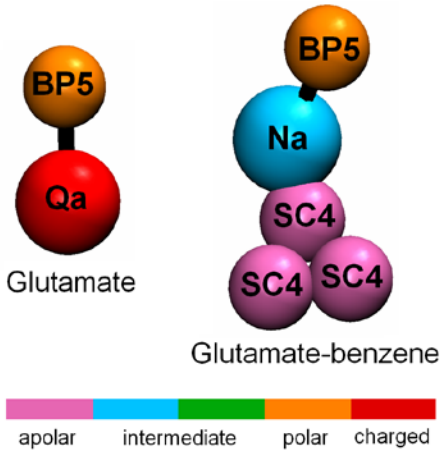

Figure 2.13. CG representations of glutamate (G) and glutamate-benzene (G-B) residues. Glutamate is coarse-grained into two beads, one as the backbone bead (BP5) and the other as the sidechain bead (Qa) bearing a charge of -1. Glutamate-benzene is coarse-grained into five molecules, three of which (SC4) represent the hydrophobic benzene ring and the other two being the backbone (BP5) and a sidechain bead (Na). Bonded parameters for the glutamate and benzene molecules are already provided in the MARTINI force field.

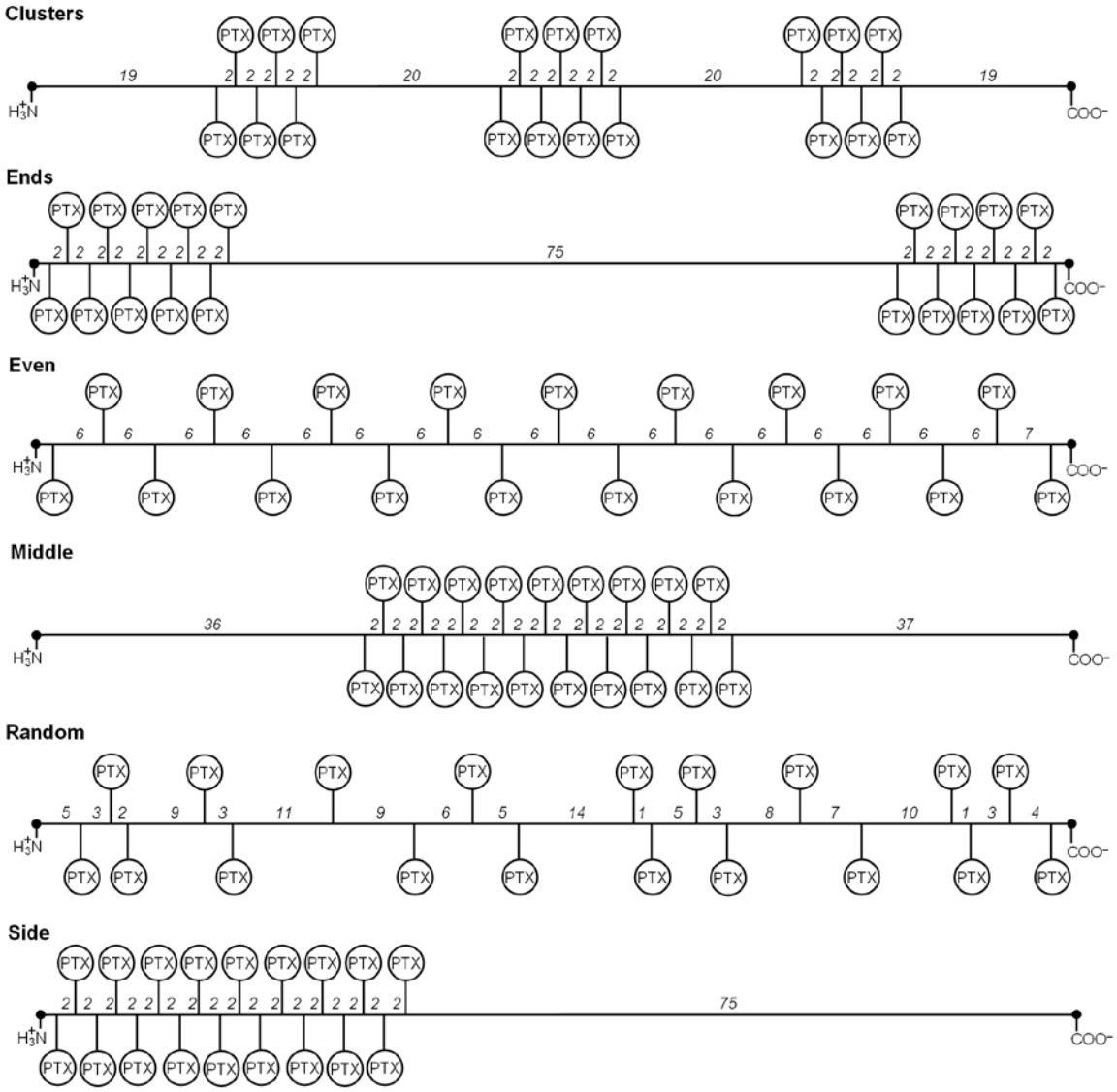

Figure 2.14. Abstract representation of the spatial PTX positioning patterns on the PGG backbone for f_{PTX} = 0.24. Each PGG-PTX molecule is composed of 130 poly-γ-glutamyl-glutamate monomers and 19 Paclitaxel molecules. Shows how 19 Paclitaxel molecules are covalently attached to the PGG backbone in six different fashions: 'clusters' (3 PTX groups with 4-5 PTX per group, spaced an equal number of residues apart), 'ends' (2 PTX groups with 9 or 10 PTX each, located at both ends), 'even' (each PTX is spaced an equal number of residues apart along PGG), 'middle' (all PTX molecules positioned in the middle), 'random' (all PTX molecules located in random positions), and 'side' (all PTX molecules located at the amino terminus end). Numbers between residues denote number of repeating GG residues that are not amino- or carboxyl-termini GG residues. The amino- and carboxyl-termini GG residues are represented by black dots at the ends of each line.

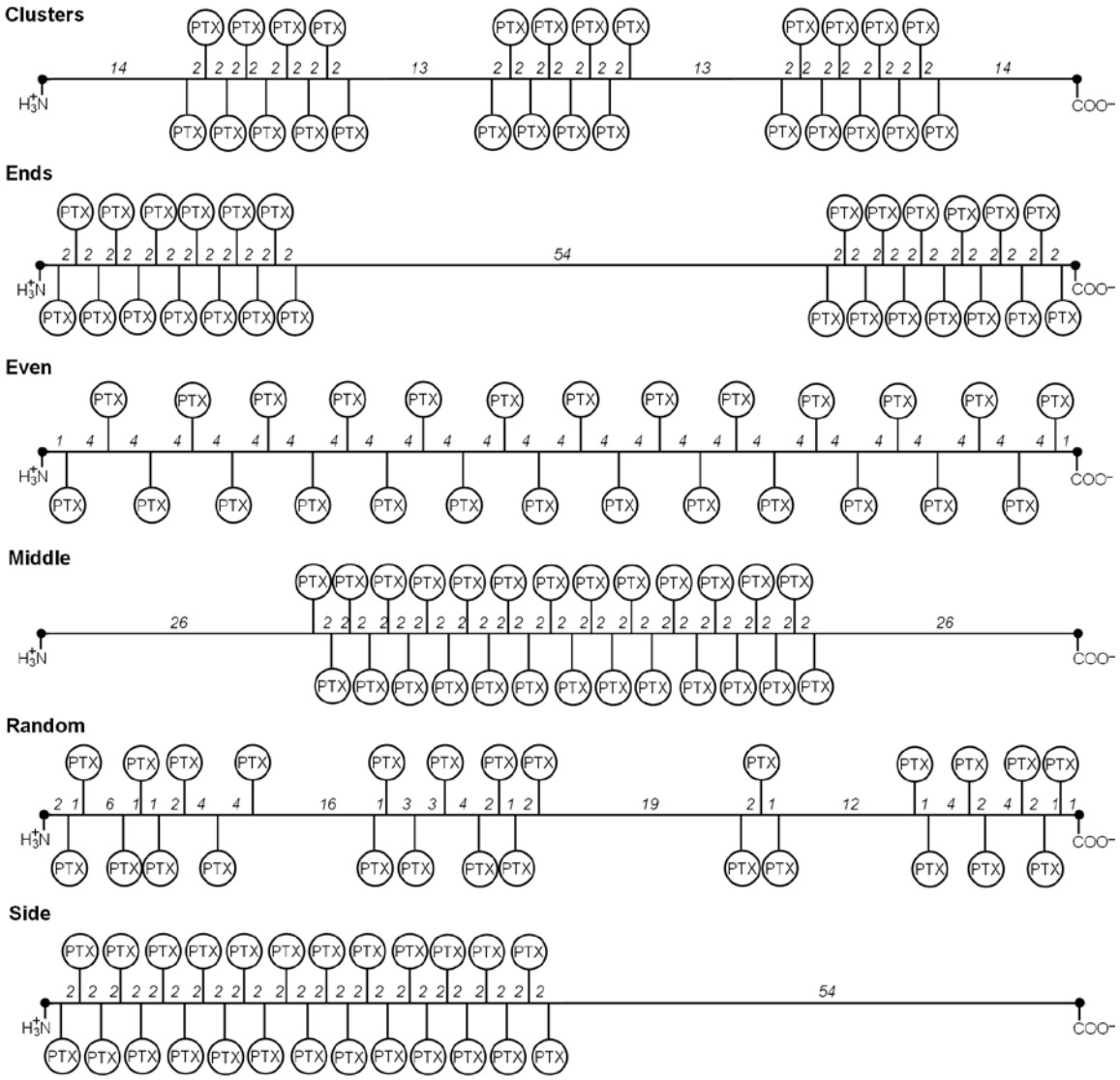

Figure 2.15. Abstract representation of the spatial PTX positioning patterns on the PGG backbone for f_{PTX} = 0.37. Each PGG-PTX molecule is composed of 130 poly-γ-glutamyl-glutamate monomers and 26 paclitaxel molecules. Shows how 26 Paclitaxel molecules are covalently attached to the PGG backbone in six different fashions: 'clusters' (3 PTX groups with 8 or 9 PTX per group, spaced an equal number of residues apart), 'ends' (2 PTX groups with 13 PTX each, located at both ends), 'even' (each PTX is spaced an equal number of residues apart along PGG), 'middle' (all PTX molecules positioned in the middle), 'random' (all PTX molecules located in random positions), and 'side' (all PTX molecules located at the amino terminus end). Numbers between residues denote number of repeating GG residues that are not amino- or carboxyl-termini GG residues. The amino- and carboxyl-termini GG residues are represented by black dots at the ends of each line.

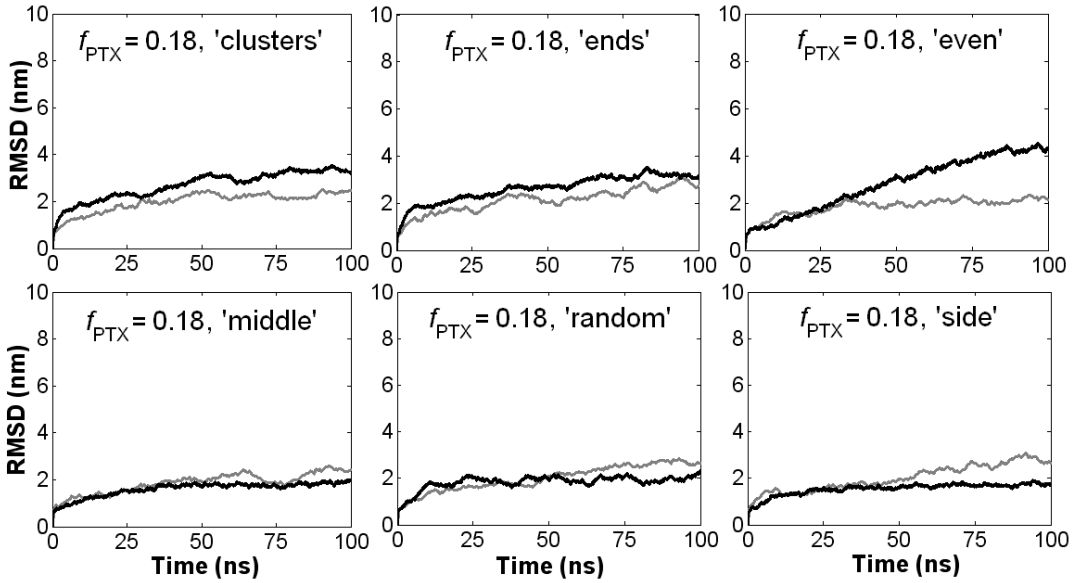

Figure 2.16. RMSD time evolutions for AA *(black line)* and CG *(grey line)* PGG-PTX molecules for f_{PTX} = 0.18. Data were extracted from the 100 ns AA MD and 25 ns CG MD simulations (non-effective timescales).

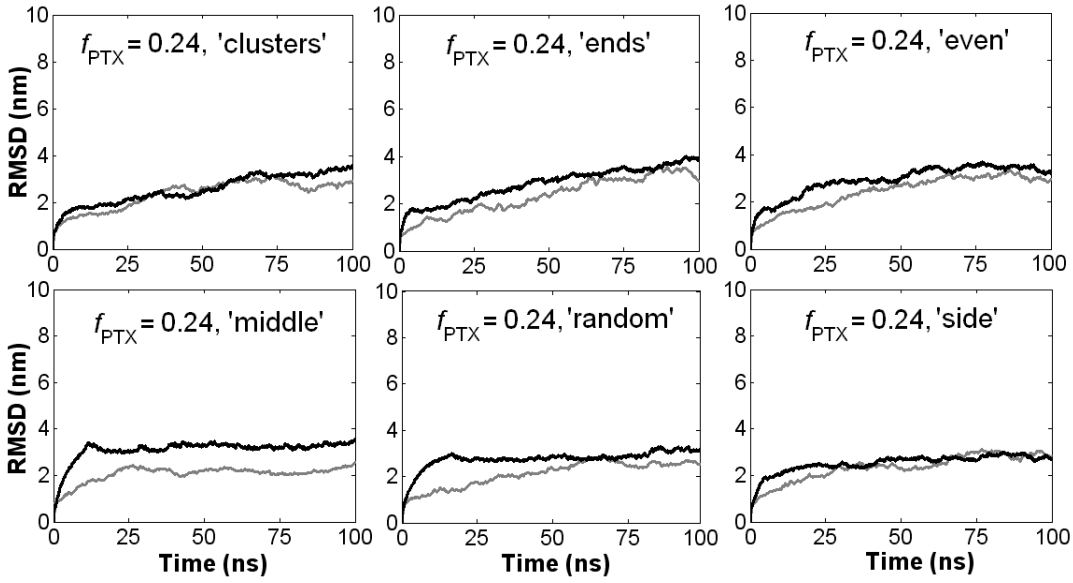

Figure 2.17. RMSD time evolutions for AA *(black line)* and CG *(grey line)* PGG-PTX molecules for f_{PTX} = 0.24. Data were extracted from the 100 ns AA MD and 25 ns CG MD simulations (non-effective timescales).

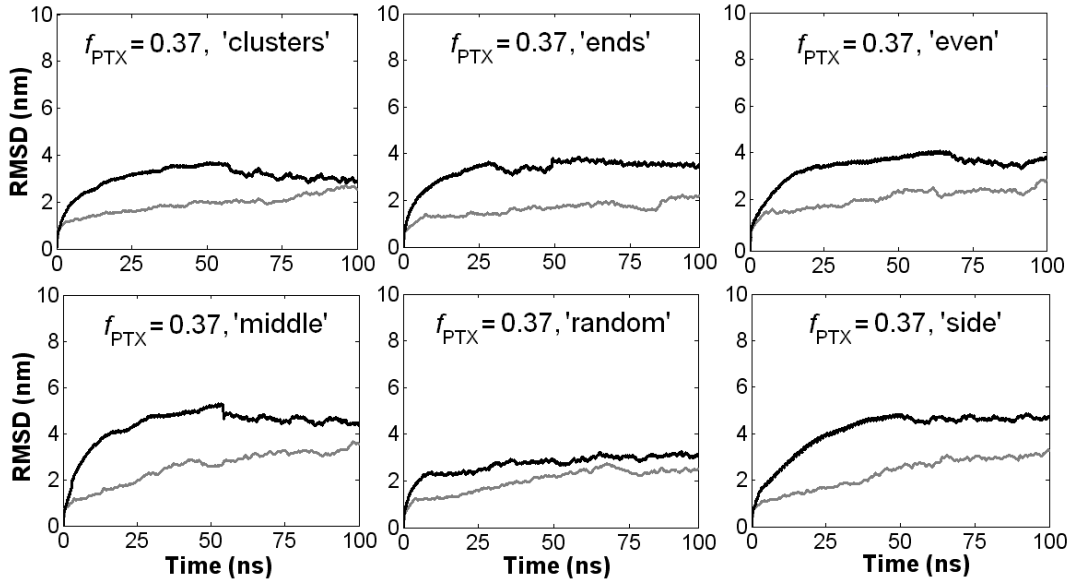

Figure 2.18. RMSD time evolutions for AA *(black line)* and CG *(grey line)* PGG-PTX molecules for f_{PTX} = 0.37. Data were extracted from the 100 ns AA MD and 25 ns CG MD simulations (non-effective timescales).

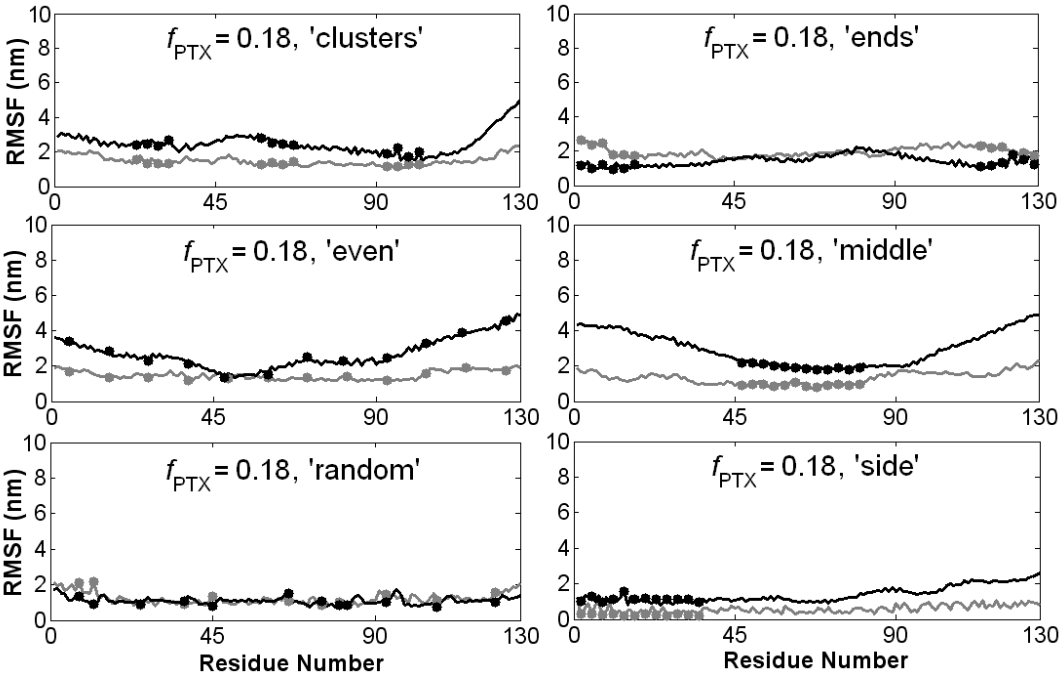

Figure 2.19. RMSF values (by residue) of AA *(black line)* and CG *(grey line)* PGG-PTX molecules for f_{PTX} = 0.18. AA PTX molecules *(black dots)* and CG PTX *(grey dots)* are covalently linked to the PGG backbone in various distributions. All trajectories were extracted from the 100 ns AA MD and 25 ns CG MD simulations (non-effective timescales).

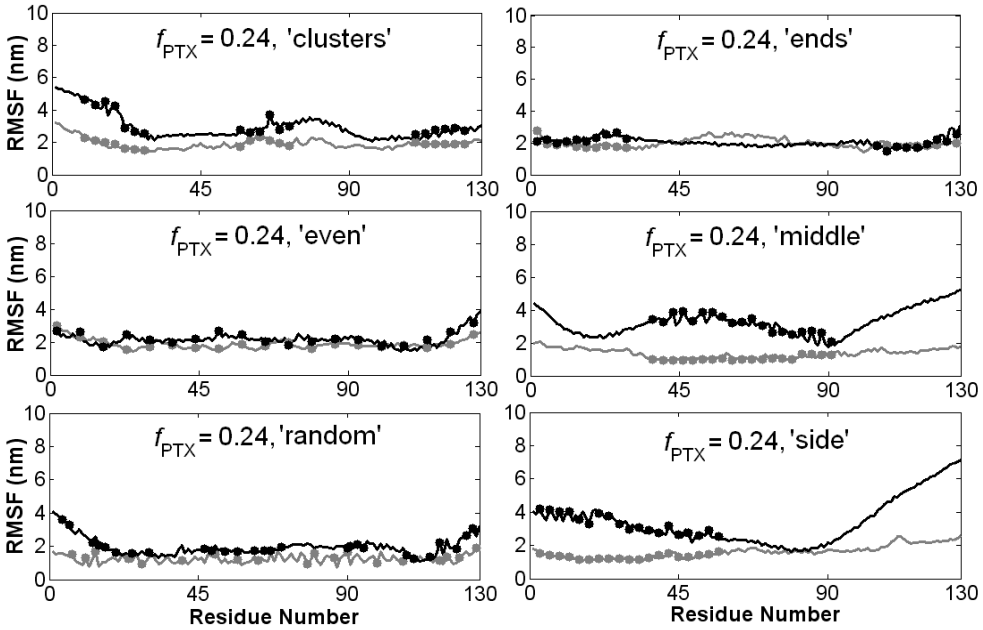

Figure 2.20. RMSF values (by residue) of AA *(black line)* and CG *(grey line)* PGG-PTX molecules for f_{PTX} = 0.24. AA PTX molecules *(black dots)* and CG PTX *(grey dots)* are covalently linked to the PGG backbone in various distributions. All trajectories were extracted from the 100 ns AA MD and 25 ns CG MD simulations (non-effective timescales).

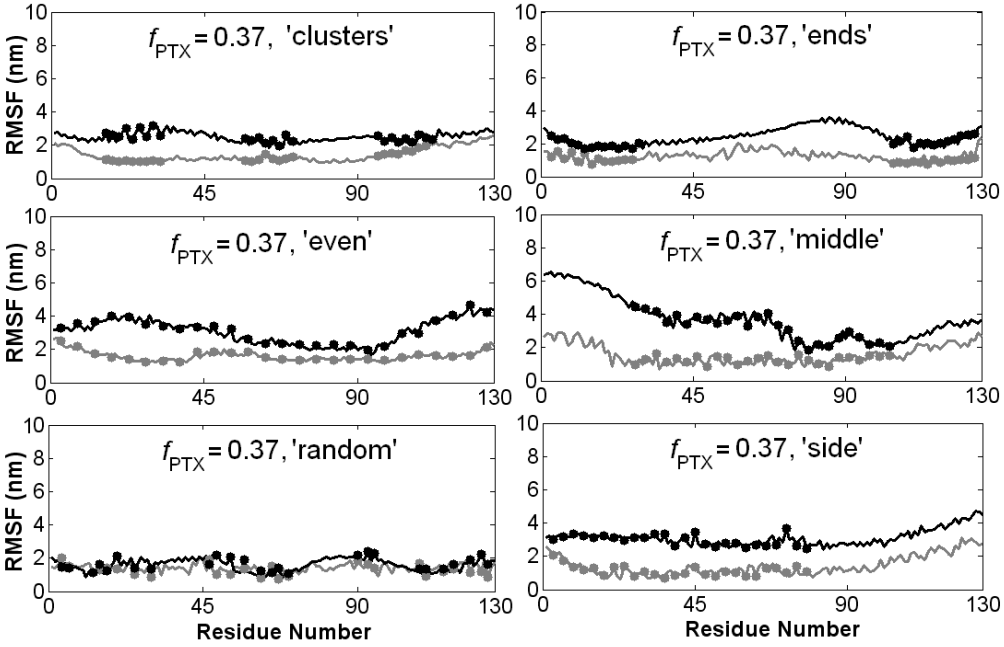

Figure 2.21. RMSF values (by residue) of AA *(black line)* and CG *(grey line)* PGG-PTX molecules for f_{PTX} = 0.37. AA PTX molecules *(black dots)* and CG PTX *(grey dots)* are covalently linked to the PGG backbone in various distributions. All trajectories were extracted from the 100 ns AA MD and 25 ns CG MD simulations (non-effective timescales).

This chapter, in full, is a reprint of the material as it appears in *Biopolymers*, 2010, Peng LX**,** Ivetac A, Van S, Zhao G, Chaudhari AS, Yu L, Howell SB, McCammon JA, Gough DA. The dissertation author was the primary investigator and first author of this paper.

Chapter 3

The molecular conformation of a polymeric cancer therapeutic: a coarse-grained modeling study

Abstract

This study examines the shape, size, and flexibility of poly(γ-glutamyl-glutamate) paclitaxel (PGG-PTX), a series of semiflexible polymer-drug constructs in preclinical development. Eighteen conformations were simulated by varying the PTX loading fraction (f_{PTX} of 0.18, 0.24, and 0.37) and spatial PTX arrangement on the PGG polymer (uniform: 'even' and 'random', clustered: 'clusters' and 'ends', concentrated: 'ends' and 'side'). Coarse-grained (CG) molecular dynamics (MD) simulations of PGG-PTX molecules were run until statistical equilibrium was attained at 4 μs. Root-mean-square deviation (RMSD) clustering was used to determine the representative conformations. Results show that uniform spatial PTX arrangements produce globular PGG-PTX conformations and lower flexibility, and concentrated spatial PTX arrangements result in filamentous shapes and higher flexibility. This study demonstrates the application of coarse-grained modeling towards characterization of semiflexible drug delivery systems that would otherwise be tedious to accomplish by experiments.

3.1 Introduction

Anticancer therapeutics are usually hydrophobic, rigid molecules with poor aqueous solubility. To overcome physiological barriers, physicochemical properties of these drugs are often altered by conjugation with a flexible, hydrophilic agent. Over the past decade, polymers have shown a lot of promise as drug delivery agents. Advantages include increasing blood circulation half-life of drugs, targeting drugs to the tumor while simultaneously minimizing toxicity by limiting drug exposure to normal tissue, and increasing adsorption of drugs in tumor tissue.[49, 50] The polymer-drug hybrid typically includes the biodegradable, flexible, and hydrophilic constituent know to enhance drug delivery to tumors while maintaining the rigid, hydrophobic component associated with the drug's efficacy.

This study focuses on the physiochemical properties of a polymeric-drug construct in preclinical development: poly-γ-glutamyl-glutamate paclitaxel (PGG-PTX). Paclitaxel (Taxol®, $C_{47}H_{51}NO_{14}$) is a cancer therapeutic commonly used to treat breast, ovarian, and lung cancers.[12, 14, 51] While effective, PTX is highly hydrophobic and not sufficiently soluble in water. Therefore, poly-γ-glutamyl-glutamate (PGG), a flexible, hydrophilic, biocompatible polymer, is used to improve the *in vivo* solubility of PTX.[52] To alter the physicochemical properties of the rigid, hydrophobic PTX, PTX is covalently conjugated via an ester linkage to glutamyl-glutamate monomers of a 130-mer PGG backbone (see Fig. 2.1). Currently there are three formulations of PGG-PTX based on the PTX loading fraction (f_{PTX}), defined as:

$$f_{PTX} = \frac{MW_{PTX}}{MW_{PGG-PTX}} \qquad (1)$$

where MW_{PTX} is the molecular weight of all PTX molecules loaded onto a PGG-PTX molecule, and $MW_{PGG\text{-}PTX}$ is the molecular weight of the total PGG-PTX molecule. Each of the three PGG-PTX formulations each molecule is loaded with 12, 19, or 26 PTX molecules, which correspond to PTX loading fractions of f_{PTX} = 0.18, 0.24, or 0.37, respectively.

The preclinical development of anticancer therapeutics usually involves systematic synthesis and trial-and-error experimental testing on *in vitro* and *in vivo* models. While this procedure is effective in the long run, it is time-consuming and resource-intensive.[17] Given the clinical urgency of cancer patients, there is a need for new methods to facilitate this process. In recent years, physicochemical properties of the drug, such as shape, size, and flexibility, have received increasing attention for their role in enhancing the drug's ability to overcome biological barriers that impede the delivery and localization of therapeutics to the target tumor.[53, 54] For instance, a discoidal nanoparticle have been shown to adhere and accumulate better to the walls of tumor endothelia than their spherical counterparts;[49, 55, 56] wormlike, filamentous polymeric micelles have been shown to remain in the blood ten times longer than their spherical counterparts.[57, 58] The size of nanoparticles may affect extravasation into fenestrated tumor endothelia and uptake rate by tumor cells[54, 59] by phagocytosis.[60, 61] Also, higher molecular flexibility may improve the particle's binding ability to cell surfaces, resulting in an increased number of surface interactions of nanoparticles with tissues and biological environment.[62] These new observations suggest the chemical structure of a therapeutic agent as the basis for its clinical development.

Coarse-grained (CG) molecular dynamics (MD) simulations were performed to explore the molecules' size, shape, and flexibility. Eighteen models varying in the PTX loading fraction (f_{PTX} = 0.18, 0.24, and 0.37) and spatial PTX arrangement on the PGG polymer (uniform: 'even' and 'random', clustered: 'clusters' and 'ends', and concentrated: 'middle' and 'side') were studied. (Patterning schemes for the f_{PTX} = 0.18, 0.24, and 0.37 molecules are provided in Fig. 2.2, 2.14, and 2.15, respectively.) CG MD simulations of PGG-PTX were already conducted in Peng et al.[63], but there were shortcomings in the methodology that raised concerns. First, closer inspection shows that portions of the PGG-PTX extends beyond the confines of the original box (5 nm x 13 nm x 20 nm). Since periodic boundary conditions were applied, this behavior resulted in undesired interactions with adjacent PGG-PTX molecules, thereby biasing the resulting conformations. In addition, the previous method regarded the structure at the end of the 800 ns MD trajectory as the representative conformation. While acceptable, this method failed to account for all possible conformations accessed throughout the entire MD trajectory. These shortcomings were addressed in this study. The simulation box size was increased to 20 nm × 20 nm × 20 nm, and root-mean-square deviation (RMSD) clustering was used to analyze and determine the representative conformations of each PGG-PTX molecule. The MD simulation time was also extended to 4 μs (effective time).

3.1.1 Challenges in the modeling methodology

In conventional molecular dynamics (MD) simulations, a starting structure is taken from the Protein Data Bank, a repository of three-dimensional structures of biomolecules as determined from X-ray crystallography and nuclear magnetic resonance

(NMR) spectroscopy.[20, 64, 65] Since there is no structure of PGG-PTX expressed in PDB format, circular dichroism (CD) spectroscopy was used to determine its starting structure. It was also a challenge to determine the final structure of PGG-PTX. Due to the semiflexible nature of PGG-PTX, given the combination of the flexible PGG and rigid PTX components, the molecule is not expected to have a specific conformation. Rather, it is expected that a range of shapes will be observed. Therefore, it would be unnecessary to run MD simulations to an equilibrium at which the molecule is static. To approximate the structure of PGG-PTX, CG MD simulations were run to a statistical equilibrium, a point at which minimal movement exists on the molecular level, and the structure of PGG-PTX was represented by a dynamic ensemble of statistically similar structures.

The goals of this study were three-fold: 1) to develop an insight into possible structural conformations of PGG-PTX, 2) to demonstrate computer simulations as a method to provide insight on the physicochemical properties of anticancer therapeutics that are experimentally tedious, and 3) to improve upon a modeling methodology for a semiflexible polymeric system.

3.2 Computational modeling

3.2.1 Simulation parameters

The governing mathematical equations describing the CG dynamics, mapping of AA models to CG models, and CG parameterization of PGG-PTX molecules were previously described in Peng et al.[63] For each system, a PGG-PTX molecule was solvated in the center of a 20 nm × 20 nm × 20 nm box with explicit water (W) molecules. Because of the negative charges imparted by the glutamyl-glutamate residues

in each system, Na+ ions (234 for f_{PTX} = 0.18, 248 for f_{PTX} = 0.24, and 251 for f_{PTX} = 0.37) were added in place of water molecules in order to neutralize the system. The simulations were carried out under NPT conditions (the number of particles N, pressure P, and temperature T were all fixed). The temperature was kept at 310 K with a coupling constant of τ_T = 0.1 ps. The pressure was weakly coupled to 1 bar with a relaxation time of τ_P = 0.5 ps. The cutoff length for the nonbonded interactions was r_{cut} = 1.2 nm. Lennard-Jones forces were considered for r_{cut} < 0.9 nm and Coulombic forces for r_{cut} < 1.2 nm. The latter was computed every time step for 1.0 nm and once every 10 time steps for 0.9 nm < r_{cut} < 1.2 nm. The time step in the leap-frog integration scheme was 5 fs. The energies, coordinates and velocities were written every 0.5 ps. MD simulations were run until a statistical equilibrium was reached at 1 μs. However, to account for the smoothness of the CG potentials, the diffusional dynamics of CG water, the simulation time was multiplied by a factor of four.[66-68] Therefore, the effective time for each MD simulation was 4 μs.

3.2.2 RMSD clustering

A quantitative method used to analyze protein structures, RMSD clustering accounts for all of the molecular conformations that were accessed during the entire MD trajectory by grouping conformations into clusters based on conformational similarity.[65, 69-71] For each cluster, a conformational average of all structures was then taken, and a structure from the MD trajectory closest to the conformational average was officially regarded as the characteristic conformation that best represented the morphology of the molecule. The RMSD clustering procedure was carried out using the *g_cluster* module

of the GROMACS 4.0.3 package. In *g_cluster*, the RMSD cutoff length was set to a default of 0.125 nm. For each PGG-PTX system, the RMSD cutoff length was manually optimized to meet the following criteria: 1) the total number of clusters is roughly 40, 2) 90% of the trajectory is contained in even fewer clusters, and 3) not many clusters contained just one configuration. Fig. 3.5 shows a sample graph of the RMSD cutoff length vs. number of clusters generated for the f_{PTX} = 0.18 'clusters' molecule, whose RMSD cutoff length of 0.658 nm corresponds to 41 clusters. (The optimized RMSD cutoff distances for all 18 PGG-PTX molecules are provided in Table 3.1.) Each cluster contains a central member, which is regarded as the most representative member of all configurations within a cluster. After the RMSD cutoff length was optimized, each cluster was verified for its significance based on the condition that its corresponding frames must occupy at least 10% of the entire 4 μs trajectory. Once confirmed to be sufficiently significant, each cluster was then evaluated for its uniqueness based on the following condition: if the RMSD between the central members of each significant cluster was greater than twice the RMSD cutoff length, then those clusters were regarded as unique (see Table 3.1). The RMSD Calculator tool in Visual Molecular Dynamics (VMD) 1.8.6 [72] was used to verify the uniqueness among clusters. Finally, a conformation expressed in Protein Data Bank (PDB) format of the characteristic conformation was extracted from each significant, unique cluster.

3.3 Results and Discussion

3.3.1 RMSD values

Fig. 3.1 shows the RMSD time evolutions for the CG MD simulations of PGG-PTX. In all, the RMSD curves rose to ~5-6 nm by 4 μs, with some attaining nearly 8 nm. While somewhat high, these RMSD values were acceptable, given the relatively large sizes of these systems. Nearly all systems attained statistical equilibrium by 4 μs. The 'even', 'random', and 'clusters' systems exhibit flatter plateaus between 2-4 μs than do the 'ends', 'middle', and 'side' counterparts. This behavior suggests that PGG-PTX systems with uniform spatial PTX arrangements are more static than the systems with concentrated PTX arrangements. The higher oscillation in the RMSD values for the 'ends', 'middle', and 'side' systems merely suggests that these molecules exhibit higher molecular fluctuation; the systems are adequately stabilized for this study. In our previous work, in which the CG MD simulations were run for 800 ns, the RMSD values rose to ~3-5 nm. Extending the simulation time four times longer caused the RMSD to increase to 6-8 nm. This behavior indicates that the structure of PGG-PTX continued to change after 800 ns, suggesting that 800 ns may not have been sufficient for PGG-PTX to have approached statistical equilibrium.

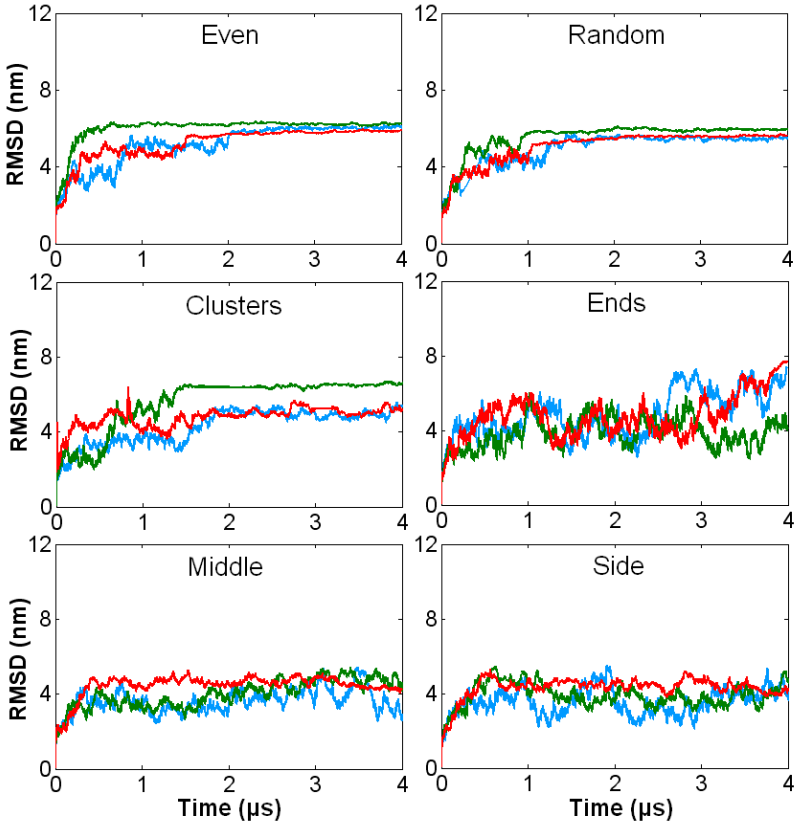

Figure 3.1. RMSD time evolutions for PGG-PTX molecules. Shows the time evolutions that correspond to f_{PTX} = 0.18 *(blue)*, 0.24 *(red)*, and 0.37 *(green)*.

3.3.2 Shape of a PGG-PTX molecule

It is of interest to investigate how the shape of a PGG-PTX molecule can be controlled by rationally varying the amount and location of PTX loaded onto the PGG backbone. Fig. 3.2 shows the representative conformations of all 18 PGG-PTX molecules. The geometry of each molecule is categorized into two types: filament (threadlike, wormlike) and globular (round). In general, the PGG-PTX molecules with uniform spatial PTX distributions tend to result in globular shapes, and molecules with concentrated spatial PTX distributions produced filamentous, wormlike shapes. PGG-PTX molecules with clustered spatial PTX distributions, such as the f_{PTX} = 0.18 'ends'

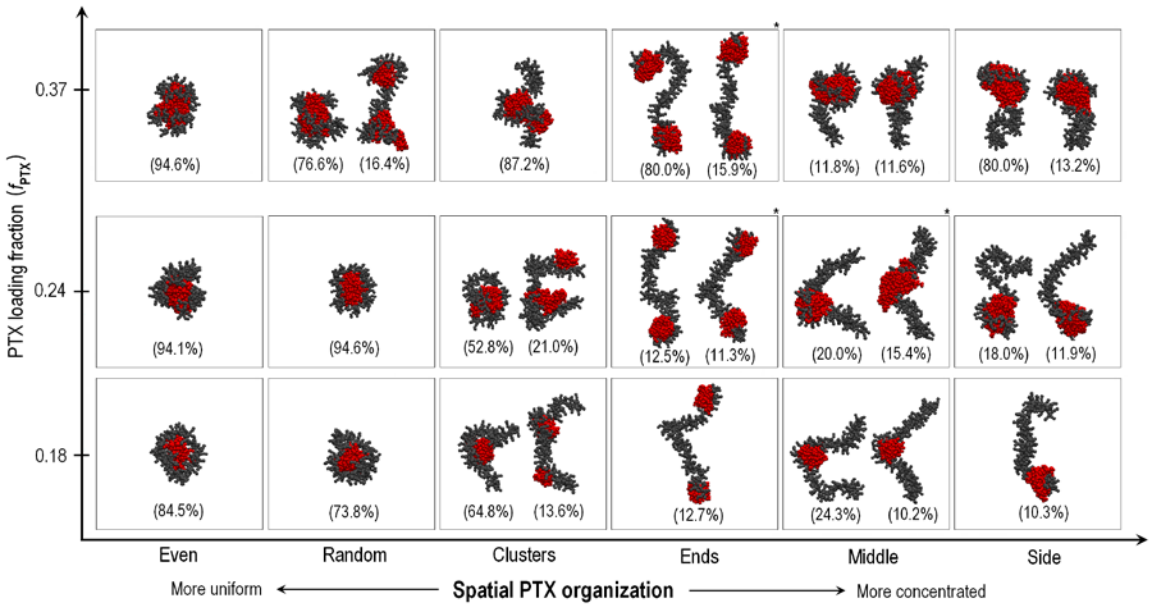

Figure 3.2. Molecular from top clusters for all PGG-PTX molecules determined from RMSD clustering. Each structure shows the glutamyl-glutamate molecules *(black)* and paclitaxel *(grey)* molecules. Explicit water molecules and Na+ ions are not shown. Each configuration is a central member of a cluster. Representing an actual frame in the trajectory, the central member embodies the configuration that is the most similar to the average of all configurations in that cluster. The percentage indicates the population of frames corresponding to that particular cluster for the full 4 μs MD trajectory, or % trajectory occupancy.

and f_{PTX} = 0.24 'clusters' molecules, generated shapes that were in-between globular and filamentous. It is suspected that the hydrophobic driving force among the PTX molecules is responsible for the different shapes. For the 'even', 'random', and 'clusters' molecules, the uniform arrangements of PTX on the PGG backbone brings the entire molecule collectively together (self-assembly) so that the hydrophobic PTX are located in the inner core, where they are furthest away from the solvent. In the 'side' and 'middle' molecules, the spatial PTX entities are localized to a specific section of the PGG backbone, the self-assembly of hydrophobic PTX occurs in only that section, therefore leaving the unconjugated portion of the PGG backbone free to move about, resulting in a filamentous morphology. These results demonstrate that, by exploiting the positioning of

PGG along the PGG backbone, the morphology of each PGG-PTX molecule can be rationally controlled.

The PTX loading fraction does not have a markedly pronounced effect on the morphology. Across all three PTX loading fractions, there is minimal discrepancy among the shapes.

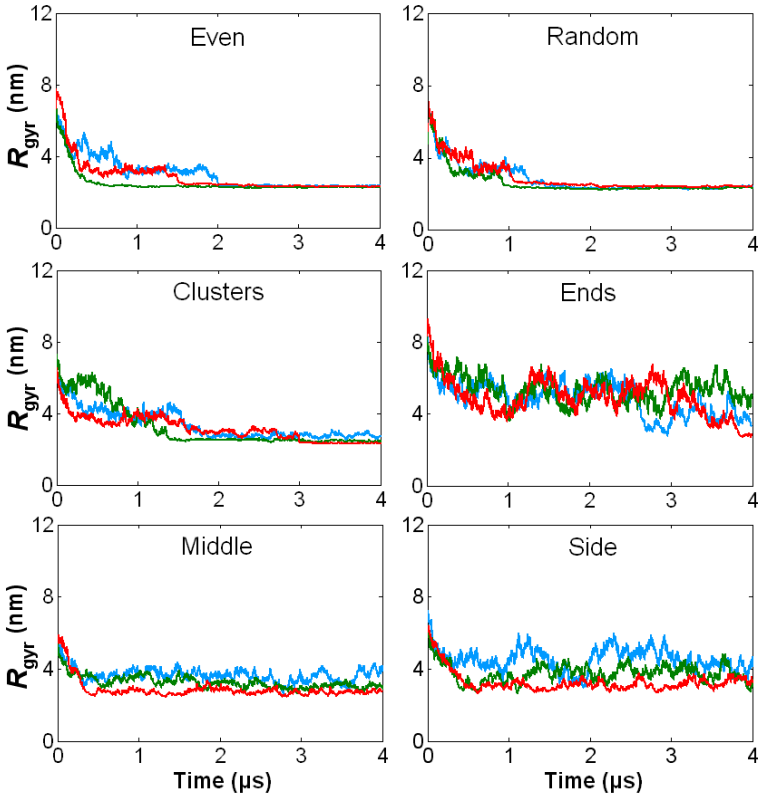

Figure 3.3. Radius of gyration time evolutions of PGG-PTX. Shows the trajectories that correspond to f_{PTX} = 0.18 *(blue)*, 0.24 *(red)*, and 0.37 *(green)*.

3.3.3 Size of a PGG-PTX molecule

The size of each PGG-PTX molecule was assessed based on its radius of gyration (R_{gyr}) over the 4 μs trajectory. Fig. 3.3 shows the radius of gyration time evolutions for all 18 PGG-PTX molecules. The PTX loading fraction does not significantly influence the size of a PGG-PTX molecule. For the 'even', 'random', and 'clusters' systems, the

configurations begin initially from R_{gyr} ~ 6-8 nm, drop to half their original size (R_{gyr} ~ 3 nm) by 2 μs, and maintain that value steadily until 4 μs. For the 'ends', 'middle', and 'side' systems, the configurations also start out at R_{gyr} ~ 6-8 nm, but do not decrease to a steady plateau; rather, their RMSD graphs oscillate around R_{gyr} ~ 4-6 nm. The R_g values for the PGG-PTX molecules with concentrated spatial PTX arrangements are slightly higher than those with uniform PTX arrangements, although the difference is minimal (~1-2 nm). This size difference agrees with the morphology of the PGG-PTX molecules; the globular shapes of the 'even', 'random, and 'clusters' systems is smaller than the filamentous 'ends', 'middle', and 'side' systems.

3.3.4 Flexibility of a PGG-PTX molecule

The flexibility was assessed by the number of representative conformations characterizing each PGG-PTX system and their degree of significance, as indicated by the % trajectory occupancy. For instance, a system characterized by a representative conformation that occupies ~80-90% of the entire MD trajectory is less flexible than a system with multiple representative conformations that each occupies less than 25% of the MD trajectory. As shown in Fig. 3.2, the 'even' and 'random' systems usually characterized by one representative conformation that occupies nearly the entire MD trajectory (80-90%). On the contrary, the 'middle' and 'side' systems exhibit multiple representative conformations that each occupies a smaller portion of the MD trajectory. Therefore, PGG-PTX systems with uniform spatial PTX arrangements are less flexible, while the systems with concentrated PTX arrangements are the more flexible. The PGG-PTX systems with clustered spatial PTX arrangements ('clusters' and 'ends') seem to exhibit an intermediate level of flexibility that is in-between the uniform vs. concentrated

PTX systems. For example, the f_{PTX} = 0.37 'clusters' system is characterized by one representative conformation that occupies nearly 90% of its MD trajectory, while the 'ends' systems at f_{PTX} = 0.24 and f_{PTX} = 0.37 are characterized by 2-4 representative conformations that occupy only 11% of their MD trajectories. Overall, the more concentrated the PTX arrangement on the PGG backbone, the more flexible the PGG-PTX molecule.

It is also worth noting that, while the 'ends' and 'side' systems at f_{PTX} = 0.18 are characterized by one representative conformation, their corresponding % trajectory occupancies are relatively low (10-13%). Each representative conformation corresponded to the only significant *and* unique cluster obtained from the RMSD clustering analysis. There were other unique clusters that occupied the remainder of the 4 μs MD trajectory, but they were only present for less than 10% (data not shown). Since those unique clusters were not considered significant in the RMSD clustering analysis, their representative conformations were not considered in this study. Since the 'ends' and 'side' molecules at f_{PTX} = 0.18 are actually comprised of multiple unique clusters that were not considered significant, these systems sample a wider range of conformations as compared to the other systems. Therefore, the 'ends' and 'side' systems at f_{PTX} = 0.18 are the most flexible PGG-PTX molecules.

Similar to shape, it is most likely that the hydrophobic driving force among PTX is responsible for the flexibility of a PGG-PTX molecule. For the 'ends' and 'random' systems, the uniform distribution of the PTX along the PGG backbone causes the entire molecule to self-assemble into a micelle, where the hydrophobic PTX are located in the core. The strong hydrophobic driving force causes the entire molecule to remain in a

globular shape. For the ‘ends’, ‘middle’, and ‘side’ systems, while the portions of the PGG backbone with PTX conjugation are driven to self-assembly, the longer unconjugated regions of the backbone are free to move about.

Overall, the results show that the spatial PTX arrangement significantly influences the flexibility of a PGG-PTX molecule, but the PTX loading fraction does not have a marked effect on the flexibility.

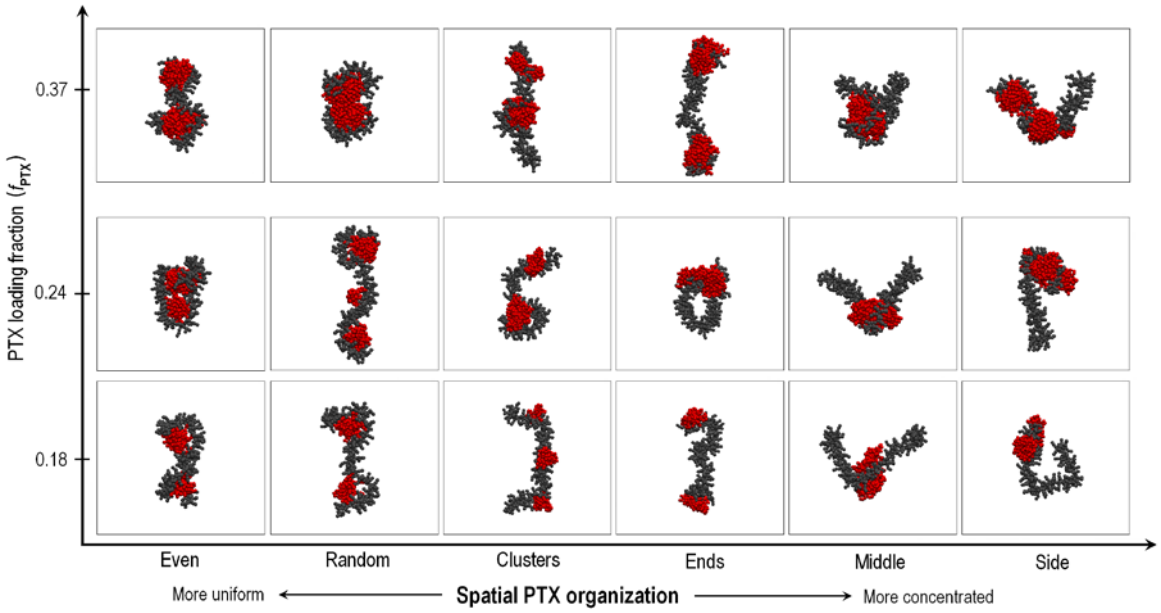

Figure 3.4. Molecular structures of original PGG-PTX molecules. Each structure shows the glutamyl-glutamate molecules *(black)* and paclitaxel *(grey)* molecules. Explicit water molecules and Na+ ions are not shown. Conformations were determined by running CG MD simulations of the molecules until an effective time of 800 ns, and then extracting the PDB at 800 ns. (Adapted from Peng et al.)

3.3.5 Improvements in the modeling approach

A focus of this study was to improve upon the previous method of analyzing the conformation of a PGG-PTX molecule, in which CG MD simulations were run to a statistical equilibrium (until 800 ns), and the PDB extracted from last frame at 800 ns was considered as the accepted structure. Increasing the box size from (5 nm × 13 nm × 20

nm) to (20 nm × 20 nm × 20 nm) and using RMSD clustering for structural analysis resulted in molecular conformations that differed significantly from the representative conformations that were determined from the previous method in Peng et al. (see Fig. 3.4). Most conformations were filamentous, although the f_{PTX} = 0.24 'ends' and f_{PTX} = 0.24 'even' molecules were globules. In other words, the original method suggested that the spatial PTX arrangement did not have a significant effect on the shape of a PGG-PTX molecule. Compared with the analysis in this study, the previous results were not the most accurate. The original box size resulted in overlap among adjacent PGG-PTX molecules, and extracting the conformation at 800 ns did not account for all conformations accessed in the entire MD trajectory. Also, extension of the MD simulation to 4 μs provided a larger population of snapshots for statistical analysis. Overall, this new methodology is a more rigorous, quantitative, and comprehensive methodology to assess the structural conformations of PGG_PTX and provides a more accurate representation of PGG-PTX.

3.3.6 Potential advantages in drug delivery

Geng et al. and Srinivas et al. have argued that filamentous nanoparticles remain in the blood longer than spherical particles in drug delivery. Since the more concentrated spatial PTX arrangements result in filamentous PGG-PTX molecules, the 'ends', 'middle', and 'side' systems are most likely to possess longer circulation half-life. In addition, Decuzzi et al. have argued that discoidal particles show a stronger tendency to adhere and accumulate towards tumor endothelial walls as compared to their spherical counterparts. This discoidal shape is also structurally analogous to the filamentous shape of PGG-PTX molecules, suggesting that filamentous PGG-PTX molecules have a higher

ability to reach the tumor target, as compared to the spherical PGG-PTX molecules, such as f_{PTX} = 0.18 'even', f_{PTX} = 0.24 'ends', and f_{PTX} = 0.37 'random'. In addition, Jiang et al. demonstrated that gold and silver nanoparticles within 2-100 nm in size range varied intracellular signaling processes necessary for basic cell functions. Given that the radius of gyration of the individual PGG-PTX molecules range from 2-8 nm, their size may confer the ability to control intracellular signaling behavior of tumor cells. Finally, S. Takeoka has speculated that greater degrees of flexibility of a nanoparticle could increase the amount of surface interactions of the particle with tumor tissue and binding activity with tumor cells. Therefore, the PGG-PTX systems with the 'ends', 'middle', and 'side' PTX arrangements would result in the greatest amount of interaction with tumor tissue and tumor cells.

3.4 Conclusions

Previous researchers have argued that the ability of a cancer therapeutic to reach tumors may be influenced by the molecular conformation of the therapeutic. To suggest conformations of PGG-PTX that may be useful in biological testing, a library of eighteen different conformations was generated constructing coarse-grained models of PGG-PTX varying in the PTX loading fraction (f_{PTX} = 0.18, 0.24, and 0.37) and spatial patterning of PTX on PGG. RMSD clustering was used to analyze the conformations. We demonstrate the importance of simulation box size, RMSD clustering, and simulation time to accurately determine the structural conformations of PGG-PTX. Results show that PGG-PTX molecules with concentrated spatial PTX distributions are the most promising candidates, given their filamentous morphologies and higher molecular flexibility.

3.5 Supporting Information

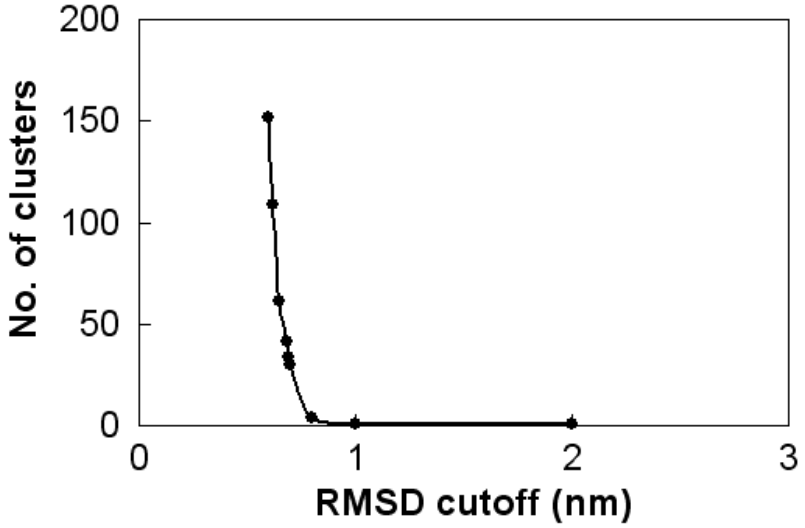

Figure 3.5. Sample relationship between the RMSD cutoff length vs. number of clusters for a PGG-PTX molecule. Shows the data for a f_{PTX} = 0.18 molecule with 'clusters' distribution**.** Trial-and-error using *g_cluster* was used to determine the optimal RMSD cutoff length, which usually corresponds to roughly 40 clusters. For this molecule, the RMSD cutoff length was determined to be 0.68 nm, which corresponds to 41 clusters.

Table 3.1. Summary of RMSD between central members, RMSD cutoff lengths, and number of corresponding clusters for each PGG-PTX molecule

f_{PTX}	Molecule PTX arrangement	Central members		RMSD between central members (nm)	RMSD cutoff (nm)	No. of clusters
0.18	even	--		--	0.67	38
	random	--		--	0.68	36
	clusters	A	B	3.30	0.68	41
	ends	--		--	0.73	41
	middle	A	B	1.85	0.66	37
	side	--		--	0.67	40
0.24	even	--		--	0.63	49
	random	--		--	0.62	37
	clusters	A	B	8.07	0.67	36
	ends	A	B	7.81	0.68	38
	"	A	C	8.91	"	"
	"	B	C	2.17	"	"
	middle	A	B	2.01	0.58	41
	"	A	C	2.08	"	"
	"	B	C	1.52	"	"
	side	A	B	2.12	0.60	38
0.37	even	--		--	0.63	41
	random	A	B	2.12	0.59	40
	clusters	--		--	5.25	41
	ends	A	B	4.47	0.66	41
	"	A	C	14.9	"	"
	"	B	C	13.7	"	"
	middle	A	B	9.41	0.60	38
	side	A	B	4.00	0.54	38

This chapter, in full, has been submitted for publication of the material as it may appear in *Biomacromolecules*, Peng LX, Fajer M, Das SK, Yu L, Howell SB, Gough DA. The dissertation author was the primary investigator and first author of this paper.

Chapter 4

Computer simulations for accelerated selection of candidate compounds of a preclinical polymer-drug conjugate

Abstract

Recent studies suggest that ability of a chemotherapeutic to overcome physiological barriers in dug delivery is associated with its structural and functional properties. Knowledge of these properties is critical in the preclinical development of chemotherapeutics; however, experimental determination of these properties is tedious, resource-intensive, and sometimes inaccessible. Here we used computer simulations to rapidly select the most promising candidates for poly(γ-glutamyl-glutamate) paclitaxel (PGG-PTX) based on their structural and functional properties. We show that variations in the PTX loading fraction (f_{PTX} = 0.18, 0.24, and 0.37) and spatial PTX distributions (uniform, clustered, and concentrated) can influence the morphology, flexibility, surface hydrophilicity, and aggregation of PGG-PTX. Aggregation was validated by freeze-fracture transmission electron microscopy. Our results show that the most promising PGG-PTX conformations are the f_{PTX} = 0.24 systems with concentrated PTX distributions. Overall, we introduce computer simulations as a hypothesis-generating tool for accelerated selection of efficacious compounds in preclinical development.

4.1 Introduction

The preclinical development phase of a drug involves *in vitro* and *in vivo* testing of hundreds of candidate compounds to determine pharmacological characteristics such as bioavailability, toxicity, and efficacy.[73] While effective, this process is time-consuming and resource-intensive. There is a need for more rapid methods of identifying the most efficacious compounds. Here we demonstrate computer simulations as a hypothesis-generating tool for accelerated identification of the most promising candidates of poly-γ-glutamyl-glutamate Paclitaxel (PGG-PTX), an amphiphilic polymer-drug in preclinical development as a cancer therapeutic.[52] Such information can be used to generate hypotheses to design meaningful experiments for efficacy studies.

A primary focus in preclinical drug development is delivering the adequate amount of drug to the target site of action while simultaneously minimizing toxicity to normal tissue.[53, 74] This is a difficult feat that has much room for improvement. Upon administration, the drug must cross various physiological barriers that impede its journey to the target site of action.[53, 54] In passive targeting, they must avoid opsonization by macrophages in order to circulate long enough in the bloodstream, adhere to the walls of tumor endothelium, diffuse through fenestrations of leaky tumor vasculature by the enhanced permeability and retention (EPR) effect, and get taken up by tumor cells.[53, 75, 76] Researchers have shown that a drug's ability to overcome these barriers is significantly influenced by its fundamental structural and functional properties such as morphology,[55, 57, 77, 78] flexibility,[62] surface hydrophilicity,[76] and aggregation[79]. This study focuses on these properties of PGG-PTX candidates and their significance to overcoming barriers in intravenous drug delivery.

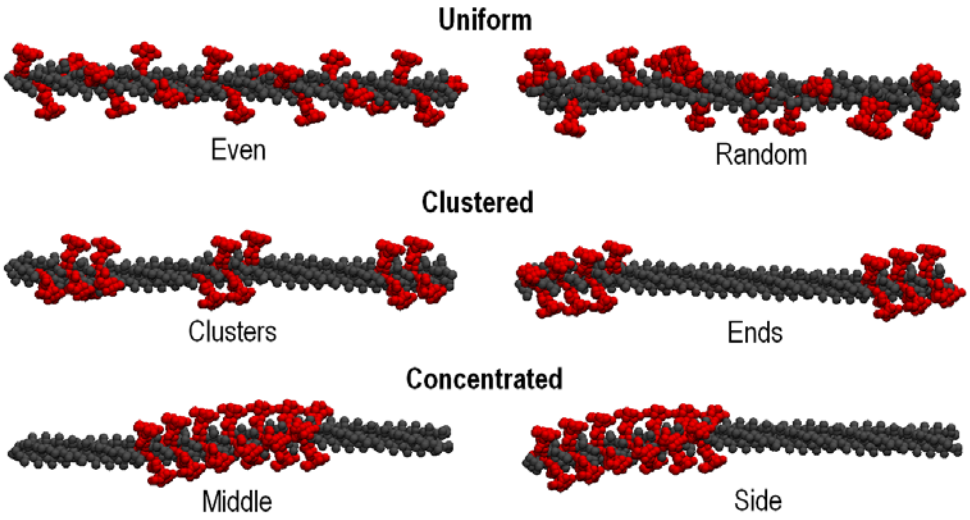

Figure 4.1. Spatial PTX organization patterns for f_{PTX} = 0.24 systems. Shows the 19 PTX molecules (red) loaded on the 130-mer PGG backbone (grey). Spatial patterning of hydrophobic PTX along the PGG polymer includes uniform distributions (a) 'even', b) 'random'), clustered distributions (c) 'clusters', d) 'ends'), and concentrated distributions (e) 'middle', and f) 'side'). All molecules have the same molecular weight but differ in their physical structures. Spatial patterning for the f_{PTX} = 0.18 and 0.37 systems are shown in Figs. 4.5 and 4.6, respectively.

We performed coarse-grained simulations of PGG-PTX systems comprised of multiple molecules. There are three formulations of PGG-PTX varying in the amount of PTX loaded onto a PGG-PTX molecule, or hydrophobic mass fraction: f_{PTX} = 0.18 (12 molecules conjugated onto a 130-mer PGG backbone), 0.24 (19 molecules), and 0.37 (26 molecules). We explored the possible physicochemical properties offered by the candidate compounds, PTX molecules were spatially organized in six different arrangements along the PGG backbone (see Fig. 4.1). Our results show that there are advantages and disadvantages associated with each combination of PTX loading fraction and spatial PTX organization. While the f_{PTX} = 0.37 systems have the maximum amount of PTX per molecule, they also exhibit high aggregation, low flexibility, and relatively low hydrophilic surface hydrophilicity. PGG-PTX systems with more concentrated PTX distributions generate non-spherical, filamentous morphologies, while systems with more

uniform PTX distributions produce spherical shapes. In all, we have identified the most promising PGG-PTX candidates to be the f_{PTX} = 0.24 systems with concentrated spatial PTX distributions, given their nonspherical morphology, flexibility, and relatively high hydrophilic surface hydrophilicity. While a PTX loading fraction of 0.24 is not as high as 0.37, 0.24 is a high enough to produce systems without causing aggregation. This information can now be used to help design meaningful *in vivo* experiments in the preclinical research of PGG-PTX.

4.2 Methods

4.2.1 Coarse-grained modeling

The governing mathematical equations describing the CG dynamics, mapping of AA models to CG models, and CG parameterization of PGG-PTX molecules were previously described in Peng et al.[63] For each system, five identical molecules were solvated in a 20 nm × 20 nm × 20 nm box. Due to the negative charges imparted by the GG and GG-PTX residues in each system, some Na+ ions were added in place of water molecules in order to neutralize the system. The simulations were carried out under NPT conditions (the number of particles N, pressure P, and temperature T were all fixed). For each simulation, the temperature was kept at 310 K with a coupling constant of τ_T = 0.1 ps. The pressure was weakly coupled to 1 bar with a relaxation time of τ_P = 0.5 ps. The cutoff length for the nonbonded interactions is r_{cut} = 1.2 nm. Lennard-Jones forces were considered for r_{cut} < 0.9 nm and Coulombic forces for r_{cut} < 1.2 nm. The latter was computed every time step for 1.0 nm and once every 10 time steps for 0.9 nm < r_{cut} < 1.2

nm. The time step in the leap-frog integration scheme was 5 fs. The energies, coordinates and velocities were written every 0.5 ps. MD simulations were run until a statistical equilibrium was reached at 3 μs. However, to account for the smoothness of the CG potentials, the simulation time was multiplied by a factor of four.[66-68] Therefore, the effective time for each MD simulation was 12 μs.

4.2.2. RMSD clustering

The RMSD clustering procedure was carried out using the *g_cluster* module of the GROMACS 4.0.3 package.[80] For each PGG-PTX system, the RMSD cutoff length was manually optimized to meet the following criteria: 1) the total number of clusters is roughly 40, 2) 90% of the trajectory is contained in even fewer clusters, and 3) not many clusters contained just one configuration. Fig. 4.9 shows a sample graph of the RMSD cutoff length vs. number of clusters generated for the f_{PTX} = 0.18 'clusters' system, whose RMSD cutoff length of 7.6 nm corresponds to 39 clusters. (The optimized RMSD cutoff distances for all 18 PGG-PTX molecules are provided in Table S1.) Each cluster contains a characteristic member, which is regarded as the most representative member of all configurations within a cluster. After the RMSD cutoff length was optimized, each cluster was verified for its significance based on the condition that its corresponding frames must occupy at least 10% of the entire 12 μs trajectory. Once confirmed to be sufficiently significant, each cluster was then evaluated for its uniqueness based on the following condition: if the RMSD between the characteristic members of each significant cluster was greater than twice the RMSD cutoff length, then those clusters were regarded as unique (see Table S1). The RMSD Calculator tool in Visual Molecular Dynamics (VMD) 1.8.6[72] was used to verify the uniqueness among clusters. Finally, a Protein Data

Bank (PDB) structure of characteristic member was extracted from each significant, unique cluster.

4.2.3 Sample preparation of PGG-PTX

Lyophilized samples of PGG-PTX varying in f_{PTX} = 0.18, 0.24, and 0.37 were provided by Nitto Denko Technical Corporation (Oceanside, CA). Lyophilized PGG-PTX varying in f_{PTX} = 0.18, 0.24, and 0.37 were first weighed and diluted to desired concentrations (1 mg/ml for CD spectroscopy and 5 mg/ml for DLS) in 1X HyClone modified DPBS buffer (ThermoScientific, Cat. No. SH30028.03). The samples were then sonicated in a 37ºC water bath for 15 min and vortexed at room temperature for 1 min. The samples were then allowed to settle at room temperature for an additional 10 min. Finally, the samples were then filtered using a 0.2 μm filter paper (Corning, Part No. 431215) and a 20G 1½ Precision Glide needle (Becton Dickinson).

4.2.4 Freeze-fracture transmission electron microscopy

The samples were quenched using sandwich technique and liquid nitrogen-cooled propane. Using this technique a cooling rate of 10000 K/s was reached avoiding ice crystal formation and artifacts possibly caused by the cryofixation process. The cryo-fixed samples were stored in liquid nitrogen for less than 2 hours prior to processing. The fracturing process was carried out in JEOL JED-9000 freeze-etching equipment; the exposed fracture planes were shadowed with Pt for 30 sec at an angle of 25-35º and with carbon for 35 sec (2 kV/60-70 mA, $1x10^{-5}$ Torr). The replicas produced this way were cleaned with concentrated, fuming HNO3 for 24 hours followed by repeated agitation with fresh chloroform/methanol (1:1 by volume) for at least 5 times. Finally, the replicas were examined using a JEOL 100 CX electron microscope.

4.3 Predicting structural and functional properties

Given the sizes of the PGG-PTX systems (M_r of f_{PTX} = 0.18 is ~71 kDa, M_r of f_{PTX} = 0.24 is ~82 kDa, M_r of f_{PTX} = 0.37 is ~90 kDa), it would require an extraordinary amount of computational time and expenses to run molecular dynamics (MD) simulations of atomistic models in explicit solvent to the nanosecond timescale. For the sake of minimizing computational resources as well as accessing longer length-and time-scales, coarse-grained (CG) models of PGG-PTX were constructed by first building atomistic models and then mapping four heavy atoms to one interaction center, as dictated by the MARTINI force field.[66, 68] The equilibrium bonded parameters have been derived from the atomistic MD simulations and were used to parameterize the CG models of PGG-PTX.[63] Each CG PGG-PTX molecule was solvated with four other identical CG molecules in explicit solvent inside a 20nm × 20 nm × 20 nm box.

Traditionally, molecular modeling has been applied to rigid systems, in which MD simulations were run until equilibrium.[20, 64, 81] For a semiflexible system like PGG-PTX, it is not expected that true equilibrium will be ever attained nor is this necessary or practical to run MD simulations until full equilibrium. Therefore, MD simulations on all 18 PGG-PTX systems were run until a statistical equilibrium was reached at 12 μs (or a non-effective time of 3 μs, given the time-scale of CG dynamics is roughly 4 times faster than those of AA dynamics). At this point, only minor fluctuations on the molecular level exist (see Fig. 4.8). Finally, RMSD clustering, a quantitative method that has been used to analyze protein structures,[19, 70, 81] was used to determine the most characteristic conformations of the semiflexible PGG-PTX systems accessed throughout the 12 μs trajectories.

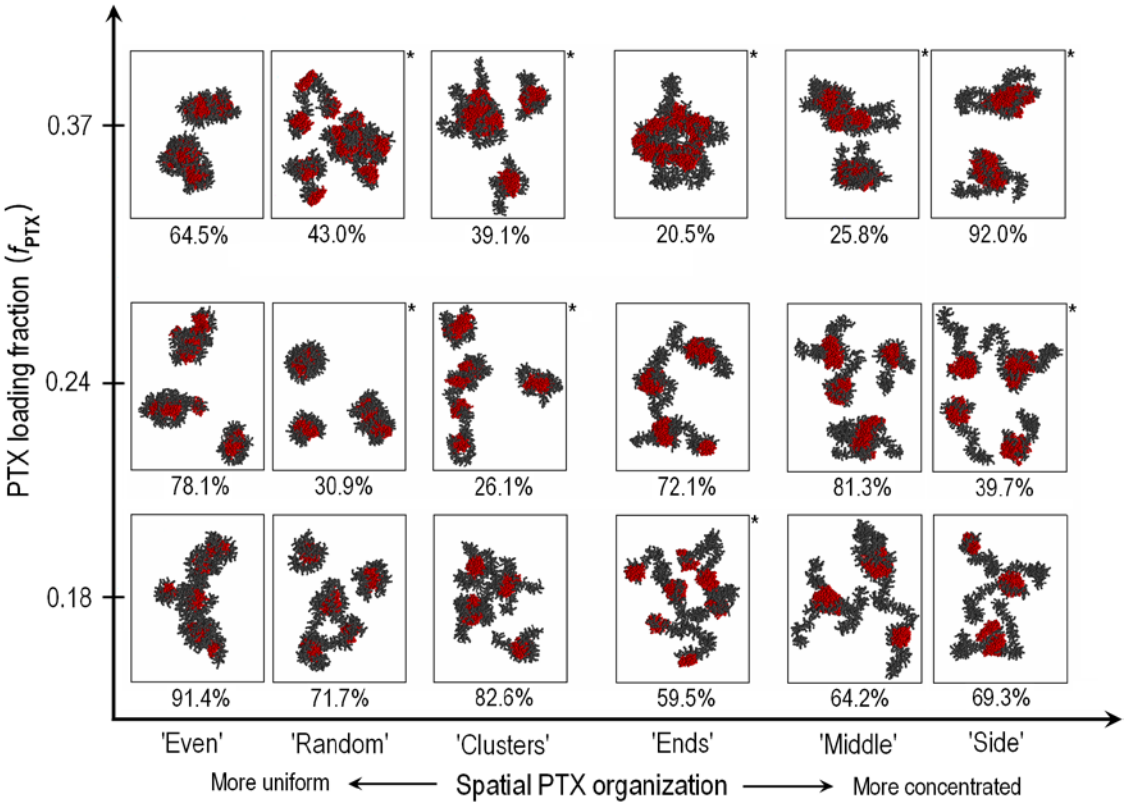

Figure 4.2. Molecular conformations from top clusters for all PGG-PTX molecules determined from RMSD clustering. A system can be comprised of one or more characteristic members. For systems with more than one characteristic member, their predominant characteristic member is denoted with an asterisk ('*'), and their other significant and unique characteristic members is/are shown in Fig. 4.8. A characteristic member corresponds to an actual frame in the 12 μs MD trajectory and is most representative of the average of all configurations in a cluster. The percentage below each box indicates the population of frames corresponding to that particular cluster for the full 12 μs MD trajectory, or % trajectory occupancy.

Fig. 4.2 shows the characteristic morphologies of the 18 PGG-PTX systems. It appears that systems with the highest PTX loading at 0.37 tend to aggregate together into larger, amorphous nanoparticles. On the contrary, at lower PTX loadings, the molecules tend to remain as individual particles and exhibit a lower propensity towards aggregation. These observations suggest that the PTX loading fraction of 0.37 is just high enough for the intermolecular attractive forces to dominate over intramolecular forces. We speculate that the hydrophobic driving force contributed by PTX from different PGG-PTX

molecules is responsible for this intermolecular aggregation. As evidenced by the f_{PTX} = 0.37 systems such as 'even' and 'ends', the PTX molecules are located in the inner core of the larger amorphous particle; this position is the furthest possible distance from the solvent. The hydrophobic effect is also seen in the f_{PTX} = 0.18 and f_{PTX} = 0.24 systems, but only on the intramolecular level. Because the hydrophobic effect dictates that polar species always tend to attract one another, by rationally organizing the PTX molecules on the PGG polymer can be influence its morphology. PGG-PTX systems with more uniform PTX distributions tend to produce spherical, globular shapes, whereas systems with more concentrated PTX distributions generate filamentous, wormlike shapes that are nonspherical. Systems with clustered PTX distributions have both spherical and filamentous shapes, which is expected given the distribution is characterized by concentrated groups of PTX that are uniformly distributed along the PGG polymer.

To investigate the influence of hydrophobic loading fraction and spatial PTX organization on the structural flexibility of PGG-PTX, the root-mean-squared fluctuation (RMSF) per residue was calculated for each system. RMSF is an indication of molecular flexibility. For each system, an average of all RMSF values for all five PGG-PTX molecules was taken and shown in Fig. 4.3. In general, the RMSF values for the f_{PTX} = 0.18 and f_{PTX} = 0.24 systems are similar (around 7-10 nm). Minimal variation in the RMSF values exists throughout residues 1-130 of the molecules in each system, although in the systems with disperse PTX arrangements (such as 'middle 'and side'), regions of the PGG backbone without PTX conjugation exhibit slightly higher RMSF values of 1-2 nm, suggesting slightly higher flexibility. The f_{PTX} = 0.37 systems exhibit the lowest RMSF values, most likely attributed to the systems' tendency towards aggregation. Also,

since the molecules tend to aggregate together into one large nanoparticle, the degree of movement for each molecule should be lower. Since intermolecular forces dominate over intramolecular forces for the f_{PTX} = 0.37 systems, we speculate that the tendency of these systems towards aggregation limits the movement of each individual molecule.

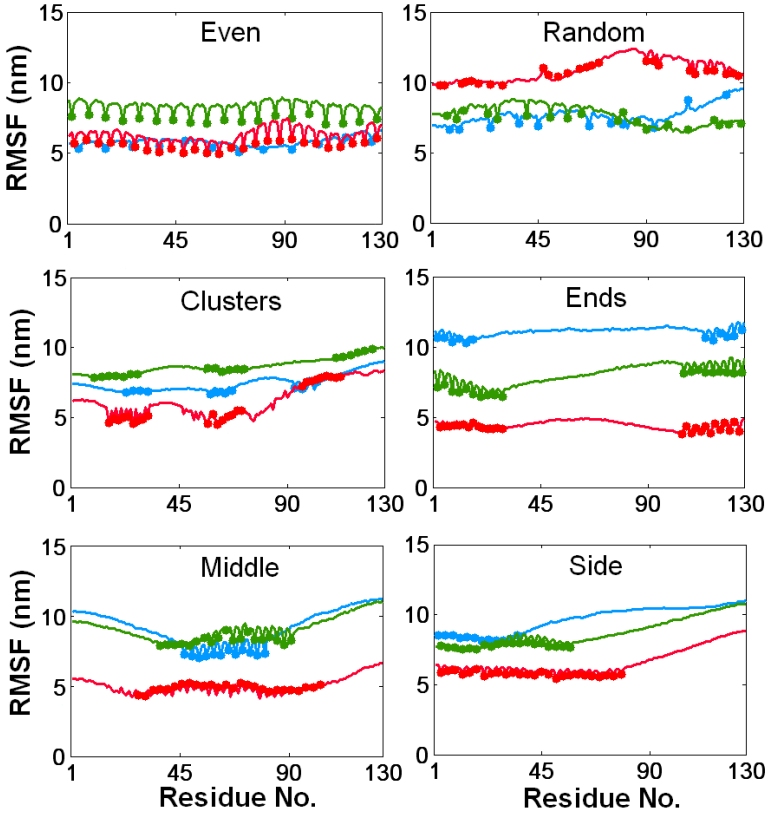

Figure 4.3. Average RMSF per residue for all 18 PGG-PTX systems. Shows the data for f_{PTX} = 0.18 *(blue)*, f_{PTX} = 0.24 *(green)*, and f_{PTX} = 0.37 *(red)* systems. Residues 1 and 130 correspond to the NH3+ and COO- termini, respectively. In general, the f_{PTX} = 0.37 systems have lower RMSF values than the f_{PTX} = 0.18 and 0.24 systems.

To examine the role of hydrophobic loading fraction and spatial PTX organization on the surface hydrophilicity of a system, the percentage of solvent-accessible surface area (SASA) of PGG of the SASA of the all PGG-PTX species, or % PGG SASA, was determined for each system using a statistical determination method (see Scheme S1). The % PGG SASA indicates the percentage of surface area of the hydrophilic PGG (with

respect to the entire PGG-PTX system) that is exposed to the solvent. Table 4.1 shows the % hydrophilicity of all 18 PGG-PTX systems. The f_{PTX} = 0.18 and 0.37 systems have the highest and lowest % PGG SASA, which is expected given increasing PTX loading fractions.

Table 4.1. Percentage (%) PGG SASA of PGG-PTX systems

Spatial PTX distribution	f_{PTX} = 0.18 (%)	f_{PTX} = 0.24 (%)	f_{PTX} = 0.37 (%)
Even	83	82	77
Random	84	78	68
Clusters	84	70	70
Ends	82	78	69
Middle	86	78	73
Side	83	77	75

As the hydrophobic loading fraction is increased, the degree of aggregation also increases. At f_{PTX} = 0.18 and 0.24, PGG-PTX molecules still exist as individual entities, as seen in the f_{PTX} = 0.18 'ends' and 'middle' systems and f_{PTX} = 0.24 'clusters' and 'side' systems. At f_{PTX} = 0.37, however, the five molecules tend to aggregate together as part of a larger amorphous particle; the morphology of each molecules also becomes less distinguishable. We believe that stronger intermolecular forces among the molecules are responsible for this higher degree of aggregation. The radius of gyration (R_{gyr}) indicates the degree of compactness of average packing density of each system (see Fig. 4.4a). Generally speaking, the f_{PTX} = 0.37 systems have lower R_{gyr} than the f_{PTX} = 0.18 and f_{PTX} = 0.24 systems, suggesting that the highest PTX loading fraction results in higher particle aggregation. The R_{gyr} values for the f_{PTX} = 0.18 and f_{PTX} = 0.24 systems are comparable. For each f_{PTX}, there is minimal variation in the R_{gyr} values among the various PTX loading patterns, suggesting that the hydrophobic dispersion patterns on the PGG backbone do not significantly impact the aggregation behavior of PGG-PTX systems.

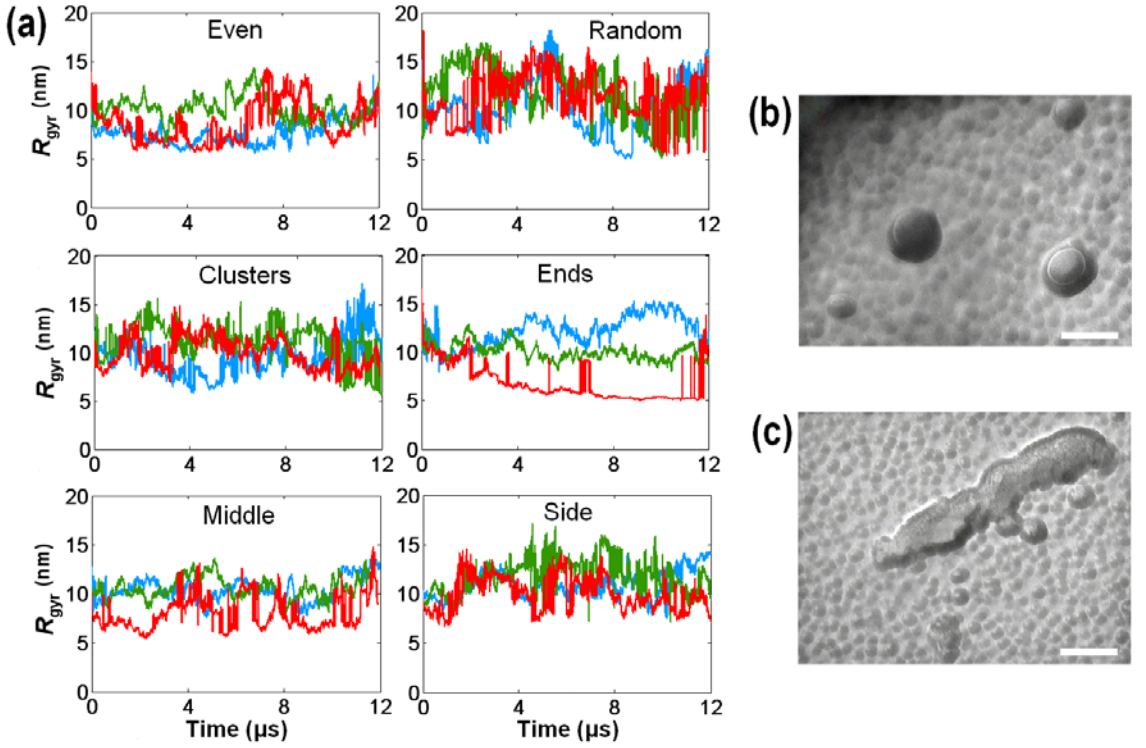

Figure 4.4. Aggregation behavior of PGG-PTX. Shows the a) radius of gyration time evolutions for all 18 PGG-PTX systems for f_{PTX} = 0.18 *(blue)*, f_{PTX} = 0.24 *(green)*, and f_{PTX} = 0.37 *(red)* systems. Lower R_{gyr} values indicate higher degrees of aggregation. Freeze-fracture cryo-TEM of PGG-PTX at f_{PTX} = 0.37 shows aggregation into a) 50-100 nm spherical nanoparticles and b) long, rod-shaped particles that are 600 nm in length and 100 nm in width. The population of particles of particles is not very monodisperse. (Scale bar: 100 nm)

4.4 Significance of structural and functional properties

It has been reported in literature that the morphology, flexibility, surface hydrophilicity, and aggregation of a nanoparticle therapeutic can influence its ability to overcome physiological barriers preventing access to tumor cells. Our results show that these properties of PGG-PTX aggregates can be controlled by systematically varying the PTX loading fraction and PTX dispersion patterns along the PGG polymer of each PGG-PTX molecule.

The morphology of a nanoparticle has been shown to impact its adhesion strength to the walls of tumor endothelia and blood circulation half-life. Decuzzi et al. reported that nonspherical, oblate particles with less curvature demonstrate stronger adhesion to walls of tumor endothelia as compared to their spherical counterparts (which has more curvature).[77] Also, Dennis Discher and colleagues have demonstrated that wormlike, filamentous particles circulate longer in the bloodstream than spherical particles, greatly increasing the chances of the nanoparticles to reach the tumor tissue and avoid clearance by the reticoendothelial system (RES).[57, 78] These arguments suggest that a nonspherical, filamentous morphology is an efficacious structural property that enhances the delivery of a particle in passive targeting. Because these nonspherical, filamentous shapes are found in PGG-PTX systems with PTX loading fractions of 0.18 and 0.24, these systems are the most likely to exhibit stronger adhesion properties and longer circulation half-lives.

There has also been speculation that greater degrees of flexibility in particles may improve the binding ability to the cell surface, resulting in an increased number of surface interactions of particles with tissues and biological environment.[62] Our RMSF results show that at f_{PTX} = 0.18 and 0.24, PGG-PTX systems with more concentrated PTX dispersion arrangements exhibit higher flexibility throughout the entire molecule as compared to the f_{PTX} = 0.37 systems. This trend agrees with the aggregation behavior of the PGG-PTX systems. Generally speaking, the systems with higher aggregation are characterized by stronger attractive intermolecular forces as a result of the hydrophobic effect among PTX molecules, thus limiting the movement of the individual molecules. Uniform PTX arrangement along the PGG backbone also causes PGG-PTX to be less

flexible than the concentrated PTX arrangements. Therefore, PGG-PTX systems with lower PTX loading fractions and concentrated spatial PTX distributions are most likely to bind effectively to cell surfaces.

Aside from morphology and flexibility, the degree of surface hydrophilicity of a particle can also enhance its blood circulation half-life,[75, 76] subsequently improving its opportunities to reach the target tumor tissue and cells via the EPR effect. Studies have shown that the more hydrophilic the surface hydrophilicity of a particle, the more likely will it be able to avoid opsonization and RES clearance and thus remain in the bloodstream for a longer time, similar to the effects of nonspherical particle morphology. This action allows the particles more time to reach the intended tumor target. (Particle uptake by macrophages is an immune response by the body and foreign particles tend to get taken up by macrophages and disposed of by the liver and spleen.) Since the lower PTX loading fractions result in systems with higher surface hydrophilicity, as shown in Table 4.1, we infer that these systems are the most likely to possess longer circulation half-lives and thus are more likely to reach tumors.

It has also been shown that the degree of aggregation is related to its *in vivo* stability.[79] Particle aggregation of the particle is usually not desired due to the lack of stability associated with aggregation. The goal is to achieve a monodisperse, uniform distribution of particles of similar sizes. It is apparent that the f_{PTX} = 0.37 systems exhibit the highest degree of aggregation, and the f_{PTX} = 0.18 and 0.24 systems exhibit lower degrees of aggregation (with exception to the f_{PTX} = 0.18 'even' system). These observations suggest that the PGG-PTX will be stable *in vivo* at f_{PTX} = 0.18 and 0.24 but not at f_{PTX} = 0.37.

The aggregation behavior of PGG-PTX (f_{PTX} = 0.37) was validated using freeze-fracture transmission electron microscopy. For the sample, it is hypothesized that the hydrophobic dispersion arrangement on the PGG backbone is most similar to that of the 'random' configuration. Figs. 4.4b and 4.4c show that the PGG-PTX (f_{PTX} = 0.37) sample exists as a wide range of spherical sizes, from 10 nm to 100 nm in diameter.

4.5 Conclusions

In summary, based on previous literature, we have determined that the most ideal candidate compound(s) of PGG-PTX to possess the following characteristics: high PTX loading fraction, relatively long circulation half-life, ability to adhere firmly adhere to walls of tumor endothelia, ability to bind effectively to tumor cell surfaces, and high *in vivo* stability. Researchers have recently shown that these characteristics are associated with physicochemical properties, such as morphology, flexibility, and hydrophilic surface hydrophilicity, as well as aggregation behavior of a drug. While the f_{PTX} = 0.37 systems have the highest PTX loading fraction, they also result in high aggregation and are not very flexible, which could result in lower *in vivo* stability and complications in binding to tumor cells. Likewise, the f_{PTX} = 0.18 systems offer the advantages of high flexibility and high hydrophilic surface hydrophilicity, their PTX loading fraction is minimal. Therefore, our results show that the most promising conformational candidates of PGG-PTX are the f_{PTX} = 0.24 systems with concentrated spatial PTX distributions, based on their relatively high PTX loading fraction, nonspherical morphologies, relatively high molecular flexibility, and low aggregation. Overall, we have shown the applications of

computer simulations towards rapid selection of the most promising candidate compounds based on physicochemical properties. Because such information can not be easily determined by experiments, computer simulations can now be applied as a tool to aid in the drug development of preclinical drugs.

4.6 Supporting Information

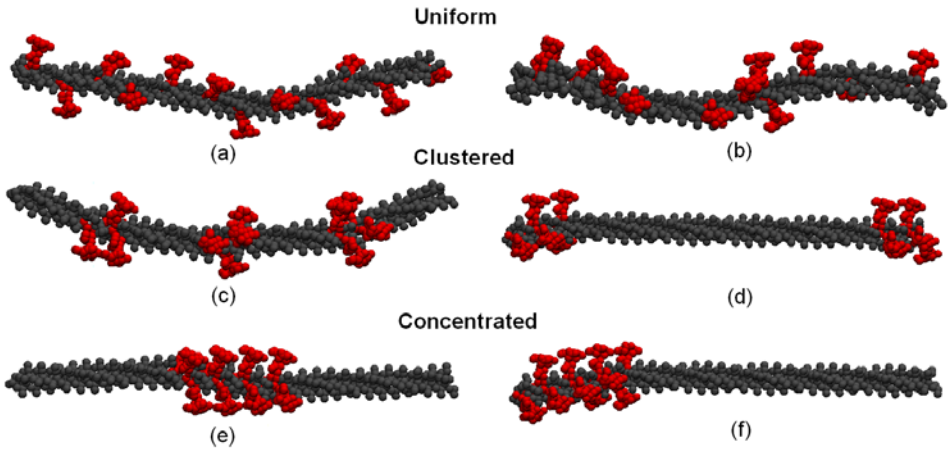

Figure 4.5. Spatial PTX organization patterns for f_{PTX} = 0.18 systems. Shows the 12 PTX molecules (red) loaded on the 130-mer PGG backbone (grey). Spatial patterning of hydrophobic PTX along the PGG polymer includes uniform distributions (a) 'even', b) 'random'), clustered distributions (c) 'clusters', d) 'ends'), and concentrated distributions (e) 'middle', and f) 'side'). All molecules have the same molecular weight but differ in their physical structures.

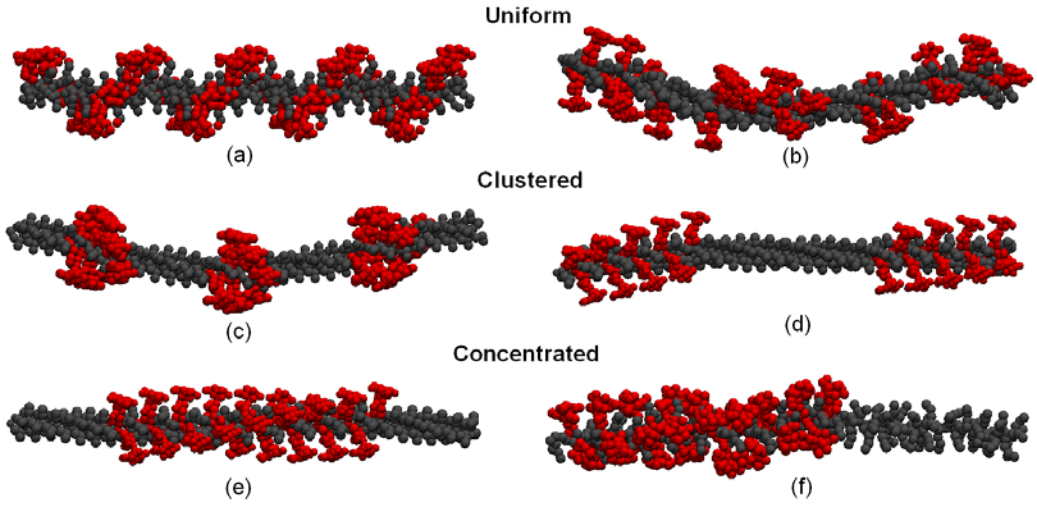

Figure 4.6. Spatial PTX organization patterns for f_{PTX} = 0.37 systems. Shows the 26 PTX molecules (red) loaded on the 130-mer PGG backbone (grey). Spatial patterning of hydrophobic PTX along the PGG polymer includes uniform distributions (a) 'even', b) 'random'), clustered distributions (c) 'clusters', d) 'ends'), and concentrated distributions (e) 'middle', and f) 'side'). All molecules have the same molecular weight but differ in their physical structures.

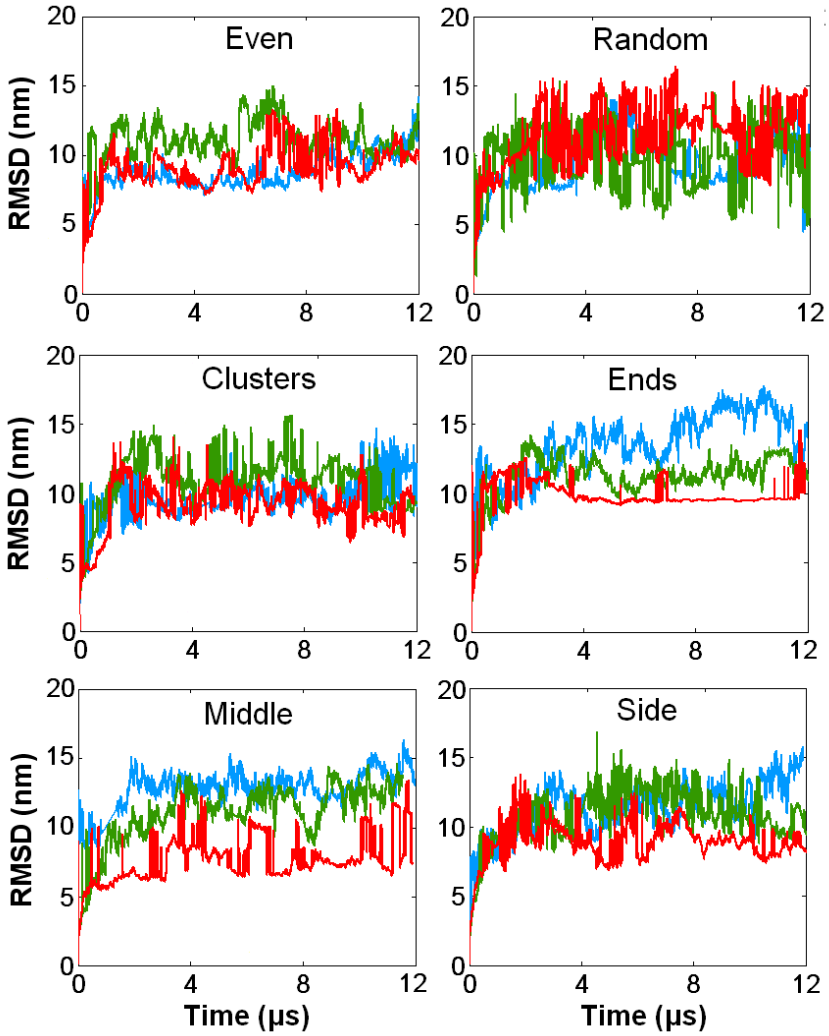

Figure 4.7. RMSD values of 18 PGG-PTX systems. Shows the data for f_{PTX} = 0.18 (blue), f_{PTX} = 0.24 (green), and f_{PTX} = 0.37 (red) systems. Root-mean-square deviation (RMSD) indicates the overall movement of a system. By 12 μs, all systems have attained a statistical equilibrium.

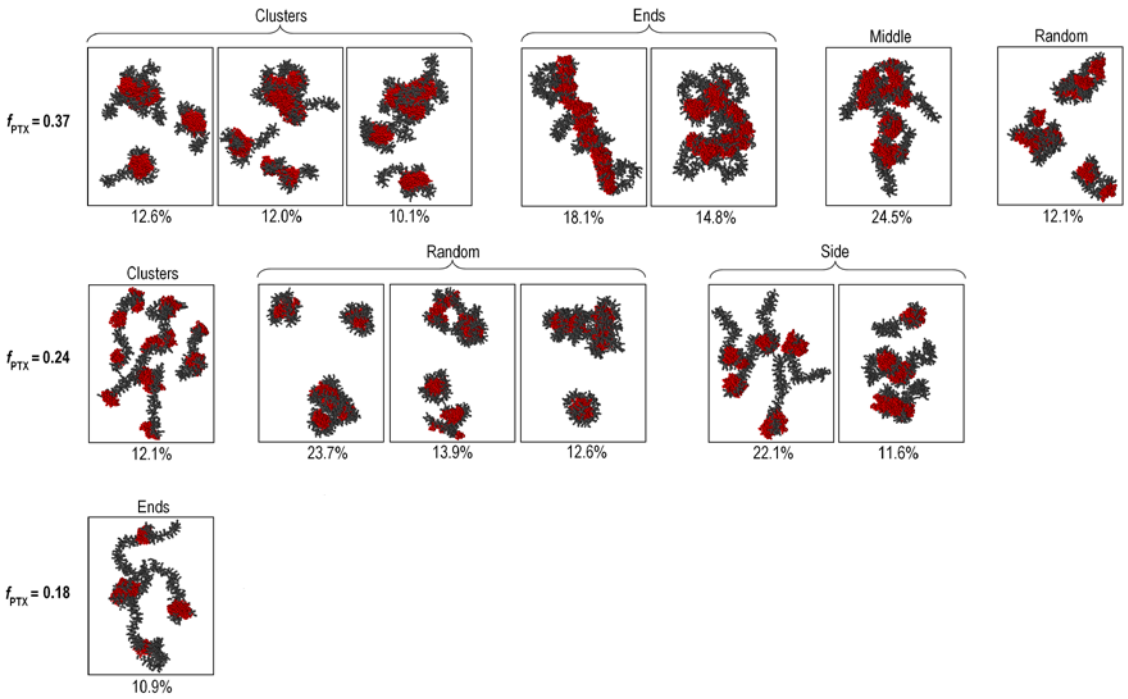

Figure 4.8. Remaining characteristic members for PGG-PTX systems with more than one characteristic member.

Table 4.2. Summary of RMSD between characteristic members, RMSD cutoff lengths, and number of corresponding clusters for each PGG-PTX molecule

f_{PTX}	Molecule PTX arrangement	Characte-ristic members	RMSD between characteristic members (nm)	RMSD cutoff (nm)	No. of clusters
0.18	even	--	--	5.75	39
	random	--	--	5.6	40
	clusters	--	--	7.16	39
	ends	A B	16.0	9.25	38
	middle	--	--	7.55	37
	side	--	--	8.0	41
0.24	even	--	--	6.7	37
	random	A B	23.3	6.4	41
	"	B C	14.6		
	"	A C	16.3		
	"	A D	23.3		
	"	B D	17.1		
	"	C D	10.3		
	clusters	A B	18.3	5.5	39
	ends	--	--	6.7	38
	middle	--	--	7.1	37
	side	A B	18.1	12.0	35
	"	B C	19.9		
	"	A C	18.7		
0.37	even	-- --	--	3.1	39
	random	A B	9.35	6.0	39
	clusters	A B	7.5	3.5	38
	"	B C	9.6		
	"	A C	13.7		
	"	A D	14.7		
	"	B D	11.5		
	"	C D	14.7		
	ends	A B	8.3	4.6	39
	"	B C	8.6		
	"	A C	5.1		
	middle	A B	4.78	2.0	37
	side	--	--	7.25	36

Scheme 4.1. Statistical determination of the surface hydrophilicity of PGG-PTX

The degree of surface hydrophilicity of a PGG-PTX system was characterized by the % PGG SASA, or the surface area of hydrophilic PGG (with respect to the entire PGG-PTX system) exposed to the solvent.

I. PGG-PTX systems with more than one characteristic member

Because some PGG-PTX systems are characterized by multiple unique, significant characteristic members, the % PGG SASA for each characteristic member was taken into account collectively (by factoring in the % trajectory occupancy for each characteristic member) as the adjusted % PGG SASA.

$$\text{Adjusted \% PGG SASA} = \sum_i \left[(\%\ PGG\ SASA)_i \cdot \frac{(\%\, Trajectory\ occupancy)_i}{Total\ \%\ trajectory\ occupancy} \right]$$

where *i* denotes the characteristic member(s) of a system. A sample calculation (for the ***f*$_{PTX}$ = 0.24 'random' system**) is provided below:

Data for the *f*$_{PTX}$ = 0.24 'random' system		
Characteristic member	% PGG SASA	% Trajectory occupancy
A	78.1	30.9
B	78.0	23.7
C	81.6	13.9
D	75.5	12.6
		Total: 81.2

Adjusted % PGG SASA =

$$78.1\left(\frac{30.9}{81.2}\right) + 78.0\left(\frac{23.7}{81.2}\right) + 81.6\left(\frac{13.9}{81.2}\right) + 75.5\left(\frac{12.6}{81.2}\right) = 78.2$$

II. PGG-PTX systems with only one characteristic member

For the PGG-PTX systems characterized by only one unique and significant characteristic member, the (original) % PGG SASA is the adjusted % PGG SASA.

The PGG SASA data for all PGG-PTX systems are shown in Table S2.

Table 4.3 Solvent accessible surface area of PGG-PTX and PGG components

System							
f_{PTX}	PTX arrange-ment	Charac-teristic member	Total SASA of system (nm^2)	SASA of PGG (nm^2)	% PGG SASA	Adjusted % PGG SASA	% Trajectory occupancy
0.18	even	--	1612.7	1342.3	83.2	83.2	91.4
	random	--	1621.5	1359.4	83.8	83.8	71.7
	clusters	--	1610.3	1360.6	84.5	84.5	82.6
	ends	A	1742.3	1392.9	79.9	80.2	59.5
	"	B	1781.5	1456.0	81.7		10.9
	middle	--	1661.8	1429.7	86.1	86.1	64.2
	side	--	1704.6	1416.2	83.1	83.1	69.3
0.24	even	--	1518.9	1243.0	81.8	81.8	78.1
	random	A	1604.4	1252.6	78.1	78.2	30.9
	"	B	1615.2	1260.4	78.0		23.7
	"	C	1557.1	1271.1	81.6		13.9
	"	D	1673.5	1264.1	75.5		12.6
	clusters	A	1714.5	1292.7	75.4	71.8	26.1
	"	B	1825.5	1279.0	70.1		12.1
	ends	--	1672.3	1311.8	78.4	78.4	72.1
	middle	--	1676.6	1303.6	77.8	77.8	81.3
	side	A	1697.5	1302.8	76.7	75.5	39.7
	"	B	1775.9	1282.4	72.2		22.1
	"	C	1662.2	1291.7	77.7		11.6
0.37	even	--	1598.2	1228.0	75.8	76.8	64.5
	random	A	1840.1	1258.7	68.4	68.4	43.0
	"	B	1828.2	1248.2	68.3		12.1
	clusters	A	1656.0	1236.8	74.7	72.6	39.1
	"	B	1676.6	1259.1	75.1		12.6
	"	C	1796.9	1265.1	70.4		12.0
	"	D	1642.6	1259.1	75.6		10.1
	ends	A	1775.3	1315.2	74.1	71.6	20.5
	"	B	1990.5	1369.0	68.8		18.1
	"	C	1834.5	1334.1	72.7		14.9
	middle	A	1583.5	1205.8	76.1	74.6	25.8
	"	B	1685.1	1231.1	73.1		24.5
	side	--	1580.7	1188.1	75.2	75.2	92.0

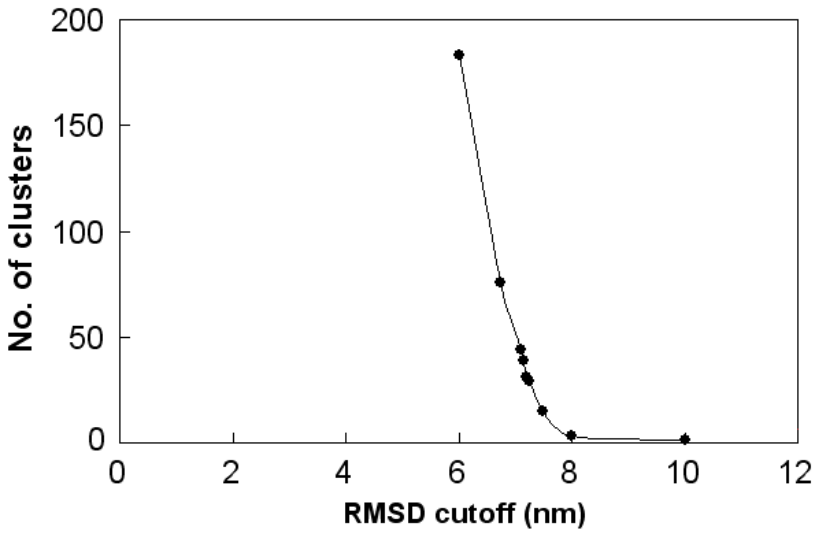

Figure 4.9. Sample relationship between the RMSD cutoff length vs. number of clusters for a PGG-PTX system. Shows the data for the f_{PTX} = 0.18 system with 'clusters' distribution**.** Trial-and-error using *g_cluster* was used to determine the optimal RMSD cutoff length, which usually corresponds to roughly 40 clusters. For this molecule, the RMSD cutoff length was determined to be 7.16 nm, which corresponds to 39 clusters.

This chapter, in part, is currently being prepared for submission for publication of the material. Peng LX, Yu L, Howell SB, Gough DA. The dissertation author was the primary investigator and first author of this paper.

Chapter 5

Effect of nonpeptide RGD ligand density and PEG molecular weight on the conformation of poly(γ-glutamyl-glutamate) paclitaxel conjugates: a coarse-grained modeling study

Abstract

The shape, flexibility, and surface hydrophilicity have received increasing attention for influencing the ability of nanoparticles to cross biological barriers in drug delivery. In this study, molecular dynamics (MD) simulations were used to study these properties of nonpeptide RGD-targeted poly(γ-glutamyl-glutamate)-paclitaxelpoly(ethylene glycol) (PGG-PTX-PEG-npRGD), a series of actively targeted polymer-drug constructs in preclinical development. It was hypothesized that the PEG molecular weight (500 Da, 1000 Da, and 2000 Da) and nonpeptide RGD ligand density (4, 8, 12, and 16 per molecule) concomitantly affects the shape, flexibility, and surface hydrophilicity of PGG-PTX-PEG-npRGD. Circular dichroism spectroscopy was used to suggest initial structures for the all-atom (AA) models of PGG-PTX-PEG-npRGD, which were further converted to coarse-grained (CG) models using the MARrink's Toolkit INItiative (MARTINI) mapping scheme. CG MD simulations were run until statistical equilibrium was attained at 4 μs. Most PGG-PTX-PEG-npRGD are globular, although

filamentous and globular shapes were observed in the PEG500 and PEG1000 molecules. The PEG500 and PEG1000 molecules are more flexible than the PEG2000 systems. Higher presence of nonpeptide RGD ligands tend to decrease the surface hydrophilicity of PGG-PTX-PEG-npRGD. These results indicate that the PGG-PTX-PEG1000-$npRGD_4$ and PGG-PTX-PEG1000-$npRGD_8$ molecules are the most efficacious candidates and are further recommended for experimental preclinical studies.

5.1 Introduction

A continuing challenge in the development of anticancer therapeutics is ensuring that adequate amounts of the drug is delivered to tumors while simultaneously minimizing toxic and adverse effects to healthy tissue.[1,82] An emerging approach in cancer treatment is targeting biological and physiological pathways that support tumor development while minimizing toxicity and adverse effects to normal tissue. Angiogenesis is crucial for tumor growth. Therefore, the microvascular endothelial cell and its receptors have become key targets in cancer therapy.[83] In particular, the $\alpha_V\beta_3$ integrin and its ligands, vitronectin and fibronectin, are known to promote angiogenesis [84, 85]. It has also been shown that tumor cells with non-activated $\alpha_V\beta_3$ integrins exhibit decreased angiogenic behavior.[86] As a result, antagonists of $\alpha_V\beta_3$ integrins have emerged as a new class of anticancer therapeutics, primarily the Arg-Gly-Asp (RGD) tripeptide and RGD peptidomimetics, which bind to $\alpha_V\beta_3$ integrins with high affinity to prevent binding of $\alpha_V\beta_3$ integrins to its natural receptors.[87-89]

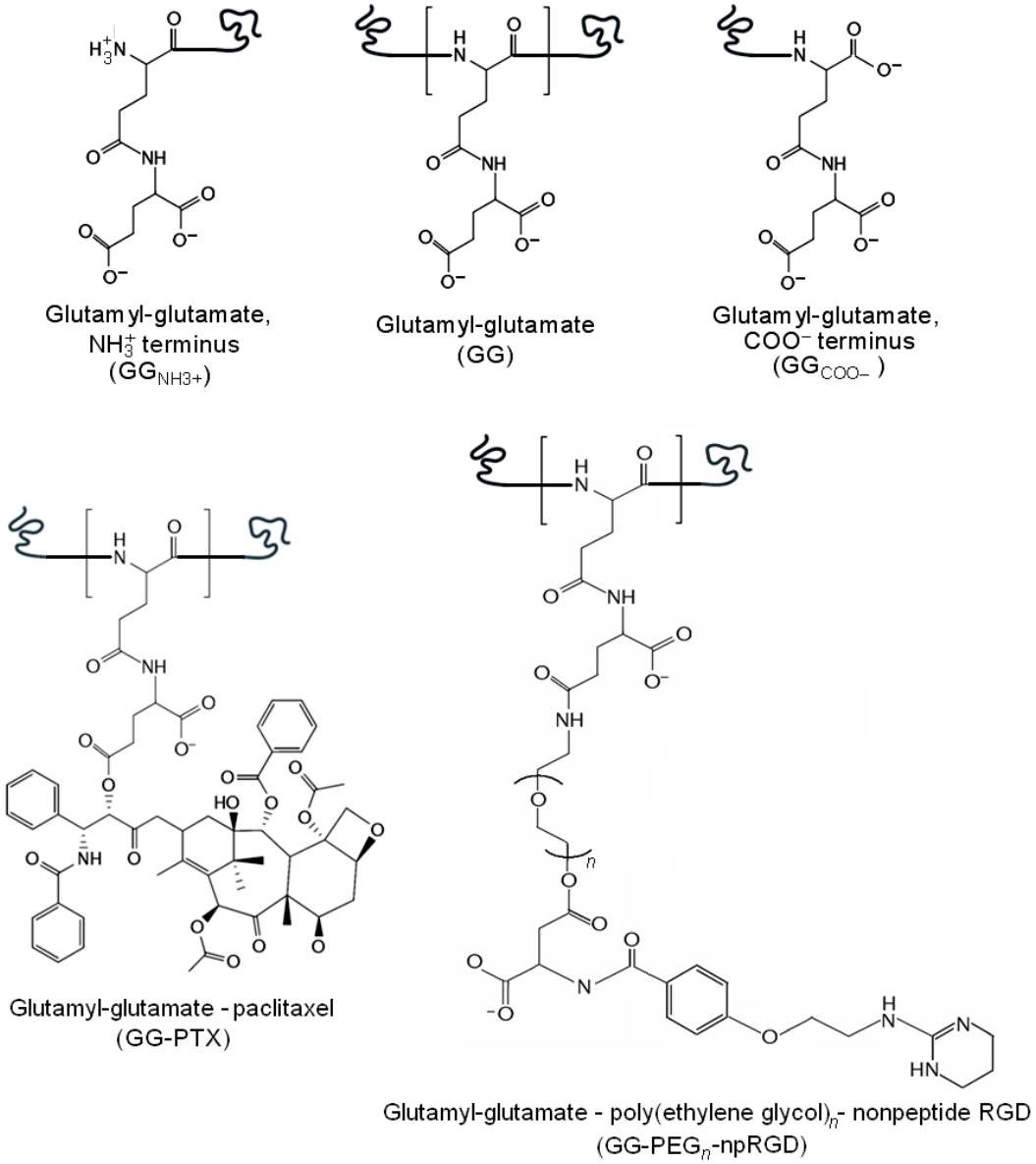

Figure 5.1. Chemical structures of GG, GG-PTX, and GG-PEG-npRGD residues. GG_{NH3+} and GG-PTX each has a charge of -1; GG and GG-PEG-npRGD each a charge of -2; and GG_{COO-} a charge of -3. The GG residue differs slightly based on its position on the polymer, such as its position at the amino or carboxyl termini. For the GG-PTX residue, paclitaxel is covalently conjugated to a carboxylate group of glutamyl-glutamate via an ester linkage. For the GG-npRGD residue, the nonpeptide RGD is covalently attached to a linear PEG spacer, which is conjugated to the GG residue. The length *n* of the PEG spacer depends on the molecular weight of the linear PEG molecule: 500 Da, 1000 Da, and 2000 Da correspond to approximately 11, 23, and 45 ethylene glycol monomers.

This study focuses on the preclinical development of a nonpeptide RGD-based drug delivery system: poly(γ-glutamyl-glutamate) paclitaxel tethered to nonpeptide RGD via poly(ethylene glycol) (PGG-PTX-PEG-npRGD).[15] Paclitaxel (Taxol®, $C_{47}H_{51}NO_{14}$) is a hydrophobic drug used to treat breast, ovarian, and lung cancers, and poly(γ-glutamyl-glutamate) (PGG) is a hydrophilic polymer conjugated to PTX to improve solubility.[12, 14] To maximize access of nonpeptide RGD to $\alpha_V\beta_3$ integrins, PEG is positioned between GG and nonpeptide RGD to avoid sterical interactions between PGG-PTX and nonpeptide RGD (see Fig. 5.1). Conjugation of PEG to therapeutic agents has also been shown to result in improved *in vivo* stability, protection from proteolytic digestion, increased biological half-life, improved solubility, and decreased toxicity.[6]

Preclinical development of anticancer therapeutics usually involves trial-and-error testing of candidate compounds on *in vitro* and *in vivo* models. While these methods yield useful results, their highly experimental nature results in a time-consuming and resource-intensive procedure that is rather inefficient. Given the immediate clinical needs of cancer patients, there is an unmet need to facilitate preclinical testing of therapeutic agents. For PGG-PTX-PEG-npRGD, molecular dynamics (MD) simulations were used to investigate physicochemical properties on multiple conformations, such as shape, flexibility, and surface hydrophilicity which have been shown or suggested to influence how nanoparticles overcome biological barriers.[3, 55, 62, 90, 91] It was hypothesized that the density of nonpeptide RGD (4, 8, 12, and 16 ligands) and molecular weight of PEG spacer (500 Da, 1000 Da, and 2000 Da) concomitantly affects the shape, flexibility, and surface hydrophilicity of a PGG-PTX-PEG-npRGD molecule. (Fig. 5.2

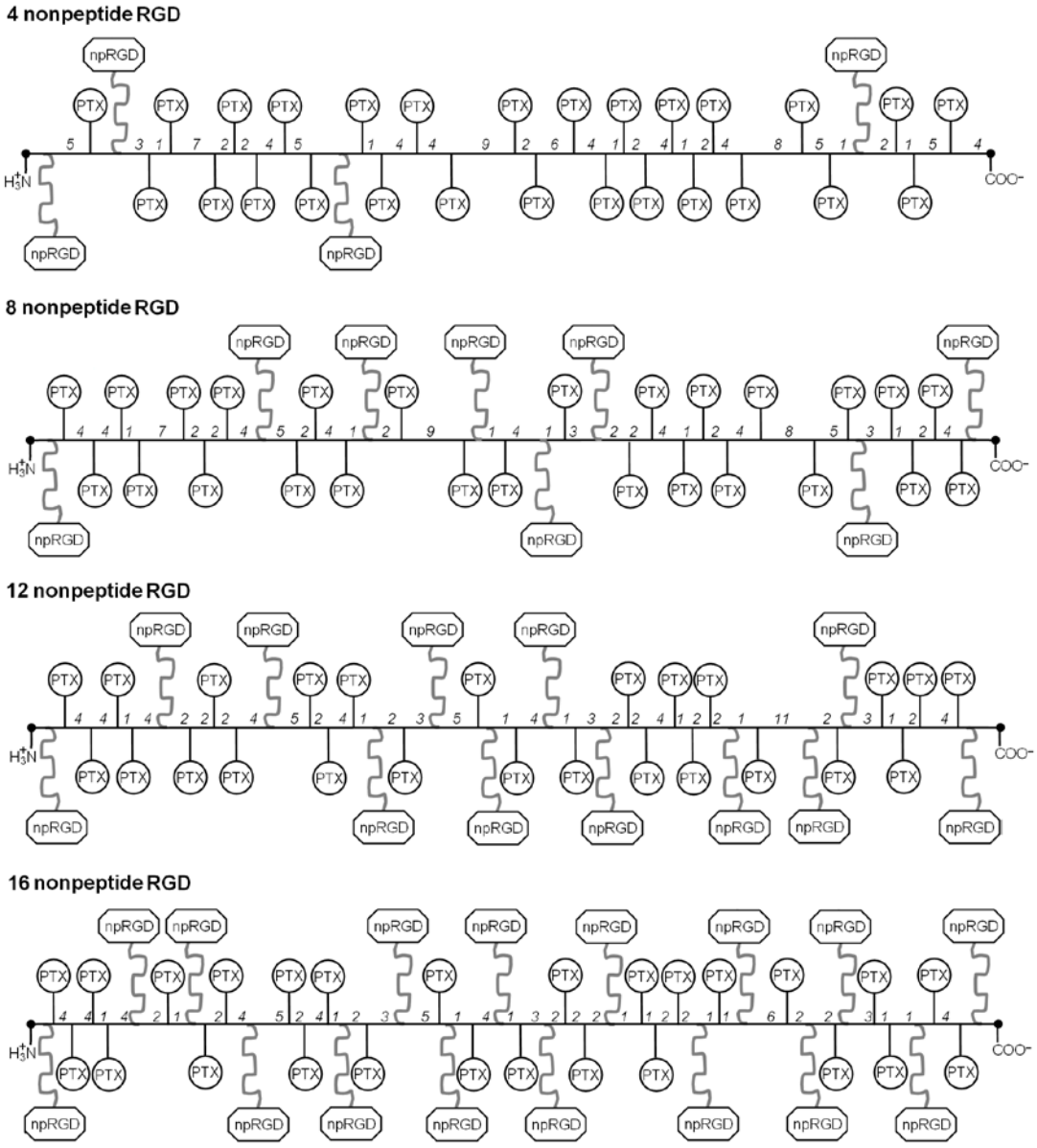

Figure 5.2. Abstract representations of the spatial positioning patterns of paclitaxel and nonpeptide RGD residues on the PGG backbone. Patterning schemes apply to all PEG500, PEG1000, and PEG2000 systems. Each PGG-PTX molecule is composed of 130 poly(γ-glutamyl-glutamate) monomers, 26 paclitaxel molecules, and 4, 8, 12, or 16 nonpeptide RGD molecules. Paclitaxel and nonpeptide RGD molecules are covalently attached to the PGG backbone in a random fashion. Numbers between residues denote the number of repeating GG residues that are not amino- or carboxyl-termini GG residues. The amino- and carboxyl-termini GG residues are represented by black dots at the ends of each line.

shows the patterning schemes for the PGG-PTX-PEG-npRGD molecules.) Theoretical insight from expediting the preclinical development of PGG-PTX-PEG-npRGD.

Prior to running MD simulations, there were challenges in the methodology that needed to be addressed. First, the starting structure of PGG-PTX-PEG-npRGD was unknown, as no structure representing its experimental form was available on the Protein Data Bank. Therefore, circular dichroism spectroscopy was used to obtain a general idea of the initial structure, which was used to construct the all-atom (AA) models. Next, given the relatively large sizes of the PGG-PTX-PEG-npRGD molecules (~90-130 kDa), running MD simulations on AA models in explicit solvent would require an extraordinary amount of CPU expenses. Therefore, to minimize computational costs and access longer time scales, AA models were converted to coarse-grained (CG) models using the mapping scheme in the MARrink's Toolkit INItiative (MARTINI) force field.[32] CG parameterization of the models was done by using the Boltzmann inversion to determine the equilibrium bonded distances and angles from 100 ns AA MD simulations in implicit solvent. Finally, determining when to end the simulations was not straightforward; given the semiflexible nature of PGG-PTX-PEG-npRGD, the molecule was not expected to adopt a specific conformation. Thus, CG MD simulations were run on the PGG-PTX-PEG-npRGD were run to statistical equilibrium at 4 μs (effective time), at which each PGG-PTX-PEG-npRGD conformation was represented by an ensemble of statistically similar structures, and minimal fluctuations exist at the molecular level.

5.2 Experimental Methods

5.2.1 Sample preparation

A lyophilized sample of PGG-PTX-PEG220-npRGD$_{16}$ was provided by Nitto Denko Technical Corporation (Oceanside, CA). The sample was weighed and then diluted to 1mg/ml in 1X HyClone modified DPBS buffer (ThermoScientific, Cat. No. SH30028.03). The sample was then sonicated in a 37ºC water bath for 15 min and vortexed at room temperature for 1 min. The samples were then allowed to settle at room temperature for an additional 10 min. Finally, the sample was filtered using a 0.2 μm filter paper (Corning, Part No. 431215) and a 20G 1½ Precision Glide needle (Becton Dickinson).

5.2.2 Circular dichroism spectroscopy

CD spectroscopy measurements for the PGG-PTX-PEG220-npRGD$_{16}$ sample were carried out using an AVIV Model 202 spectrophotometer. CD spectra of pure 1X DPBS buffer and FD protein in 50% TFE/50% double distilled H_2O/0.1% TFA were also taken as the negative and positive controls, respectively. All measurements were taken at 37ºC. The far-UV CD spectra were recorded from 190 to 260 nm using a 1 cm rectangular quartz cuvette, and the CD spectra were collected at every 0.5 nm with 5 sec at each point. For each sample except pure 1X DPBS, the concentration was adjusted and diluted so that the dynode voltage corresponding to the ellipticity signal remained below 500 V throughout the entire spectra collection period. (It has been suggested by Greenfield et al. that the signal-to-noise ratio will greatly diminish once the dynode voltage exceeds 500 V.[24]) The optimum concentrations of each sample leading to optimum ellipticity signal and lowest signal-to-noise ratio were determined to be: 1

mg/ml of PGG-PTX-PEG220-npRGD$_{16}$ in 1X DPBS and 0.25 mg/ml of FD protein in 50% TFE/50% ddH_2O/0.1% TFA.

5.3 Computational Methods

5.3.1 All-atom modeling

5.3.1.1 Model construction

The initial structures and input files for the following residues were constructed in the *xleap* module of AMBER 9.0: GG, GG_{COO-}, GG_{NH3+}, GG-PTX, GG-PEG500-npRGD, GG-PEG1000-npRGD, and GG-PEG2000-npRGD. The initial structure for paclitaxel (PDB ID: 1JFF) was provided by the Protein Data Bank.[34] The Gaussian (g03) program's geometry optimization and restrained electrostatic potential fitting (RESP) were carried out to generate the atom-centered point charge for all residues.[35, 36] For the protonated molecules, hydrogen atoms were added to the carboxyl groups to achieve their ionized states. To obtain the electrostatic potential for these residues, the AM1 geometry scheme and the HF/6-31G* and HF/6-31G** pop=mk iop(6/33=2) *ab initio* level calculations were performed using the Gaussian program. Finally, RESP fitting was applied on the electrostatic potentials to derive the equivalent partial atomic charges for the molecules.

5.3.1.2 Energy minimization and MD simulation

These steps were carried out using the AMBER 9.0 *sander* module. Each molecule was solvated and minimized in implicit solvent using the modified Generalized-Born model of IGB=2 and the LPCO model.[37, 38] 250 steps of steepest descent followed by 1750 steps of conjugate gradient were carried out. The ionic strength of the implicit

solvent was set to 140 mM to mimic the salt concentration of blood plasma. No periodic boundary conditions were applied. A non-bonded electrostatic cutoff of 16.0Å was used. Trajectory snapshots were saved every 100 steps for further reprocessing.

MD simulations were also carried out using the *sander* module applying the modified version (ff99SB) of the Cornell et al. parm99 and GAFF force fields in the NVT ensemble (in which the number of atoms N, volume V, and temperature T were fixed) at 310K in implicit solvent without periodic boundary conditions.[30, 31, 39] Constant temperature scaling was also applied with a time constant of 0.5 ps. Langevin dynamics was used with a collision frequency of 2.0 ps^{-1}. Newton's equations of motions were integrated with a time step of 2 fs. All bonds involving hydrogen atoms were constrained using the SHAKE algorithm.[40] The rotational and translational degree of freedom about the center of mass was eliminated. Trajectory snapshots were saved every 100 steps for later reprocessing. Each cycle of the MD simulation was run for 0.1 ns; this step was repeated until a statistical equilibrium was reached at 100 ns.

5.3.2 Coarse-grained modeling

5.3.2.1 CG mapping

The MARTINI force field was selected for the CG parameterization for its successful application to proteins by experimental validation of their structural and thermodynamic properties as well as the amino acid-based nature of the glutamyl-glutamate backbone.[32, 43] The MARTINI force field dictates that a group of roughly 4-5 atoms are represented as an interaction center, or bead. The only exception applies to aromatic groups, in which a mapping scheme of 2 heavy atoms-to-1 bead was applied in order to maintain their geometric symmetry, namely, the benzene entities in paclitaxel

and nonpeptide RGD. These beads interact through a set of short-range Lennard-Jones potentials to reproduce characteristic properties resulting from AA simulations. Charged groups interact via a Coulombic energy function, and bonded potentials are used to describe the chemical connectivity of the beads. CG mapping of the GG, GG_{COO-}, GG_{NH3+}, and GG-PTX residues was previously done in Peng et al.[63] CG mapping of the GG-PEG500-npRGD residue is shown in Fig. 5.3, and CG mapping of the GG-PEG1000-npRGD and GG-PEG2000-npRGD residues are provided in Fig. 5.7. Also, each Na+ ion is represented as a single Q type bead, and four AA water molecules are mapped to a single P_4 type bead (W).

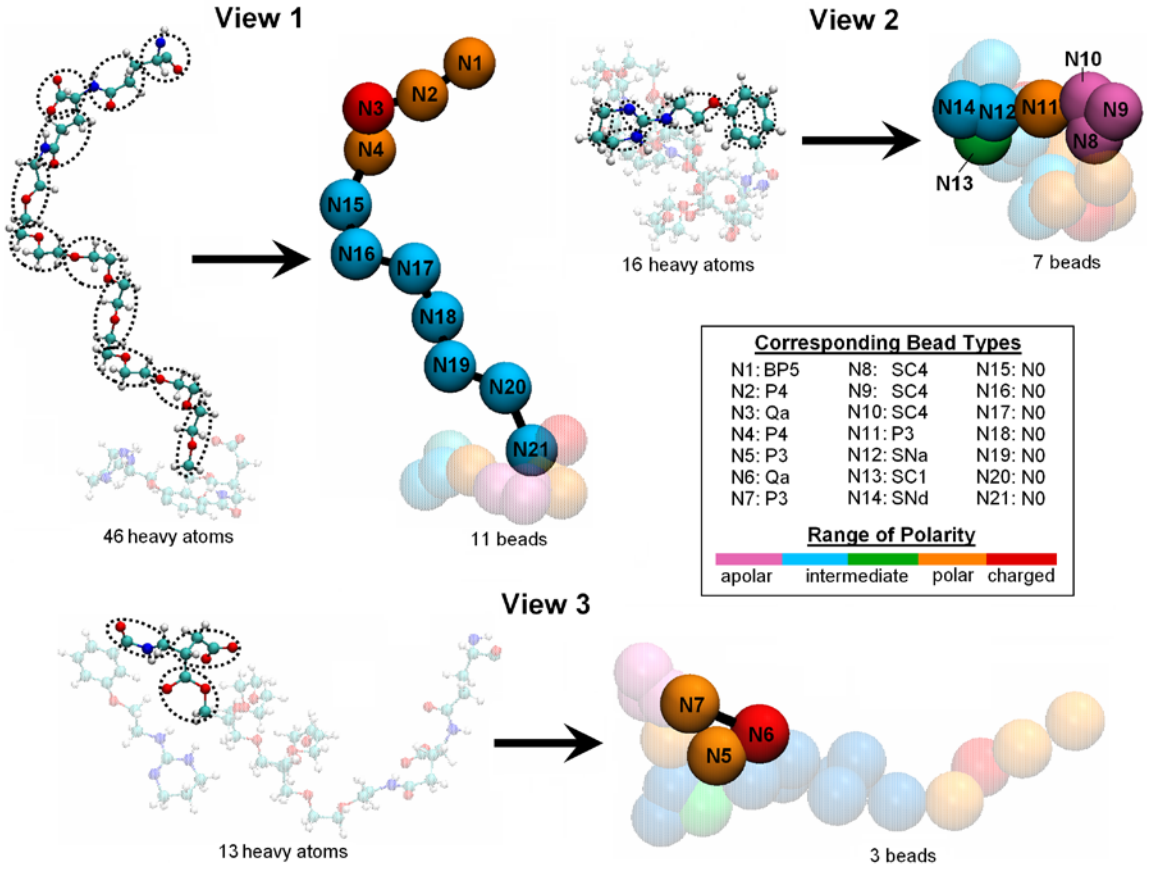

Figure 5.3. Coarse-grained representation of a GG-PEG500-npRGD residue. GG-PEG500-npRGD was reduced from 75 heavy atoms to 21 CG beads. (CG representations for the GG-PEG1000-npRGD and GG-PEG2000-npRGD residues are shown in Fig 5.7.)

5.3.2.2 Theory

The dynamics of the beads are described by Newton's equations of motion. The effective bonded and nonbonded interactions are described by a potential of the form, adapted from Marrink et al.:[43]

$$V = \sum_m \left[V_{bond}^m + V_{angle}^m + V_{dihedral}^m \right] + V_{nonbonded}^m \quad (1)$$

where the index *m* represents a bead from a PGG-PTX-PEG-npRGD molecule, Na+ ion, or W bead. V_{bond} represents the forces between two successively bonded beads, V_{angle} accounts for the forces used to sustain angles between three successively bonded beads, and $V_{dihedral}$ corresponds to the dihedral angle potential for four successively bonded beads. The $V_{nonbonded}$ term accounts for the nonbonded interactions among all of the beads in a system. The bonded interactions are used to describe the chemical connectivity of the beads and are characterized as one of the following (the indices *i*, *j*, *k*, and *l* represent four consecutive beads):

$$V_{bond}^m = \sum_{ij} \tfrac{1}{2} k_{ij}^m \left(r_{ij}^m - r_{0,ij}^m \right)^2 \quad (2)$$

where r_{ij}^m is the distance between two consecutive beads *i* and *j*, $r_{0,ij}^m$ is the equilibrium bond length, and k_{ij}^m is the distance force constant. The potential for bond angles is:

$$V_{angle}^m = \sum_{ijk} \tfrac{1}{2} k_{ijk}^m \left[\cos\left(\theta_{ijk}^m\right) - \cos\left(\theta_{0,ijk}^m\right) \right]^2 \quad (3)$$

where θ_{ijk}^m is the angle between beads *i*, *j*, and *k*, and $\theta_{0,ijk}^m$ is the equilibrium angle, and k_{ijk}^m is the angle force constant.

The dihedral potential, $V_{dihedral}$, only applies to backbone protein residues. Since the general structure of PGG-PTX-PEG-npRGD has been shown to adapt a random coil, $V_{dihedral}$ was set to 0 for all combinations of four successively connected beads:

$$V_{dihedral}^{m} = \sum_{ijkl} k_{ijkl}^{m} \left[1 + \cos\left(n\chi_{ijkl}^{m} - \delta_{ijkl}^{m}\right)\right] \quad (4)$$

where *n* is an integer that represents multiplicity, δ_{ijkl}^{m} is the phase shift, χ_{ijkl}^{m} is the angle between the plane formed by the first three beads *i*, *j*, and *k* and the plane formed by the last three beads *j*, *k*, and *l*, and k_{ijkl}^{m} is the dihedral force constant.

Nonbonded interactions between two beads are described by a van der Waals (vdW) potential, characterized by a Lennard-Jones 12-6 potential energy function and a Coulombic potential for charged beads. The following summation is performed over all pairs of nonbonded beads *m* and *n* separate by a distance of r_{mn}.

$$V_{nonbonded} = \sum_{m,n} 4\varepsilon_{mn} \left[\left(\frac{\sigma_{mn}}{r_{mn}} \right)^{12} - \left(\frac{\sigma_{mn}}{r_{mn}} \right)^{6} \right] + \sum_{m,n} \frac{q_m q_n}{4\pi\varepsilon_0 \varepsilon r_{mn}} \quad (5)$$

where constants σ_{mn} and ε_{mn} are the vdW parameters for the bead interaction, σ_{mn} refers to a typical closest distance of approach between two beads *m* and *n*, and ε_{mn} denotes the strength of the interactions between beads *m* and *n*. The charges q_m and q_n of the *m*th and *n*th beads, respectively, and the vacuum dielectric permittivity ε_0 are included. A relative dielectric constant of $\varepsilon = 15$ is assumed for all electrostatic interactions.

5.3.2.3 CG parameterization

The bonded distances and angles for the PGG-PTX-PEG-npRGD molecules were determined as follows: 1) MD simulations of the twelve AA PGG-PTX-PEG-npRGD models were run to 100 ns; 2) the bonded distances and values for the assigned beads

were extracted from the AA MD simulations using the AMBER 9.0 *ptraj* module; and 3) the Boltzmann inversion was used to extract the equilibrium bonded distances and angles [44]. These values were averaged for each set of four PGG-PTX-PEG-npRGD molecules with the same PEG molecular weight. (For example, the bonded distances and angles for the four PEG1000 molecules were averaged together; the resulting values were used for the parameterizing the PGG-PTX-PEG1000-npRGD$_4$, PGG-PTX-PEG1000-npRGD$_8$, PGG-PTX-PEG1000-npRGD$_{12}$, and PGG-PTX-PEG1000-npRGD$_{16}$ molecules.) CG topologies for the GG, GG$_{COO-}$, GG$_{NH3+}$, and GG-PTX residues were taken from Peng et al.;[63] CG topologies for the GG-PEG500-npRGD residue is provided in Table 5.1; and CG topologies of the GG-PEG1000-npRGD and GG-PEG2000-npRGD residues are provided in Tables 5.5 and 5.6, respectively.

Table 5.1. Coarse-grained topology for GG-PEG500-npRGD

i j	**Bond length** $r_{0,ij}$ **[nm]**	**Force constant** k_{ij} **[kJ nm^{-2} mol^{-1}]**	*i j k*	**Bond angle** $\theta_{0,ijk}$ **[°]**	**Force constant** k_{ijk} **[kJ nm^{-2} mol^{-1}]**
N1 N2	0.40	7500*	N1 N2 N3	134	100*
N2 N3	0.38	7500*	N2 N3 N4	85	100*
N3 N4	0.56	7500*	N6 N5 N7	90	100*
N5 N6	0.35	7500*	N7 N8 N9	170	100*
N5 N7	0.36	7500*	N8 N9 N10	60	100*
N7 N8	0.34	7500*	N9 N10 N8	60	100*
N8 N9	0.27*	7500*	N9 N8 N10	60	100*
N9 N10	0.27*	7500*	N9 N11 N12	136	100*
N8 N10	0.27*	7500*	N12 N13 N14	60	100*
N9 N11	0.35	7500*	N13 N14 N12	59	100*
N11 N12	0.35	7500*	N3 N4 N15	143	100*
N12 N13	0.34	7500*	N4 N15 N16	131	100*
N13 N14	0.35	7500*	N15 N16 N17	135	100*
N12 N14	0.34	7500*	N16 N17 N18	130	100*
N4 N15	0.42	7500*	N17 N18 N19	123	100*
N15 N16	0.36	7500*	N18 N19 N20	128	100*
N16 N17	0.34	7500*	N19 N20 N21	122	100*
N17 N18	0.45	7500*	N20 N21 N5	105	100*
N18 N19	0.35	7500*			
N19 N20	0.33	7500*			
N20 N21	0.44	7500*			
N21 N5	0.41	7500*			

*Taken from the predetermined values for backbone or sidechain bonded parameters from the MARTINI force field. CG topologies for the GG-PEG1000-npRGD and GG-PEG2000-npRGD residues are shown in Table 5.4.

5.3.2.4 MD simulation

CG models of the twelve PGG-PTX-PEG-npRGD molecules were constructed using the *atom2cg* and *itp-generating* scripts provided by the MARTINI tutorials.[92] Each PGG-PTX-PEG-npRGD molecule was solvated in explicit solvent comprising of W beads. Due to the negative charges imparted by the glutamyl-glutamate residues, Na+ ions were added in place of water molecules to neutralize the system. The simulations were carried out under NPT (the number of particles N, pressure P, and temperature T are fixed) conditions at a constant temperature of 310 K with a coupling constant of $\tau_T = 0.1$ ps and a constant pressure of 1 bar with a relaxation time of $\tau_P = 0.5$ ps. The cutoff length used for the nonbonded interactions was $r_{cut} = 1.2$ nm. Lennard-Jones and Coulombic forces were considered for $r_{cut} < 0.9$ nm and $r_{cut} < 1.2$ nm, respectively. Coulombic forces were computed every time step for 1.0 nm and once every 10 time steps for 0.9 nm < r_{cut} < 1.2 nm. The time step in the leap-frog integration scheme was 5 fs. The energies, coordinates and velocities were written every 0.5 ps. MD simulations were run for 1 μs. However, since the underlying energy landscape for CG simulations is much smoother as a result of larger particle sizes, CG dynamics are much faster than AA dynamics. Therefore, the simulation timescale was scaled up by a factor of four resulting in an effective time of 4 μs.[32, 43, 46]

5.3.3 RMSD clustering

Root-mean-square deviation (RMSD) clustering, a quantitative method used to analyze protein structures,[19, 69, 70, 93] was used to determine the PGG-PTX-PEG-npRGD conformations. All molecular conformations accessed throughout an MD trajectory were

categorized into clusters based on structural similarity. For each cluster, a structure from the MD trajectory closest to the conformational average of all structures in the MD trajectory was regarded as the representative conformation. Using the *g_cluster* module of the GROMACS 4.0.3 package, the RMSD cutoff length was manually optimized to so the following criteria were met: 1) there were approximately 40 clusters total, 2) very few clusters contained just one configuration, and 3) 90% of the MD trajectory was in clusters fewer than those with one configuration. Table 5.2 provides the optimized RMSD cutoff distances for all twelve PGG-PTX-PEG-npRGD molecules. (Sample optimization of the RMSD cutoff length vs. number of clusters generated for the GGG-PTX-PEG1000-$npRGD_{12}$ molecule is shown in Fig. 5.8.) After optimization of the RMSD cutoff lengths, the significance of every cluster was assessed such that its corresponding frames must occupy at least 10% of the entire 4 μs trajectory. Once the clusters were judged to be sufficiently significant, each was evaluated for its uniqueness based on the following stipulation: if the RMSD between the central members of each significant cluster was greater than twice the RMSD cutoff length, then those clusters were regarded as unique. (For the PGG-PTX-PEG-npRGD molecules with only one central member, that central member was automatically deemed unique.) To verify the uniqueness among clusters, the RMSD Calculator tool in Visual Molecular Dynamics (VMD) 1.8.6 was used.[94]

Table 5.2. Summary of RMSD between central members, RMSD cutoff lengths, and number of corresponding clusters for each PGG-PTX-PEG-npRGD molecule

PEG MW	Molecule Number of nonpeptide RGD molecules	RMSD cutoff (nm)	Number of clusters	Central member(s)		RMSD between central members
500	4	0.57	37	A	B	17.7
	8	0.59	38	A	B	7.2
	12	0.56	37	--		--
	16	0.53	40	A	B	6.6
1000	4	0.59	37	A	B	8.0
	8	0.61	38	A	B	6.2
	"	"	"	A	C	4.9
	"	"	"	B	C	4.1
	12	0.52	39	A	B	9.6
	"	"	"	A	C	7.3
	"	"	"	B	C	4.3
	16	0.53	40	--		--
2000	4	4.6	36	--		--
	8	0.60	38	--		--
	12	0.93	37	--		--
	16	0.59	38	--		--

5.3.4 Solvent-accessible surface area (SASA) analysis

The solvent-accessible surface area (SASA) indicates the area of a particular species that is exposed to the solvent. The SASA of the PGG-PTX-PEG-npRGD molecules was analyzed in VMD 1.8.6 using a solvent probe radius of 2.4 nm. For each PGG-PTX-PEG-npRGD molecule, the SASA of the entire molecule was calculated, along with the SASA of PGG, PEG, PTX, and nonpeptide RGD entities of each PGG-PTX-PEG-npRGD molecule (see Table 5.7). The contribution of each entity was then determined by taking the fraction of the SASA for a particular entity with respect to the SASA of the whole PGG-PTX-PEG-npRGD molecule, or the percentage (%) SASA. Table 3 shows the % SASA for the PGG, PEG, PTX, and nonpeptide RGD entities for all PGG-PTX-PEG-npRGD molecules.

5.4 Results and Discussion

5.4.1 Circular dichroism spectroscopy

Circular dichroism spectroscopy was used to determine the secondary structure of a PGG-PTX-PEG220-npRGD$_{16}$ molecule. This method of determining the initial structure was originally applied on PGG-PTX in Peng et al.[63] Although PGG-PTX-PEG220-npRGD$_{16}$ was not one of the PGG-PTX-PEG-npRGD molecules pursued in this study, its chemical structure is similar enough to provide an accurate representation of the PGG-PTX-PEG-npRGD molecules being studied.

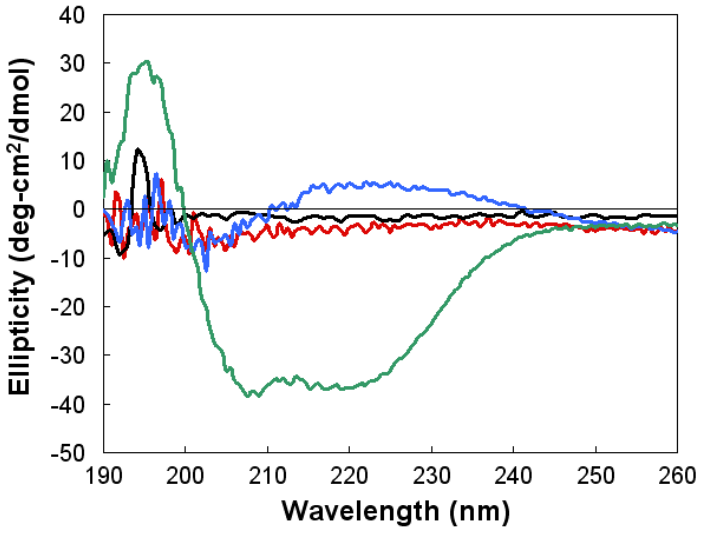

Figure 5.4. CD spectra of samples. Shows the spectra for PGG-PTX-PEG220-npRGD$_{16}$ *(red line)*, PGG-PTX *(blue line)*, FD protein *(green line)*, and pure 1X DPBS *(black line)*.

Fig. 5.4 shows the CD spectra of 1mg/ml PGG-PTX-PEG220-npRGD$_{16}$ dissolved in 1X DPBS. The curve is most representative of a random coil at physiological temperature of 37ºC. The negative control of 1X DPBS at 37ºC indicates that that there is no signal interference that may have influenced the conditions while CD spectrum of PGG-PTX-PEG220-npRGD$_{16}$ was being taken. For the positive control, the shape of the

alpha-helical FD protein, a bZIP transcription factor in a floral pathway,[47] in 50% TFE/50% ddH_2O/0.1% TFA buffer does indeed corresponds to an alpha-helix, as compared with the CD spectrum of the alpha-helical poly-γ-tyrosine.[48] The lowest part of the curve is ~215nm and the highest point of the curve is ~200nm collectively indicate that the FD protein is indeed alpha-helical. Since PGG-PTX-PEG220-npRGD$_{16}$ exists as a random coil, this data suggest that the PGG-PTX-PEG-npRGD molecules being modeled most likely exist as random coils. Therefore, their existence as random coils poses no stipulations on the construction of AA models of PGG-PTX-PEG-npRGD.

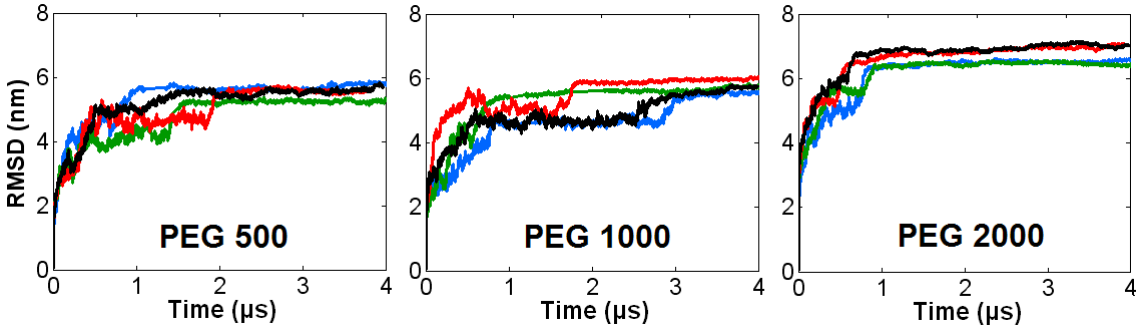

Figure 5.5. RMSD time evolutions of PGG-PTX-PEG-npRGD molecules. Shows the data for the molecules with 4 npRGD *(blue line)*, 8 npRGD *(green line)*, 12 npRGD *(red line)*, and 16 npRGD *(black line)*.

5.4.2 RMSD values

Fig. 5.5 shows the RMSD time evolutions for all PGG-PTX-PEG-npRGD molecules. Most time evolutions rose up to ~6-7 nm and reached a statistical equilibrium by 4 μs. Given the relatively large sizes of these systems, these values are reasonable. The RMSD values for the PEG2000 molecules are slightly higher than the PEG500 and PEG1000 molecules by 1 nm, whereas the RMSD values for the PEG500 and PEG1000 molecules are comparable. This 1 nm difference is in accordance with the size of the molecular systems, as the PEG2000 molecules are the largest. In addition, the time it

takes for PGG-PTX-PEG-npRGD molecules to attain statistical equilibrium depends on the PEG molecular weight (MW). The PEG1000 molecules take the longest time to reach equilibrium, as some molecules do not reached a plateau until 3 μs. Contrariwise, the PEG2000 molecules take the least time to reach equilibrium; by 1 μs, all molecules have attained a statistical equilibrium. The time it takes for the PEG500 molecules to reach a plateau is ~2 μs, which is intermediate compared to the time it takes for the PEG1000 and PEG2000 molecules to reached equilibrium. This behavior suggests that the PEG1000 molecules fluctuate the most, accessing a wider range of molecular conformations throughout the 4 μs MD trajectory.

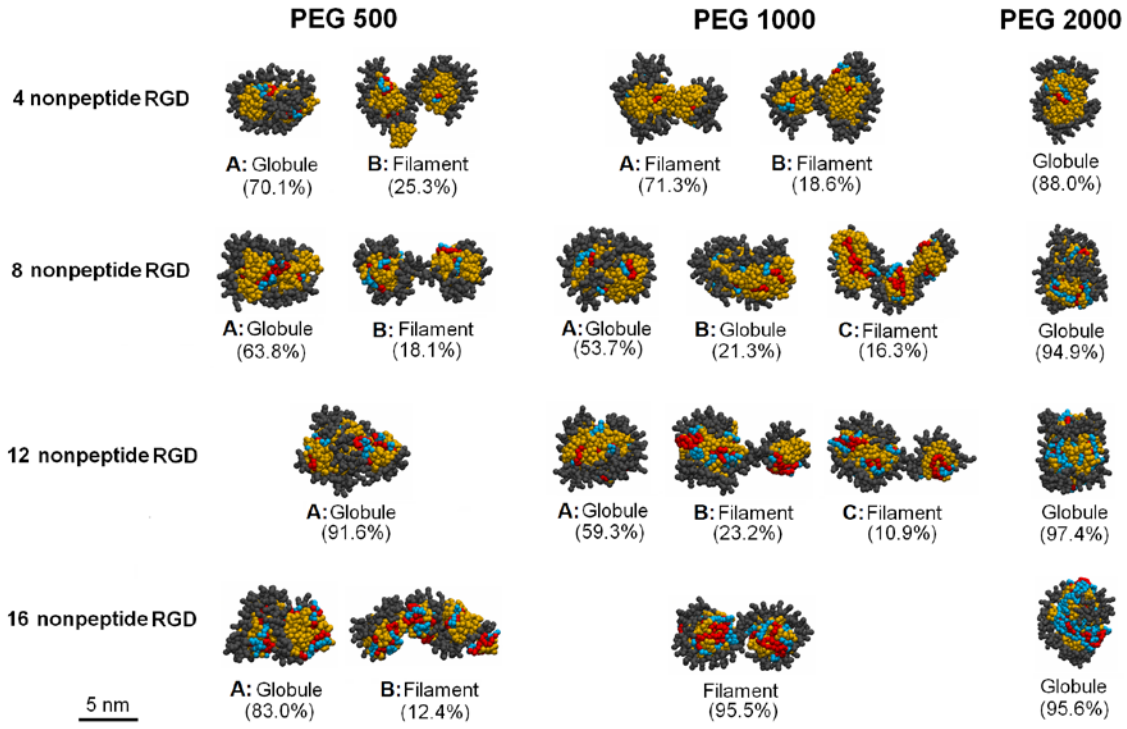

Figure 5.6. Representative conformations of PGG-PTX-PEG-npRGD molecules. Each structure shows the glutamyl-glutamate *(grey)*, paclitaxel *(yellow)*, PEG *(blue)*, and nonpeptide RGD *(red)* molecules. Explicit water molecules and Na+ ions are not shown. Representing an actual frame in the trajectory, the central member embodies the configuration that is the most similar to the average of all configurations in that cluster. The percentage indicates the population of frames, or % trajectory occupancy, corresponding to that particular cluster for the full 4 μs MD trajectory.

5.4.3 Implications of shape of a PGG-PTX-PEG-npRGD molecule

Dennis Discher and colleagues have demonstrated that filamentous particles retains a longer circulation half-life in the bloodstream, thus decreasing levels of clearance by the reticoendothelial system (RES) and improving chances of the nanoparticle to reach the target tumor.[3] Also, nonspherical nanoparticles have been shown to adhere more firmly to walls of tumor endothelia.[55] Fig. 5.6 shows the representative conformations of all PGG-PTX-PEG-npRGD molecules. The geometry of each molecule was characterized as a filament (wormlike and threadlike) or globule (round). In general, most molecules are globules, which is most likely attributed to hydrophobic driving force among PTX that are uniformly distributed along the PGG backbone. The uniform distribution of PTX causes the entire PGG-PTX-PEG-npRGD to self-assemble into a globule in which the PTX are located in the core, where it is the furthest away from the solvent and surrounded by hydrophilic PGG. Other molecules, such as PGG-PTX-PEG1000-npRGD$_4$ and PGG-PTX-PEG1000-npRGD$_{12}$, exhibit both filamentous and globular behavior. The PEG1000 molecules exhibit the most filamentous behavior, as each one of its four molecules is characterized by a filamentous conformation. The higher prominence of filaments in the PEG500 and PEG1000 molecules is possibly a result of the sterical interactions among the rigid, conformationally constrained nonpeptide RGD residues that hinder the formation of a more compact globule. For the PEG2000 molecules, however, the prominence of the globular shapes (~90%) suggest that 2000 Da is the PEG molecular weight to prevent sterical interactions among nonpeptide RGD residues, thus allowing the PGG-PTX-PEG-npRGD molecules to form a globule. Overall, the results suggest that the PGG-PTX-

PEG-npRGD molecules with PEG500 and PEG1000 spacers are more efficacious than the molecules with PEG2000 spacers. While the molecular weight of the PEG spacer influences that shape of a PGG-PTX-PEG-npRGD molecule, the density of nonpeptide RGD ligands only has minimal impact.

5.4.4 Implications of flexibility of a PGG-PTX-PEG-npRGD molecule

S. Takeoka has speculated that higher molecular flexibility of nanoparticles promotes more surface interactions to tumor cells.[62] The flexibility of each PGG-PTX-PEG-npRGD molecule was assessed by the number of representative conformations of each molecule and, for those systems with multiple representative conformations, the similarity in the representative conformations. A higher number of representative conformations indicates a stronger tendency for that molecule to fluctuate and change shape. The PEG1000 molecules have the most representative conformations; the PGG-PTX-PEG1000-npRGD$_8$ and PGG-PTX-PEG1000-npRGD$_{12}$ molecules are characterized by three representative conformations, although with mediocre significance (~10-20%). On the contrary, each PEG2000 molecule has only one unique shape with very high significance (~90%). Moreover, the degree of similarity among the representative conformations is also an indicator of flexibility: a PGG-PTX-PEG-npRGD molecule with two globular representative conformations is less flexible than a molecule characterized by globular and filamentous conformations. For instance, PGG-PTX-PEG500-npRGD$_4$ and PGG-PTX-PEG1000-npRGD$_4$ each has two representative conformations, but a larger structural difference exists between the globular and filamentous shapes of the PGG-PTX-PEG500-npRGD$_4$ molecule, as compared to the two filamentous conformations of the PGG-PTX-PEG1000-npRGD$_4$ molecule. In all, these observations

show that the PEG2000 molecules are the least flexible, whereas the PEG500 and PEG1000 molecules are more flexible and thus bind more effectively to tumor cells. Finally, the density of the nonpeptide RGD ligands does not have a significant affect on the flexibility of a PGG-PTX-PEG-npRGD molecule.

Table 5.3. Solvent-accessible surface area of PGG-PTX-PEG-npRGD molecules

System	% $SASA_{PGG}$	% $SASA_{PEG}$	% $SASA_{phil}$*	% $SASA_{PTX}$	% $SASA_{npRGD}$
PEG 500					
4 nonpeptide RGD					
A	78.5	1.1	79.6*	18.2	2.2
B	69.5	1.9	71.4*	25.7	2.9
8 nonpeptide RGD					
A	73.1	1.6	74.7*	21.5	3.9
B	73.3	1.5	74.8*	20.4	4.9
12 nonpeptide RGD	68.2	2.8	70.0*	19.0	8.2
16 nonpeptide RGD					
A	66.9	3.7	70.6*	18.7	10.6
B	58.1	6.2	64.3*	23.8	11.8
PEG1000					
4 nonpeptide RGD					
A	74.2	0.3	74.5*	24.2	1.2
B	74.9	1.1	76.0*	22.3	1.8
8 nonpeptide RGD					
A	78.3	2.0	80.3*	16.4	3.4
B	64.7	5.8	70.5*	25.2	4.3
C	71.7	2.4	74.1*	22.8	3.1
12 nonpeptide RGD					
A	78.7	0.5	79.2*	15.0	5.8
B	73.2	0.4	73.6*	18.7	7.7
C	73.9	0.4	74.3*	18.8	6.9
16 nonpeptide RGD	74.1	0.6	74.7*	16.0	9.2
PEG2000					
4 nonpeptide RGD	78.9	1.8	80.7*	17.8	1.5
8 nonpeptide RGD	72.6	6.5	79.1*	17.0	3.8
12 nonpeptide RGD	68.3	8.4	76.7*	16.9	6.4
16 nonpeptide RGD	66.0	12.5	78.5*	12.3	9.2

* Sum of **% $SASA_{PGG}$** and **% $SASA_{PEG}$**.

5.4.5 Implications of surface hydrophilicity of a PGG-PTX-PEG-npRGD molecule

Nanoparticles with higher degrees of surface hydrophilicity have been shown to possess longer circulation half-lives in the bloodstream, suggesting a higher preference

for accumulating in leaky vasculature of tumors.[90] The degree of surface hydrophilicity of each PGG-PTX-PEG-npRGD molecule was assessed by the % SASA of the hydrophilic entities – PGG and PEG (see Table 5.3). As expected, the surface hydrophilicity increases with PEG molecular weight, and an increase in the density of nonpeptide RGD results in higher % $SASA_{npRGD}$. A higher density of nonpeptide RGD ligands tends to cause a decrease in the % $SASA_{phil}$. While nonpeptide RGD is used to promote active targeting of PGG-PTX to tumor cells, too many nonpeptide RGD ligands may decrease surface hydrophilicity, which may be unfavorable to the circulation half-life. To ensure that PGG-PTX-PEG-npRGD remains in the bloodstream long enough to convectively diffuse into leaky vasculature of tumors. At the same time, adequate amounts of nonpeptide RGD ligands must be exposed to the solvent to achieve effective binding to $\alpha_V\beta_3$ integrins. Therefore, optimization of the density of nonpeptide RGD ligands is necessary for attaining optimal efficacy of PGG-PTX-PEG-npRGD. Taking these factors into consideration, the PGG-PTX-PEG-npRGD molecules with 8 and 12 nonpeptide RGD ligands and PEG1000 and PEG2000 are most likely to confer the longest circulation half-lives and effective targeting to $\alpha_V\beta_3$ integrins on tumor cells.

5.5 Recommendations

This study was based on the hypothesis found the degree of PEGylation (500 Da, 1000 Da, and 2000 Da) and density of nonpeptide RGD ligands (4, 8, 12, and 16 nonpeptide RGD per PGG-PTX-PEG-npRGD molecule) together affect the shape, flexibility, and surface hydrophilicity of PGG-PTX-PEG-npRGD. The results

demonstrated that the PEG500 and PEG1000 molecules exhibited more filamentous behavior and higher flexibility, whereas the PEG2000 molecules are all globular and more rigid. An increase in the nonpeptide RGD ligand density may result in lower surface hydrophilicity, yet not enough nonpeptide RGD ligands may prevent PGG-PTX-PEG-npRGD from achieving effective targeting to tumor cells. All factors considered, the ideal PGG-PTX-PEG-npRGD candidate would possess the following properties: filamentous shape, high flexibility, and high surface hydrophilicity. Based on the results, the PGG-PTX-PEG1000-npRGD$_4$ and PGG-PTX-PEG1000-npRGD$_8$ molecules best fulfilled these criteria and are the most promising candidates.

5.6 Conclusions

There has been increasing attention on the roles of certain physicochemical properties, such as shape, flexibility, and surface hydrophilicity, in influencing the delivery of therapeutic nanoparticles to tumors. Knowledge of these implications can serve as a basis for the design of anticancer therapeutics, such as PGG-PTX-PEG-npRGD. While it would be technically feasible to determine these properties using experimental methods, the effort required to synthesize all candidate compounds and subsequently perform experimental testing would be very time- and resource-intensive, especially since the testing is usually conducted in a trial-and-error manner. Therefore, MD simulations were used to explore the shape, flexibility, and surface hydrophilicity of candidate PGG-PTX-PEG-npRGD compounds in a more efficient and controlled manner. The theoretical results can be used to further guide experiments, ultimately facilitating the preclinical development of PGG-PTX-PEG-npRGD.

5.6 Supporting Information

Table 5.4. Coarse-grained topologies for GG and GG-PTX

GG Sidechain Topology (includes NH_3^+ and COO^- termini residues)

i j	Bond length $r_{0,ij}$ [nm]	Force constant k_{ij} [kJ nm^{-2} mol^{-1}]	*i j k*	Bond angle $\theta_{0,ij}$ [°]	Force constant k_{ijk} [kJ nm^{-2} mol^{-1}]
G1 G2	0.39	7500*	G1 G2 G3	143	100*
G2 G3	0.38	7500*	G2 G3 G4	85	100*
G3 G4	0.37	7500*			

Backbone Topology

i j	Bond length $r_{0,ij}$ [nm]	Force constant k_{ij} [kJ nm^{-2} mol^{-1}]	*i j k*	Bond angle $\theta_{0,ij}$ [°]	Force constant k_{ijk} [kJ nm^{-2} mol^{-1}]
G1 G1	0.350*	200*	G1 G1 G1	127*	25*
D1 D1	0.350*	200*	D1 D1 D1	127*	25*
N1 N1	0.350*	200*	N1 N1 N1	127*	25*

GG-PTX Sidechain Topology

i j	Bond length $r_{0,ij}$ [nm]	Force constant k_{ij} [kJ nm^{-2} mol^{-1}]	*i j k*	Bond angle $\theta_{0,ij}$ [°]	Force constant k_{ijk} [kJ nm^{-2} mol^{-1}]
D1 D2	0.37	7500*	D1 D2 D3	153	100*
D2 D3	0.39	7500*	D2 D3 D4	94	100*
D3 D4	0.41	7500*	D3 D4 D5	130	100*
D4 D5	0.36	7500*	D4 D5 D6	84	100*
D5 D6	0.26	7500*	D4 D5 D13	146	100*
D6 D7	0.35	7500*	D5 D6 D7	107	100*
D6 D10	0.32	7500*	D5 D6 D10	75	100*
D5 D13	0.20	7500*	D5 D13 D14	80	100*
D13 D14	0.23	7500*	D5 D13 D23	158	100*
D7 D8	0.27*	1000*	D6 D7 D8	173	100*
D7 D9	0.27*	1000*	D6 D7 D9	109	100*
D8 D9	0.27*	1000*	D6 D10 D11	143	100*
D10 D11	0.27*	1000*	D6 D10 D12	105	100*
D10 D12	0.27*	1000*	D13 D14 D22	95	100*
D11 D12	0.27*	1000*	D13 D14 D15	127	100*
D13 D23	0.22	7500*	D13 D22 D24	85	100*
D14 D23	0.34	7500*	D14 D23 D22	60	100*
D14 D15	0.38	7500*	D14 D15 D16	52	100*
D15 D16	0.52	7500*	D14 D15 D17	36	100*
D15 D17	0.61	7500*	D15 D17 D22	53	100*
D17 D18	0.58	7500*	D15 D17 D18	85	100*
D18 D19	0.29	7500*	D15 D17 D19	48	100*
D17 D19	0.47	7500*	D16 D17 D24	31	100*
D17 D22	0.14	7500*	D17 D19 D21	120	100*
D19 D20	0.35	7500*	D18 D19 D20	115	100*
D19 D21	0.25	7500*	D18 D19 D21	121	100*
D22 D24	0.37	7500*	D18 D17 D19	30	100*
D22 D23	0.37	7500*	D22 D18 D19	54	100*
D24 D25	0.24	7500*	D22 D19 D20	105	100*
D25 D26	0.27*	1000*	D22 D24 D25	125	100*
D25 D27	0.27*	1000*	D23 D22 D13	75	100*
D26 D27	0.27*	1000*	D23 D22 D24	96	100*
			D24 D25 D26	128	100*
			D24 D25 D27	165	100*

*Taken from the predetermined values for backbone or sidechain bonded parameters from the MARTINI force field.

Table 5.5. Coarse-grained topologies for PEG1000-npRGD					
i j	**Bond length $r_{0,ij}$ [nm]**	**Force constant k_{ij} [kJ nm^{-2} mol^{-1}]**	***i j k***	**Bond angle $\theta_{0,ij}$ [º]**	**Force constant k_{ijk} [kJ nm^{-2} mol^{-1}]**
N1 N2	0.41	7500*	N1 N2 N3	133	100*
N2 N3	0.39	7500*	N2 N3 N4	82	100*
N3 N4	0.82	7500*	N6 N5 N7	87	100*
N5 N6	0.34	7500*	N7 N8 N9	170	100*
N5 N7	0.37	7500*	N8 N9 N10	60	100*
N7 N8	0.32	7500*	N9 N10 N8	60	100*
N8 N9	0.27*	7500*	N9 N8 N10	60	100*
N9 N10	0.27*	7500*	N9 N11 N12	133	100*
N8 N10	0.27*	7500*	N12 N13 N14	60	100*
N9 N11	0.30	7500*	N13 N14 N12	59	100*
N11 N12	0.32	7500*	N3 N4 N15	130	100*
N12 N13	0.21	7500*	N4 N15 N16	131	100*
N13 N14	0.22	7500*	N15 N16 N17	133	100*
N12 N14	0.21	7500*	N16 N17 N18	133	100*
N4 N15	0.39	7500*	N17 N18 N19	125	100*
N15 N16	0.35	7500*	N18 N19 N20	127	100*
N16 N17	0.34	7500*	N19 N20 N21	126	100*
N17 N18	0.45	7500*	N20 N21 N22	120	100*
N18 N19	0.35	7500*	N21 N22 N23	126	100*
N19 N20	0.33	7500*	N22 N23 N24	124	100*
N20 N21	0.45	7500*	N23 N24 N25	119	100*
N21 N22	0.35	7500*	N24 N25 N26	125	100*
N22 N23	0.33	7500*	N25 N26 N27	120	100*
N23 N24	0.44	7500*	N26 N27 N28	119	100*
N24 N25	0.35	7500*	N27 N28 N29	126	100*
N25 N26	0.33	7500*	N28 N29 N30	133	100*
N26 N27	0.44	7500*	N29 N30 N5	127	100*
N27 N28	0.35	7500*			
N28 N29	0.30	7500*			
N29 N30	0.30	7500*			
N30 N5	0.40	7500*			

*Taken from the predetermined values for backbone or sidechain bonded parameters from the MARTINI force field.

Table 5.6. Coarse-grained topologies for PEG2000-npRGD					
i j	**Bond length $r_{0,ij}$ [nm]**	**Force constant k_{ij} [kJ nm^{-2} mol^{-1}]**	***i j k***	**Bond angle $\theta_{0,ij}$ [º]**	**Force constant k_{ijk} [kJ nm^{-2} mol^{-1}]**
N1 N2	0.37	7500*	N1 N2 N3	134	100*
N2 N3	0.39	7500*	N2 N3 N4	85	100*
1N3 N4	0.39	7500*	N6 N5 N7	91	100*
N5 N6	0.35	7500*	N7 N8 N9	171	100*
N5 N7	0.36	7500*	N8 N9 N10	60	100*
N7 N8	0.31	7500*	N9 N10 N8	60	100*
N8 N9	0.27*	7500*	N9 N8 N10	60	100*
N9 N10	0.27*	7500*	N9 N11 N12	134	100*
N8 N10	0.27*	7500*	N12 N13 N14	60	100*
N9 N11	0.30	7500*	N13 N14 N12	60	100*
N11 N12	0.32	7500*	N3 N4 N15	132	100*
N12 N13	0.21	7500*	N4 N15 N16	128	100*
N13 N14	0.22	7500*	N15 N16 N17	133	100*
N12 N14	0.21	7500*	N16 N17 N18	128	100*
N4 N15	0.40	7500*	N17 N18 N19	133	100*
N15 N16	0.36	7500*	N18 N19 N20	128	100*
N16 N17	0.34	7500*	N19 N20 N21	120	100*
N17 N18	0.46	7500*	N20 N21 N22	122	100*
N18 N19	0.35	7500*	N21 N22 N23	127	100*
N19 N20	0.34	7500*	N22 N23 N24	127	100*
N20 N21	0.45	7500*	N23 N24 N25	121	100*
N21 N22	0.36	7500*	N24 N25 N26	127	100*
N22 N23	0.33	7500*	N25 N26 N27	126	100*
N23 N24	0.44	7500*	N26 N27 N28	122	100*
N24 N25	0.35	7500*	N27 N28 N29	131	100*
N25 N26	0.33	7500*	N28 N29 N30	126	100*
N26 N27	0.44	7500*	N29 N30 N31	121	100*
N27 N28	0.35	7500*	N30 N31 N32	128	100*
N28 N29	0.33	7500*	N31 N32 N33	123	100*
N29 N30	0.45	7500*	N32 N33 N34	122	100*
N30 N31	0.35	7500*	N33 N34 N35	125	100*
N31 N32	0.39	7500*	N34 N35 N36	125	100*
N32 N33	0.45	7500*	N35 N36 N37	121	100*
N33 N34	0.35	7500*	N36 N37 N38	119	100*
N34 N35	0.33	7500*	N37 N38 N39	126	100*
N35 N36	0.45	7500*	N38 N39 N40	121	100*
N36 N37	0.37	7500*	N39 N40 N41	127	100*
N37 N38	0.33	7500*	N40 N41 N42	114	100*
N38 N39	0.45	7500*	N41 N42 N44	121	100*
N39 N40	0.35	7500*	N42 N43 N44	120	100*
N40 N41	0.33	7500*	N43 N44 N45	126	100*
N41 N42	0.44	7500*	N44 N45 N46	120	100*
N42 N43	0.45	7500*	N45 N46 N47	124	100*
N43 N44	0.33	7500*	N46 N47 N5	120	100*
N44 N45	0.45	7500*			
N45 N46	0.12	7500*			
N46 N47	0.12	7500*			
N47 N5	0.40	7500*			

*Taken from the predetermined values for backbone or sidechain bonded parameters from the MARTINI force field.

Table 5.7. Solvent-accessible surface area of PGG-PTX-PEG-npRGD molecules

System	$SASA_{PGG}$ (nm^2)	$SASA_{PEG}$ (nm^2)	$SASA_{PTX}$ (nm^2)	$SASA_{npRGD}$ (nm^2)
PEG500				
4 nonpeptide RGD				
A	257.2	3.6	59.6	7.2
B	265.0	7.3	97.9	11.2
8 nonpeptide RGD				
A	257.7	5.2	70.3	12.6
B	253.7	5.7	77.9	18.5
12 nonpeptide RGD	264.5	9.0	62.4	26.8
16 nonpeptide RGD				
A	247.9	12.2	61.4	34.8
B	247.9	23.6	90.9	45.1
PEG1000				
4 nonpeptide RGD				
A	262.1	1.2	85.4	4.3
B	298.6	4.2	89.1	7.0
8 nonpeptide RGD				
A	255.3	8.4	79.8	10.8
B	264.2	23.6	102.8	17.6
C	251.0	7.0	57.9	11.8
12 nonpeptide RGD				
A	266.0	1.7	53.1	20.3
B	289.8	1.7	73.9	30.6
C	285.4	1.7	72.7	26.6
16 nonpeptide RGD	297.7	2.5	64.3	37.1
PEG2000				
4 nonpeptide RGD	269.5	6.3	60.9	51.1
8 nonpeptide RGD	243.9	23.3	61.0	13.7
12 nonpeptide RGD	229.6	29.9	59.7	22.6
16 nonpeptide RGD	206.1	49.8	49.1	37.8

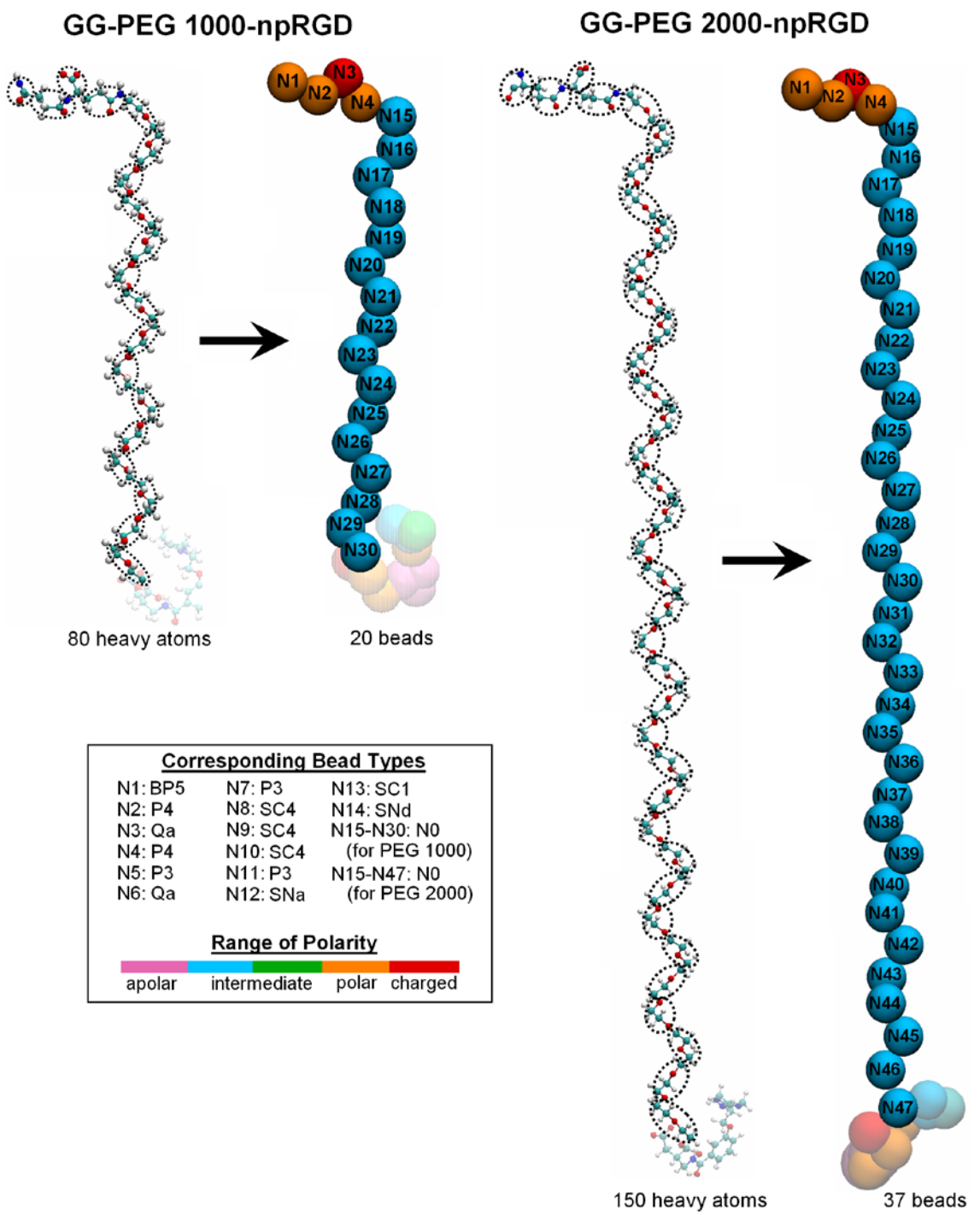

Figure 5.7. Coarse-grained representations of GG-PEG1000-npRGD and GG-PEG2000-npRGD residues. Mappings of the group of N8, N9, N10, N11, N12, N13, N14 beads and group of N5, N6, and N7 beads are identical to those of the GG-PEG500-npRGD residue in Fig. 3. Overall, the GG-PEG1000-npRGD residue was reduced from 80 heavy atoms to 20 beads, and the GG-PEG2000-npRGD residue was reduced from 150 heavy atoms to 37 beads.

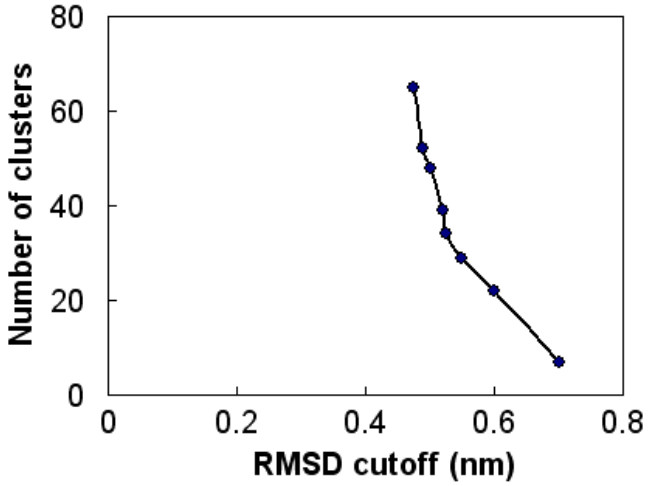

Figure 5.8. Sample relationship between the RMSD cutoff length vs. number of clusters for a PGG-PTX-PEG-npRGD molecule. Shows the data for a PGG-PTX-PEG1000-npRGD$_{12}$ molecule. Trial-and-error using the GROMACS 4.0.3 *g_cluster* module was used to determine the optimal RMSD cutoff length, which usually corresponds to ~40 clusters. For this molecule, the RMSD cutoff length was determined to be 0.52 nm, which corresponds to 39 clusters.

This chapter, in part, is currently being prepared for submission for publication of the material. Peng LX, Chaudhari AS, Das SK, Yu L, Howell SB, Gough DA. The dissertation author was the primary investigator and first author of this paper.

Chapter 6

Conclusions and Future Directions

6.1 Conclusions

The focus on this thesis was to elucidate these properties of semiflexible polymeric anticancer therapeutics, PGG-PTX, and PGG-PTX-PEG-npRGD. The computational modeling of PGG-PTX was based on the hypothesis that the relative amount of PTX (f_{PTX} = 0.18, 0.24, and 0.37) and spatial arrangement of PTX on the hydrophilic PGG polymer (uniform: 'even' and 'random', clustered: 'clusters' and 'ends', concentrated: 'middle' and 'side') concomitantly influences the size, shape, flexibility, surface hydrophilicity, and aggregation of PGG-PTX. The computational modeling of PGG-PTX-PEG-npRGD systems was based on the hypothesis that the PEG spacer length (500 Da, 1000 Da, and 2000 Da) and density of npRGD ligands (4, 8, 12, and 16 per PGG-PTX-PEG-npRGD molecule) together influences the size, shape, and flexibility of each PGG-PTX-PEG-npRGD molecule.

At the commencement of this study, our main hurdle was to develop a molecular modeling methodology to elucidate the physicochemical behavior of semiflexible biomolecules. Molecular modeling approaches had previously been rigorously applied to rigid systems such as proteins and nucleic acids, but a methodology for predicting

behavior of semiflexible systems had yet to be developed, which were one of the objectives in this thesis. Furthermore, in an ideal world of infinite computing resources, all solute and solvent atoms in small molecular systems have often been considered as discrete entities. For large molecular systems like those studied here, the level of computing resources and time required would be extraordinary and impractical, given the relatively large sizes of the PGG-PTX and PGG-PTX-PEG-npRGD molecules. Therefore, in order to study the size, shape, flexibility, and other properties of PGG-PTX and PGG-PTX-PEG-npRGD, the scale was adjusted from the atomistic level to the atomistic group level in the modeling methodology.

Molecular dynamics (MD) simulations of biomolecules usually begin with a starting structure whose information is based on X-ray crystallography and/or NMR spectroscopy experiments. Since no such information about PGG-PTX and PGG-PTX-PEG-npRGD was available, circular dichroism spectroscopy was used to determine their starting structures. The CD spectroscopy results showed that PGG-PTX and PGG-PTX-PEG-npRGD exist as random coils and lack secondary structure. Hence, the starting structure can be initiated from any conformation.

In conventional MD simulations of solute-water systems, water molecules are characterized as explicit structures modeled using an atom-based molecular force field. Such MD simulations involve interactions among a large number of atoms, most of which belong to solvent molecules. Given the large sizes of the PGG-PTX and PGG-PTX-PEG-npRGD systems, and to reduce the CPU time required for all-atom (AA) simulations, a Generalized-Born implicit solvent model was used. AA MD simulations were carried out in AMBER 9.0 on all PGG-PTX and PGG-PTX-PEG-npRGD systems

until statistical equilibria were reached at 100 ns, and the equilibrium bonded distances and angles were extracted using the Boltzmann inversion as parameters for the coarse-grained (CG) models. AA models were converted to CG models using mapping scheme dictated by the MARTINI force field. Subsequent CG MD simulations on the PGG-PTX and PGG-PTX-PEG-npRGD systems were run in GROMACS 4.0.3 until statistical equilibrium, a point where there were minimal differences in structural fluctuations within the overall molecule.

The first modeling study of PGG-PTX molecules, as described in Chapter 2, good reproducibility was demonstrated between the AA and CG models, proving that the CG models are robust enough for predicting the structural behavior of PGG-PTX. Each PGG-PTX molecule was solvated in explicit water of 2 nm thickness; CG MD simulations were run for an effective time of 800 ns, which led to statistical equilibrium; and the final structure at this point was representative structure. The results show that most PGG-PTX molecules adopt coil morphologies, and the PGG-PTX molecules at f_{PTX} = 0.24 are most susceptible to morphological change. The results also show that the size and flexibility of PGG-PTX are not significantly affected by PTX loading fraction and spatial PTX arrangement.

While this method was acceptable in characterizing conformations of PGG-PTX, there were steps in the methodology that raised concerns. The following changes in the modeling methodology were made: 1) the simulation box size was increased to $(20\ nm)^3$ in effort to avoid overlap between the PGG-PTX molecules; 2) RMSD clustering was used to determine the characteristic conformations; and 3) the MD simulation time was extended to 4 μs. The resulting PGG-PTX conformations were considerably different

from those determined in the original method. The PGG-PTX molecules with uniform spatial PTX arrangements produced globular shapes, whereas the molecules with concentrated spatial PTX arrangements generated filamentous morphologies. The clustered PTX arrangements resulted in PGG-PTX molecules with both globular and filamentous morphologies. The size and flexibility of the PGG-PTX systems were mildly affected by the PTX loading fraction and spatial PTX arrangements. Given the potential beneficial implications of nonspherical particle shape in adhesion to walls of tumor endothelia, PGG-PTX molecules with concentrated spatial PTX arrangements are expected to be the most promising candidates.

The intermolecular behavior of PGG-PTX was examined in Chapter 4. Simultaneously, CG MD simulations of five identical PGG-PTX molecules were run in GROMACS 4.0.3 until statistical equilibrium was attained at 12 μs, and RMSD clustering was used to determine the characteristic conformations. Results indicate that PGG-PTX is the least stable at f_{PTX} = 0.37, since those systems exhibit the highest degrees of aggregation. Also, at f_{PTX} = 0.18 and 0.24, the PGG-PTX molecules with concentrated spatial PTX arrangements (‘ends’, ‘middle’, and ‘side’) are filamentous, while the molecules with dispersed spatial PTX arrangements (‘even’, ‘random’, and ‘clusters’) are globular. This behavior indicates that each individual PGG-PTX molecule maintains its shape (as described in Chapter 2 and 3) in the presence of other molecules, but only if the molecules do not aggregate. Finally, we showed that the f_{PTX} = 0.18 systems have the highest surface hydrophilicity, and the f_{PTX} = 0.37 systems are the least flexible.

The objective of the modeling study in Chapter 4 was to identify the PGG-PTX compound(s) with the potential to overcome biological barriers in drug delivery. Based on the implications of shape, flexibility, surface hydrophilicity, and aggregation, the ideal PGG-PTX candidate would possess nonspherical morphology, high surface hydrophilicity, high flexibility, and low aggregation. The results show that the PGG-PTX molecules at f_{PTX} = 0.24 with concentrated spatial PTX arrangements ('middle' and 'side') fit the aforementioned criteria and thus are the most promising candidates. Therefore, we recommend the PGG-PTX systems at f_{PTX} = 0.24 with the 'middle' and 'side' PTX distributions for future experimental testing.

Aside from the PGG-PTX compounds, the shape, flexibility, and surface hydrophilicity of PGG-PTX-PEG-npRGD (f_{PTX} = 0.37) molecules varying in PEG molecular weight (500 Da, 1000 Da, and 2000 Da) and nonpeptide RGD ligand density (4, 8, 12, and 16 per PGG-PTX-PEG-npRGD molecule) were studied in Chapter 5. We determined that the PEG2000 molecules always produced globular shapes and were more rigid, whereas the PEG500 and PEG1000 molecules generated globular and filamentous shapes and were more flexible. Higher PEG molecular weight and lower density of nonpeptide RGD resulted in higher degrees of surface hydrophilicity. Overall, the results suggest that the PGG-PTX-PEG1000-npRGD$_8$ and PGG-PTX-PEG1000-npRGD$_{12}$ molecules are the most efficacious for their nonspherical, filamentous shape, high flexibility, and high surface hydrophilicity.

6.2 Future Directions

Computer simulations have been used to elucidate certain structural and functional properties of semiflexible polymeric drug delivery systems. The next step is to investigate how the drug particles interact with their biological and physiological environments. Molecular transport processes such as avoidance of opsonin deposition (to avoid further RES clearance) in the bloodstream and cellular uptake of the drug via macropinocytosis or receptor-mediated endocytosis are just a few of the physiological barriers that may hinder the access of a drug to its tumor target. It would be useful to use computer simulations to examine these dynamic processes in detail, especially since they can be tedious to study on the molecular level using wet-lab experiments. In addition, it would be interesting to examine whether the structural and functional properties of PGG-PTX differ in environments varying in pH; the pH of the extracellular tumor interstitium and intracellular tumor space are approximately 6.2 and 4.2, respectively. Constant pH MD simulations of biomolecules in implicit solvent established by Charles Brooks can be applied towards this study. This theoretical approach would be useful to help design *in vitro* and *in vivo* experiments in preclinical development.

APPENDIX A

Molecular dynamics simulations files

A.1 All-atom molecular dynamics simulations

All AA MD simulations of PGG-PTX and PGG-PTX-PEG-npRGD systems were carried out in AMBER 9.0. Exact input commands and input files for the energy minimization and MD simulation are provided below.

A.1.1 System minimization

Each molecule was minimized in implicit solvent using the following `min.in` file. The *sander* modules were used for this step.

```
&cntrl

  timlim = 999999., nmropt = 0,
  ntx    = 1,       irest  = 0,       ntrx   = 1,      ntxo   = 1,
  ntpr   = 100,     ntwx   = 100,       ntwv   = 0,      ntwe   = 0,
  ioutfm = 0,       ntwr   = 500,
  ntwprt = 0,

  imin=1, ntmin=1, nmropt=0, drms=0.1
  maxcyc=2000, ncyc=250,

  ntf    = 1,       ntb    = 0,
  igb  = 2,         gbsa    = 1,   surften=0.005,     dielc  = 1.0,
  cut    = 16.0,     nsnb   = 10,
  scnb   = 2.0,     scee   = 1.2,
  saltcon=0.14,
  ntc    = 1,       tol    = 0.00001, jfastw = 0,

&end
```

A.1.2 Running MD simulations

MD simulations were run in *sander* module using the `md.in` file:

```
&cntrl

  timlim = 999999., nmropt = 0,       imin=0,
  ntx    = 1,       irest  = 0,       ntrx   = 1,      ntxo   = 1,
  ntpr   = 100,      ntwx   = 100,       ntwv   = 0,      ntwe   = 0,
  ioutfm = 0,       ntwr   = 50000,
  ntwprt = 0,

  ntf    = 2,       ntb    = 0,
  igb  = 2,         gbsa    =1,   surften=0.005,     dielc  = 1.0,
  cut    = 16.0,     nsnb   = 10,
  scnb   = 2.0,     scee   = 1.2, saltcon=0.14

  nstlim = 100000,   nscm   = 2500,   iwrap = 0, t  = 0.0,     dt     =
  0.002,

  temp0  = 300.0,   tempi  = 200.0,    tautp=0.5,      ig  = 71227,
  heat   = 0.0,     ntt    = 3,      gamma_ln=2.0,
  ntc    = 2,       tol    = 0.00001, jfastw = 0,

  ibelly=0, ntr=0,

$end
```

To restart the MD simulation after the first MD run, the following `md_rst.in` file was used:

```
&cntrl

timlim = 999999., nmropt = 0,       imin=0,
ntx    = 5,       irest  = 1,       ntrx   = 1,      ntxo   = 1,
ntpr   = 100,      ntwx   = 100,       ntwv   = 0,     ntwe   = 0,
ioutfm = 0,       ntwr   = 50000,
ntwprt = 0,

ntf    = 2,       ntb    = 0,
igb  = 2,         gbsa    =1,   surften=0.005,     dielc  = 1.0,
cut    = 16.0,     nsnb   = 10,
scnb   = 2.0,     scee   = 1.2, saltcon=0.14

nstlim = 1000000,   nscm   = 2500,   iwrap = 0,
t      = 0.0,     dt     = 0.002,

temp0  = 300.0,   tempi  = 200.0,    tautp=0.5,      ig  = 71227,
heat   = 0.0,     ntt    = 3,      gamma_ln=2.0,
ntc    = 2,       tol    = 0.00001, jfastw = 0,

ibelly=0, ntr=0,

&end
```

A.2 Coarse-grained molecular dynamics simulations

All CG MD simulations of PGG-PTX and PGG-PTX-PEG-npRGD systems were carried out in GROMACS 4.0.3 Exact input commands and input files for the energy minimization and MD simulation are provided below.

A.2.1 Energy minimization

Each molecule was minimized in explicit solvent using the `em.mdp` file. The *grompp* and *mdrun* modules were used for this step.

```
; VARIOUS PREPROCESSING OPTIONS =
title                    =
cpp                      = /lib/cpp
include                  =
define                   =

; RUN CONTROL PARAMETERS =
integrator               = steep
; start time and timestep in ps =
tinit                    = 0
dt                       = 0.02
nsteps                   = 300

; ENERGY MINIMIZATION OPTIONS =
;emtol                    = 0.00001
;emstep                   = 0.1
;nstcgsteep               = 1000

emtol                    = 10
emstep                   = 0.01
nstcgsteep               = 1000
```

A.2.2 Running MD simulations in GROMACS 4.0.3

MD simulations were using the `md.mdp` file:

```
; STANDARD MD INPUT OPTIONS FOR MARTINI 2.0 for use with GROMACS 4.0.3

; VARIOUS PREPROCESSING OPTIONS =
title                    = Martini
cpp                      = /usr/bin/cpp

; RUN CONTROL PARAMETERS =
; MARTINI - Most simulations are stable with dt=40 fs, some (especially
; rings) require 20-30 fs. The range of time steps used for
; parametrization is 20-40 fs, using smaller time steps is therefore not
; recommended.

integrator               = md
; start time and timestep in ps
tinit                    = 0
dt                       = 0.040
;nsteps                   = 10000 ; initial step
nsteps                          = 2500000 ; 100 ns @ dt=0.04

; number of steps for center of mass motion removal =
nstcomm                  = 1

; OUTPUT CONTROL OPTIONS =
; Output frequency for coords (x), velocities (v) and forces (f) =
nstxout                  = 5000
nstvout                  = 5000
nstfout                  = 0
; Output frequency for energies to log file and energy file =
nstlog                   = 1000
nstenergy                = 100
; Output frequency and precision for xtc file =
nstxtcout                = 5000 ; frame every 150 ps
xtc_precision            = 100
; This selects the subset of atoms for the xtc file. You can select
; multiple groups. By default all atoms will be written. =
xtc-grps                 =
; Selection of energy groups =
energygrps               = PROTEIN W ION

; NEIGHBORSEARCHING PARAMETERS =
; MARTINI - no need for more frequent updates or larger neighborlist cut-
; off due to the use of shifted potential energy functions.

; nblist update frequency =
nstlist                  = 10
; ns algorithm (simple or grid) =
ns_type                  = grid
; Periodic boundary conditions: xyz or none =
pbc                      = xyz
; nblist cut-off         =
rlist                    = 1.2

; OPTIONS FOR ELECTROSTATICS AND VDW =
; MARTINI - vdw and electrostatic interactions are used in their shifted
; forms. Changing to other types of electrostatics will affect the
; general performance of the model.
```

```
; Method for doing electrostatics =
coulombtype              = Shift
rcoulomb_switch          = 0.0

rcoulomb                 = 1.2


; Dielectric constant (DC) for cut-off or DC of reaction field =
epsilon_r                = 15
; Method for doing Van der Waals =
vdw_type                 = Shift
; cut-off lengths        =
rvdw_switch              = 0.9
rvdw                     = 1.2
; Apply long range dispersion corrections for Energy and Pressure =
DispCorr                 = No

; OPTIONS FOR WEAK COUPLING ALGORITHMS =
; MARTINI - normal temperature and pressure coupling schemes can be used.
; Recommended to couple individual groups in your system seperately.

; Temperature coupling   =
tcoupl                   = Berendsen
; Groups to couple separately =
tc-grps                  = PROTEIN SOLVENT
; Time constant (ps) and reference temperature (K) =
tau_t                    = 1.0 1.0
ref_t                    = 310 310
; Pressure coupling      =
Pcoupl                   = berendsen
Pcoupltype               = isotropic
; Time constant (ps), compressibility (1/bar) and reference P (bar) =
tau_p                    = 5.0
compressibility          = 4.5e-5
ref_p                    = 1.0

; GENERATE VELOCITIES FOR STARTUP RUN =
gen_vel                  = yes
gen_temp                 = 310
gen_seed                 = 1

; OPTIONS FOR BONDS     =
; MARTINI - for ring systems constraints are defined which are best
; handled using Lincs.
constraints              = none
; Type of constraint algorithm =
constraint_algorithm     = Lincs
; Do not constrain the start configuration =
unconstrained_start      = no
; Highest order in the expansion of the constraint coupling matrix =
lincs_order              = 4
; Lincs will write a warning to the stderr if in one step a bond =
; rotates over more degrees than =
lincs_warnangle          = 30
```

A.3 Sample submission scripts

A.3.1 Submission script for AMBER 9.0

Written in C-shell:

```
#!/bin/csh
#$ -S /bin/csh
#$ -cwd
#
#$ -M lpeng@ucsd.edu
#$ -l h_rt=96:00:00
#$ -V
#$ -e error_file
#$ -o output_file
#$ -pe mpi 8

echo Running on host `hostname`
echo Time is `date`
echo Directory is `pwd`
cp $TMPDIR/machines machinefile

setenv LD_LIBRARY_PATH /home/swong/intel/mkl/9.1/lib/em64t/

cd /gpfs/lpeng/nexil12/random

/opt/mpich/myrinet/intel/bin/mpirun -np $NSLOTS -machinefile
$TMPDIR/machines /home/swong/usr/amber9_mkl/exe/sander.MPI -O \
       -i md_rst.in \
       -o nexil12_random_4.out \
       -p nexil12_random.top \
       -c nexil12_random_3.rst \
       -r nexil12_random_4.rst \
       -x nexil12_random_4.mdcrd
```

A.3.2 Submission script for GROMACS 4.0.3

Written in Bash shell:

```
#!/bin/bash
#$ -cwd
#$ -S /bin/bash
#$ -e error_file
#$ -o output_file
#
# requesting 16 processors
#$ -pe mpich 16
# requesting 168 hours of wall.clock time
#$ -l h_rt=168:00:00

echo Running on host `hostname`
echo Time is `date`
echo Directory is `pwd`
echo This job runs on the following processors:
cat $TMPDIR/machines

# Write node IDs to file
cp $TMPDIR/machines node1

# Define locations of MDRUN, TPBCONV and MPIRUN
export MDRUN=/home/pwhitfor/BIN/gromacs-4.0.3/bin/mdrun
export TPBCONV=/home/pwhitfor/BIN/gromacs-4.0.3/bin/tpbconv
export MPIRUN=/soft/linux/pkg/mpich/intel/bin/mpirun

# Running Gromacs: read TPR and write output to /gpfs disk
$MPIRUN -machinefile $TMPDIR/machines -np $NSLOTS $MDRUN -v -nice 0 -np
$NSLOTS \
       -s n12_random_all.tpr \
      -o n12_random_all_2.trr \
      -c n12_random_all.gro \
      -x n12_random_all.xtc

# MDRUN completes: now make the next run file for a further 268 ps, to be
run by next job
$TPBCONV \
       -s n12_random_all.tpr \
       -f n12_random_all.trr \
       -o n12_random_all_2.tpr \
       -extend 200000

# Now delete the TRR file to conserve disk space
rm n12_random_all.trr
```

A.4 Boltzmann inversion script in MATLAB 7.0

```
load angle_all_46_47_5.out2;
t = angle_all_46_47_5(:,1);
angle_all_46_47_5 = angle_all_46_47_5(:,2);

% Generates the probability distribution
P = hist(angle_all_46_47_5,200);
size(P);
sum(P);

% Normalized probability distribution
delta = (max(angle_all_46_47_5) - min(angle_all_46_47_5))/200;
A = 1./(delta.*sum(P));
%A.*sum(P).*delta;
G = A.*P;           % G = normalized probability distribution
size(G);

for i=1:200;
    x(i) = min(angle_all_46_47_5) + delta.*i;    % generates 200 values
of x to plot against 200 values of G
end

% Potential of mean force
W = -0.616.*log(G);        % W = potential of mean force
%
cftool(x,W)
```

Bibliography

1. Ferrari, M. Cancer nanotechnology: opportunities and challenges. *Nat Rev* 5, 161-171 (2005).

2. Ferrari, M. Beyond drug delivery. *Nat Nano* 3, 131-132 (2008).

3. Geng, Y., Dalhaimer, P., Cai, S., Tsai, R., Tewari, M., Minko, T., Discher, D. E. Shape effects of filaments versus spherical particles in flow and drug delivery. *Nature Nanotech* 2, 249-255 (2007).

4. Srinivas, G., Shelley, J. C., Nielson, S. O., Discher, D. E., Klein, M. L. *J Phys Chem B* 108, 8150-8160 (2004).

5. Decuzzi, P., Pasqualini, R., Arap, W., Ferrari, M. *Pharma Res* 26, 235-243 (2008).

6. Duncan, R. The dawning era of polymer therapeutics. *Nat Rev Drug Discov* 2, 347-360 (2003).

7. Nishiyama, N. Nanocarriers shape up for long life. *Nat Nano* 2, 203-204 (2007).

8. Jiang, W., Kim, B. Y., Rutka, J. T., Chan, W Nanoparticle-mediated cellular response is size-dependent. *Nat Nano* 3, 145-150 (2008).

9. Champion, J.A., Katare, Y. K., Mitragotri, S. Particle shape: a new design for micro- and nanoscale drug delivery carriers. *J Control Release* 121, 3-9 (2007).

10. Champion, J.A., Mitragotri, S Role of target geometry in phagocytosis. *PNAS* 103, 4930-4934 (2006).

11. Satchi-Fainaro, R., Duncan, R. Polymer Therapeutics I, Vol. 1. (Springer, New York; 2006).

12. Pujol, J.L. in Clinical Study Report for Study CA139-368 (Bristol-Myers Squibb, Montpellier, France; 2005).

13. Piccart, M.J., Bertelsen, K., James, K., Cassidy, J., Mangioni, C., Simonsen, E., Stuart, G., Kaye, S., Vergote, I., Blom, R., Grimshaw, R., Atkinson, R. J., Swenerton, K. D., Trope, C., Nardi, M., Kaern, J., Tumolo, S., Timmers, P., Roy, J. A., Lhoas, F., Lindvall, B., Bacon, M., Birt, A., Andersen, J. E., Zee, B., Paul, J., Baron, B., Pecorelli, S. *J Natl Cancer Inst* 92, 699-708 (2000).

14. Yoshida, T. in Clinical Study Report for Study CA139-387 (Bristol-Myers Squibb Tokyo, Japan; 2009).

15. Wang, X., Gang, Z., Van, S., Yu, L., Vol. US20090226393. (ed. N.D.T. Corporation) 1-27 (Nitto Denko Technical Corporation, USA; 2009).

16. Abraxis. (ed. A. Oncology) 1-26 (Abraxis Bioscience, USA; 2007).

17. Vauthier, C., Fattal, E., Labarre, D. in Chapter 26: From Polymer Chemistry and Physicochemistry to Nanoparticulate Drug Carrier Design and Applications, Vol. 1.12003).

18. Schames, J., Henchman, R. H., Siegel, J. S., Sotriffer, C. A., Ni, H., McCammon, J. A. Discovery of a novel binding trench in HIV integrase. *J Med Chem* 47, 1879-1881 (2004).

19. Amaro, R.E., Schnaufer, A., Interthal, H., Hol, W., Stuart, W. D., McCammon J. A. Discovery of drug-like inhibitors of an essential RNA-editgin ligase in trypanosoma brucei. *PNAS* 106, 17278-17283 (2008).

20. Zewail, A.H. in Physical Biology: From Atoms to Medicine. (ed. A.H. Zewail) 401-410 (World Scientific Publishing, 2008).

21. Baschnagel, J., Binder, K., Doruker, P., Gusev, A. A., Hahn, O., Kremer, K., Mattice, W. L., Muller-Plathe, F., Murat, M., Paul, W., Santos, S., Suter, U. W., Tries, V. *Advances in Polymer Science* 152, 41-156 (2000).

22. Beall, G.W., Muruesan, S., Galloway, H. C., Koeck, D. C., Jarl, J., Abrego, F. *Polymer* 46, 11889-11895 (2005).

23. Faller, R. *Polymer* 45, 3869-3876 (2004).

24. Greenfield, N.J. Using circular dichroism spectroscopy spectra to estimate protein secondary structure. *Nat Protoc* 1, 2876-2890 (2007).

25. Cooke, B., Schmidler, S. C. *Biophys J* 95, 4497-4511 (2008).

26. Adcock, S.A., McCammon, J. A. Molecular dynamics: a survey of methods for simulating the activity of proteins. *Chem Rev* 106, 1589-1615 (2006).

27. Muller-Plathe, F. *Chem Phys Chem Rev* 3, 754-769 (2002).

28. Kenward, M., Dorfman, K. D. *Biophys J* 97, 2785-2793 (2009).

29. Case, D.A., Cheatham, T. E., Darden, T., Gohlke, H., Luo, R., Merz, K. M., Jr., Onufriev, A., Simmerling, C., Wang, B., Woods, R. The AMBER biomolecular simulation programs. *J Comput Chem* 26, 1668-1688 (2005).

30. Cornell, W.D., Cieplak, P., Bayly, C. I., Gould, I. R., Merz, K. M., Jr., Ferguson, D. M., Spellmeyer, D. C., Fox, T., Caldwell, J. W., Kollman, P. A. *J Am Chem Soc* 117, 5179-5197 (1995).

31. Wang, J., Rolf, R. M., Caldwell, J. W., Kollman, P. A., Case, D. A. *J Comput Chem* 25, 1157-1174 (2004).

32. Monticelli, L., Kandasamy, S. K., Periole, X., Larson, R. G., Tieleman, D. P., Marrink, S. J. The MARTINI coarse-grained force field: extension to proteins. *J Chem Theory and Comput* 4, 819-834 (2008).

33. Lindahl, E., Hess, B., van der Spoel, D. GROMACS 3.0: A package for molecular simulation and trajectory analysis. *J Mol Mod* 7, 306-317 (2001).

34. Bernstein, F.C., Koetzle, T. F., Williams, G. J., Meyer, E. E., Jr., Brice, M. D., Rodges, J. R., Kennard, O., Shimanouchi, T., Tasumi, M. *J of Mol Biol* 112, 535 (1977).

35. Frisch, M.J.T., G. W., Schlegel, H. B., Gill, P. M. W., Johnson, B. G., Robb, M. A., Cheeseman, J. R., Keith, T. A., Petersson, G. A., Montgomery, J. A., Raghavachari, K., Al-Laham, M. A., Zakrzewski, V. G., Ortiz, J. V., Foresman, J. B., Cioslowski, J., Stefanov, B. B., Nanayakkara, A., Challacombe, M., Peng, C. Y., Ayala, P. Y., Chen, W., Wong, M. W., Andres, J. L., Replogle, E. S., Gomperts, R., Martin, R. L., Fox, D. J., Binkley, J. S., Defrees, D. J., Baker, J., Stewart, J. P., Head-Gordon, M., Gonzalez, C., Pople, J. A. (Gaussian, Inc., Pittsburgh, PA; 1995).

36. Cornell, W.D., Cieplak, C., Bayly, C. I., Kollman, P. A. *J Am Chem Soc* 115, 9620-9631 (1993).

37. Onufriev, A., Bashford, D., Case, D. A. *Proteins: Struct, Funct, Bioinf* 55, 383-394 (2004).

38. Weiser, J., Shenkin, P. S., Still, W. C. 1999. *J Comput Chem* 20, 217-230.

39. Hornak, V., Abel, R., Okur, A., Strockbine, R., Roitberg, A., Simmerling, C. *Proteins: Struct, Funct, Bioinf* 65, 712-725 (2006).

40. Ryckaert, J., Cicotti, G., Berendsen, H. *J Comp Phys* 98, 10089-10092 (1977).

41. Tozzini, V. Coarse-grained models for proteins. *Curr Opin in Struct Biol* 15, 144-150 (2005).

42. Reith, D., Putz, M., Muller-Plathe, F. Deriving effective mesoscale potentials from atomistic simulations. *J Comput Chem* 24, 1624-1636 (2003).

43. Marrink, S.J., Rissalada, J. H., Yefimov, S., Tieleman, D. P., de Vries, A. H. The MARTINI force field: coarse-grained model for biomolecular simulations. *J Phys Chem B* 111, 7812-7824 (2007).

44. Trylska, J., Tozzini, V., McCammon, J. A. *Biophys J* 89, 1455-1463 (2005).

45. Mathworks 1994-2008).

46. Marrink, S.J., de Vries, A. H., Mark, A. E. *J Phys Chem B* 108, 750-760 (2004).

47. Abe, M., Kobayashi, Y., Yamamoto, S., Daimon, Y., Yamaguchi, A., Ikeda, Y., Ichinoki, H., Notaguchi, M., Goto, K., Araki, T. FD, a bZIP protein mediating signals from the floral pathway integrator FT at the shoot apex. *Science* 5737, 2876-2890 (2005).

48. Yasui, S.C., Keiderling, T. A. Vibrational circular dichroism of polypeptides. VI. Polytyrosine alpha-helical and random-coil results. *Biopolymers* 25, 5-15 (1986).

49. Duncan, R. The dawning era of polymer therapeutics. *Nat. Rev. Drug Discov.* 2, 347-360 (2003).

50. Satchi-Fainaro, R., Duncan, R. Polymer Therapeutics I: Polymers as drugs, conjugates, and gene delivery systems., Vol. 1. (Springer, New York; 2006).

51. Piccart, M.J., Bertelsen, K., James, K., Cassidy, J., Mangioni, C., Simonsen, E., Stuart, G., Kaye, S., Vergote, I., Blom, R., Grimshaw, R., Atkinson, R. J., Swenerton, K. D., Trope, C., Nardi, M., Kaern, J., Tumolo, S., Timmers, P., Roy, J. A., Lhoas, F., Lindvall, B., Bacon, M., Birt, A., Andersen, J. E., Zee, B., Paul, J., Baron, B., Pecorelli, S. Randomized intergroup trial of cisplatin-paclitaxel vs. cisplatin-cyclophosphamide in women with advanced epithelial ovarian cancer. *J. Natl. Cancer Inst.* 92, 699-708 (2000).

52. Wang, X., Gang, Z., Van, S., Yu, L., Vol. US20090226393. (ed. N.D.T. Corporation) 1-27 (Nitto Denko Technical Corporation, USA; 2009).

53. Ferrari, M. Cancer nanotechnology: opportunities and challenges. *Nat. Rev.* 5, 161-171 (2005).

54. Ferrari, M. Beyond drug delivery. *Nat. Nano.* 3, 131-132 (2008).

55. Decuzzi, P., Pasqualini, R., Arap, W., Ferrari, M. Intravascular delivery of particulate systems: does geometry really matter? *Pharma Res* 26, 235-243 (2009).

56. Nishiyama, N. Nanocarriers shape up for long life. *Nat. Nano.* 2, 203-204 (2007).

57. Geng, Y., Dalhaimer, P., Cai, S., Tsai, R., Tewari, M., Minko, T., Discher, D. E. Shape effects of filaments versus spherical particles in flow and drug delivery. *Nat. Nano.* 2, 249-255 (2007).

58. Srinivas, G., Shelley, J. C., Nielson, S. O., Discher, D. E., Klein, M. L. Simulation of diblock copolymer self-assembly, using a coarse-grain model. *J. Phys. Chem. B* 108, 8153-8160 (2004).

59. Jiang, W., Kim, B. Y., Rutka, J. T., Chan, W Nanoparticle-mediated cellular response is size-dependent. *Nat. Nano.* 3, 145-150 (2008).

60. Champion, J.A., Mitragotri, S Role of target geometry in phagocytosis. *Proc. Natl. Acad. Sci. USA.* 103, 4930-4934 (2006).

61. Champion, J.A., Katare, Y. K., Mitragotri, S. Particle shape: a new design for micro- and nanoscale drug delivery carriers. *J. Contr. Release* 121, 3-9 (2007).

62. Takeoka, S. Rolling properties of rGPIbα-conjugated phospholipid vesicles with different membrane flexibilities on vWf surface under flow conditions. *Biochem Biophys Res Commun* 296, 765-770 (2002).

63. Peng, L.X., Ivetac, A., Van, S., Zhao, G., Chaudhari, A. S., Yu, L., Howell, S. B., McCammon, J. A., and Gough, D. A. Characterization of a clinical polymer-drug conjugate using multiscale modeling. *Biopolymers* (2010).

64. Schames, J., Henchman, R. H., Siegel, J. S., Sotriffer, C. A., Ni, H., McCammon, J. A. Discovery of a novel binding trench in HIV integrase. *J. Med. Chem.* 47, 1879-1881 (2004).

65. Amaro, R.E., Schnaufer, A., Interthal, H., Hol, W., Stuart, W. D., McCammon J. A. Discovery of drug-like inhibitors of an essential RNA-editgin ligase in trypanosoma brucei. *Proc. Natl. Acad. Sci. USA.* 106, 17278-17283 (2008).

66. Monticelli, L., Kandasamy, S. K., Periole, X., Larson, R. G., Tieleman, D. P., Marrink, S. J. The MARTINI coarse-grained force field: extension to proteins. *J. Chem. Theory Comput.* 4, 819-834 (2008).

67. Marrink, S.J., de Vries, A. H., Mark, A. E. "Coarse-grained model for semi-quantitative lipid simulations." *J. Phys. Chem. B* 108, 750-760 (2004).

68. Marrink, S.J., Rissalada, J. H., Yefimov, S., Tieleman, D. P., de Vries, A. H. The MARTINI force field: coarse-grained model for biomolecular simulations. *J. Phys. Chem. B* 111, 7812-7824 (2007).

69. Amaro, R.E., Baron, R., and McCammon, J. A. An improved relaxed complex scheme for receptor flexibility in computer-aided drug design. *J. Comput. Aided. Mol. Des.* 22, 693-705 (2008).

70. Amaro, R.E., Chen, X., Ivanov, I., Xu, D., and McCammon, J. A. Characterizing loop dynamics and ligand recognition in human- and avian-type influenza neuraminidases via generalized born molecular dynamics and end-point free energy calculations. *J. Am. Chem. Soc.* 131, 4702-4709 (2009).

71. Cheng, L.S., Amaro, R. E., Xu, D., Li, W. W., Arzberger, P. W., and McCammon, J. A. Ensemble-based virtual screening reveals potential novel antiviral compounds for avian influenza neuraminidase. *J. Med. Chem.* 51, 3878-3894 (2008).

72. Humphrey, W., Dalke, A., and Schulten, K. VMD - Visual Molecular Dynamics. *J. Molec. Graph.* 14, 33-38 (1996).

73. Rowberg, R.E. in CRC Report for Congress (The Library of Congress Washington, D. C.; 2001).

74. Amiji, M.M. Nanotechnology for cancer therapy. (CRC Press, Boca Raton, FL; 2007).

75. Cho, K., Wang, X., Nie, S., Chen, Z., & Shin, D. M. Therapeutic nanoparticles for drug delivery in cancer. *Clin Cancer Res* 14, 1310-1316 (2008).

76. Adiseshaiah, P.P., Hall, J. B., & McNeil, S. E. Nanomaterial standards for efficacy and toxicity assessment. *WIREs Nanomed Nanobiotechnol* 2, 99-112 (2009).

77. Decuzzi, P., & Ferrari, M. The adhesive strength of non-spherical particles mediated by specific interactions. *Biomaterials* 27, 5307-5314 (2006).

78. Srinivas, G., Shelley, J. C., Nielson, S. O., Discher, D. E., Klein, M. L. Dissipative particle dynamics of polymersomes. *J Phys Chem B* 108, 8150-8160 (2004).

79. Ignatova, Z. Monitoring protein stability in vivo. *Microbial Cell Factories* 4, 23 (2005).

80. Lindahl, E., Hess, B., and van der Spoel, D. GROMACS 3.0: A package for molecular simulation and trajectory analysis. *J. Molec. Model.* 7, 306-317 (2001).

81. Amaro, R.E., Schnaufer, A., Interthal, H., Hol, W., Stuart, W. D., McCammon J. A. Discovery of drug-like inhibitors of an essential RNA-editing ligase in trypanosoma brucei. *Proc. Natl. Acad. Sci. USA.* 106, 17278-17283 (2008).

82. Amiji, M.M. Nanotechnology for cancer therapy. (CRC Press, Boca Raton, FL; 2007).

83. Satchi-Fainaro, R., Puder, M., Davies, J. W., Tran, H. T., Sampson, D. A., Greene, A. K., Corfas, G., Folkman, J. Targeting angiogenesis with a conjugate of HPMA copolymer and TNP-470. *Nat Med* 10, 225-261. (2004).

84. Kok, R.J., Schraa, A. J., Bos, E. J., Moorlag, H. E., Asgeirsdottir, S. A., Everts, M., Meijer, D. K. F., Molema, G. Preparation and functional evaluation of RGD-modified proteins as αVβ3 integrin directed therapeutics. *Bioconj Chem* 13, 128-135 (2002).

85. Chen, X., Plasencia, C., Hou, Y., Neamati, N. Synthesis and biological evaluation of dimeric RGD peptide-paclitaxel conjugate as a model for integrin-targeted drug delivery. *J Med Chem* 48, 1098-1106 (2005).

86. Lorger, M., Kreuger, J. S., O'Neal, M., Staflin, K., Felding-Habermann, B. Activation of tumor cell integrin αVβ3 controls angiogenesis and metastatic growth in the brain. *PNAS* 106, 10666-10671 (2009).

87. Temming, K., Schiffelers, R. M., Molema, G., Kok, R. J. RGD-based strategies for selective delivery of therapeutics and imaging agents to the tumour vasculature. *Drug Resis Updates* 8, 381-402 (2005).

88. Danhier, F., Vroman, B., Lecouturier, N., Crokart, N., Pourcelle, V., Friechels, H., Jérome, C., Marchand-Brynaert, J., Feron, O., Préat, V. Targeting of tumor endothelium by RGD-grafted PLGA-nanoparticles loaded with paclitaxel. *J Contr Rel* 2, 166-173 (2009).

89. Bourguet, E., Banères, J-L., Parello, J., Lusinchi, X., Girard, J-P., Vidal J-P. Nonpeptide RGD antagonists: a novel class of mimetics, the 5,8-disubstituted 1-azabicyclo[5.2.0]nonan-2-one Lactam. *Bioorg Medic Chem Lett* 13, 1561-1564 (2003).

90. McNeeley, K.M., Karathanasis, E., Annapragada, A. V., Bellamkonda, R. V. Masking and triggered unmasking of targeting ligands on nanocarriers to improve drug delivery to brain tumors. *Biomaterials* 30, 3986-3995 (2009).

91. Farokhzad, O.C., Langer, R. Impact of nanotechnology on drug delivery. *ACS Nano* 3, 16-20 (2009).

92. Marrink, S.J. "MARTINI tutorial 2A: Simulating proteins." (2010).

93. Cheng, L.S., Amaro, R. E., Xu, D., Li, W. W., Arzberger, P. W., and McCammon, J. A. Ensemble-based virtual screening reveals potential novel antiviral compounds for avian influenza neuraminidase. *J Med Chem* 51, 3878-3894 (2008).

94. Humphrey, W., Dalke, A., and Schulten, K. VMD - Visual Molecular Dynamics. *J Molec Graphics* 14, 33-38 (1996).